JOURNAL OF THE AERONAUTICAL SCIENCES

VOLUME 16 JANUARY, 1949 NUMBER 1

RECEIVED LIBRARY JAN 10 1949 The Dow Chemical Co.

CONTENTS

Linearized Treatment of Supersonic Flow Through Ducts ..... H. F. LUDLOFF AND F. REICHE 5

Two-Dimensional Airfoils in Hypersonic Flows ..... RICHARD D. LINNELL 22

Linearized Theory of Supersonic Control Surfaces ..... P. A. LAGERSTROM AND MARTHA E. GRAHAM 31

Efficient Applications of Stringer Panel and Multicell Wing Construction ..... GEORGE GERARD 35

The Boundary Layer of Yawed Infinite Wings ..... J. M. WILD 41

Problems and Progress in Low-Pressures Research ..... E. D. KANE AND R. G. FOLSOM 46

Airfoils in Slightly Supersonic Flow ..... HSUE-SHEN TSIEN AND JUDSON R. BARON 55

Readers' Forum: "Determination of Stability Derivatives from Flight Data," HARRY GREENBERG; "On Sweat-Cooling," E. A. RICHARDSON; and "Induction Effects in Aeroelasticity," JOHN W. MILES 62–64

LIBRARY COPY NOT FOR LOAN

Published by the

INSTITUTE OF THE AERONAUTICAL SCIENCES, INC.

629.13
J86
Vol. 16
1949

JOURNAL OF THE AERONAUTICAL SCIENCES

Editor: HUGH L. DRYDEN, *Director of Aeronautical Research, N.A.C.A.*

Associate Editor: ROBERT R. DEXTER *Associate Editor:* BERNEICE H. JARCK

The Institute of the Aeronautical Sciences publishes monthly the JOURNAL OF THE AERONAUTICAL SCIENCES and the AERONAUTICAL ENGINEERING REVIEW.

The JOURNAL OF THE AERONAUTICAL SCIENCES prints papers of scientific and technical interest to Institute members and subscribers. In general, it provides an opportunity for specialists to publish articles disclosing new knowledge and new applications in the field of the aeronautical sciences. The JOURNAL restricts itself to the aeronautical aspects of advances in science and engineering, and papers printed have either been submitted directly to the JOURNAL or have been previously presented at a meeting of the Institute.

The AERONAUTICAL ENGINEERING REVIEW keeps members and subscribers informed regarding the contents of new books and current periodicals in the field of aeronautics. It reviews new developments in the aircraft industry and reports on progress from house organs and catalogs published by aircraft and engine manufacturers and other companies engaged in aeronautical activities. It publishes papers on applied engineering and aircraft production. News of Institute activities is published in the REVIEW.

Statements and opinions expressed in the JOURNAL are to be understood as individual expressions of the authors and not those of the Institute.

SUBSCRIPTION RATES

Journal of the Aeronautical Sciences
Published Monthly

United States and Possessions		Foreign Countries Including Canada (American Currency Rate)	
1 Year	$12.00	1 Year	$13.00
Single Copies	1.50	Single Copies	1.50

Aeronautical Engineering Review
Published Monthly

United States and Possessions		Foreign Countries Including Canada (American Currency Rates)	
1 Year	$3.00	1 Year	$3.50
Single Copies	0.50	Single Copies	0.50

Notices of change of address should be sent to the Institute at least 30 days prior to actual change of address.

Manuscripts for publication, proofs, and all correspondence should be addressed to the Editorial Office of the JOURNAL.

Correspondence regarding subscriptions may be addressed to Publication Office, 20th and Northampton Sts., Easton, Pa., or to the Editorial Office of the JOURNAL OF THE AERONAUTICAL SCIENCES, 2 East 64th Street, New York 21, New York.

Copyright, 1949, by the Institute of the Aeronautical Sciences, Inc.

Entered as Second Class Matter at the Post Office, Easton, Pa., May 1, 1937. Acceptance for mailing at a special rate of Postage provided for in the Act of August 24, 1912. Authorized April 29, 1937.

270
663

JOURNAL OF THE AERONAUTICAL SCIENCES

VOLUME 16 JANUARY, 1949 NUMBER 1

Linearized Treatment of Supersonic Flow Through Ducts*†

H. F. LUDLOFF‡ AND F. REICHE**
New York University

ABSTRACT

The object of the investigation is to determine the velocity and pressure field occurring in supersonic flow through ducts of various shapes. In order to obtain results in analytical form, giving approximate insight into essential flow features, linearized treatment has been applied.

The solution has been composed by assuming that "supersonic sources" of various intensities are distributed over the surface of a skeleton cylinder. In Part (II) the expressions for velocity and stream function have been derived for three cases: (A) for constant source intensity; (B) for source intensity that increases linearly along the generatrices of the cylinder; (C) for a certain combination of the two previous cases, which turns out to be the most satisfactory approach to the problem insofar as generality and validity of the procedure is concerned. This last approach yields nozzle shapes for which location and size of the throat can be adjusted at will. Moreover, a general theorem has been derived enabling one to give expressions for the velocity field of any arbitrary source distribution (Appendix II).

Particular attention has been paid to the physical discussion of the results (Part III). The resulting pressure distribution inside the duct points to the occurrence of compression and expansion waves that appear at the surface of the Entrance Mach Cone and at the extension of this surface, called the "second Mach cone." In general, the intensity of these waves is small and the distance between them appreciable. The computations indicate, however, that, with certain properties of the duct rim, a compression wave would be immediately followed by an expansion wave, while the wave intensities increase.

The form of the wave front has been computed in a second approximation. For small lip angles, the wave shape is only slightly different from that of a double cone, in qualitative agreement with Ferri's analysis.

Received July 23, 1948. Based on a paper presented by H. F. Ludloff at the Aerodynamics Session, Fifteenth Annual Meeting, I.A.S., New York, January, 1947.

* This investigation was carried out under subcontract with A.P.L., Johns Hopkins University. Sponsored by the Navy Department. The authors wish to express their appreciation to Prof. F. K. Teichmann, Chairman of the Aeronautics Department New York University, for his kind interest and encouragement, and to Prof. K. O. Friedrichs, of the Institute for Mathematics and Mechanics, for numerous stimulating discussions.

† After completion of this paper, the authors noticed that M. J. Lighthill (R. and M. No. 2003) carried out an investigation along somewhat similar lines; however, approach and details are different.

‡ Associate Professor of Aeronautical Engineering, College of Engineering.

** Adjunct Professor of Physics, College of Engineering.

NOTATION

x, r	= axial and radial coordinate of test point P
ξ	= axial coordinate of source element
R	= radial distance from test point P to source element
d	= radius of skeleton cylinder
ω	= azimuth position about duct axis
α	= Mach angle; M = free-stream Mach Number; $\beta = \tan\alpha$
δ	= lip angle of duct
λ	= inclination of shock front
B	= distance between sources and sinks in case (C); see Fig. 3
Z	$= x/\beta d$; $Y = r/d$; $\zeta = \xi/\beta d$; $s = \dfrac{Z-(1-Y)}{2Y}$; $Z' = (x-B)/\beta d$
a	$= (1+Y)^2$; $b = (1-Y)^2$; $c = Z^2$
$f(\xi)$	= general source intensity per unit area $[L/T]$
A	= intensity of constant sources $[L/T]$
A'	= intensity of linear sources $[L/T]$
Φ	= disturbance velocity potential $[L^2/T]$
ψ	= disturbance stream function $[M/T]$
ρ	= disturbance density $[M/L^3]$
Φ_0, Ψ_0, and ρ_0	= free-stream potential, stream function, and density
U	= free-stream velocity
v_x and v_r	= axial and radial disturbance velocities
σ	$= A\beta\pi/U \sim \delta/\alpha$; $\sigma' = A'\beta\pi/U$
p	= absolute pressure
c_p	= pressure coefficient

(I) INTRODUCTION: OUTLINE OF THE INVESTIGATION

IN VARIOUS AERODYNAMICAL PROBLEMS, it is desirable to have an approximate, analytic method for computing the supersonic field of flow through ducted

31217

bodies in order to get quick insight into essential flow features as related to the shape of the nozzle wall. While the two-dimensional flow through nozzles has been commonly treated by the "method of characteristics," it has appeared that, for the three-dimensional case, the cumulative error (which must necessarily arise in this step-by-step method) makes it worth while to try a different approach. The advantage of the present method is that it would yield the streamlines all at once and at the same time permit some insight to be gained of the analytical features of the solution.

We are considering a supersonic air stream entering a nozzle whose constriction occurs slowly enough so that the prerequisites of the linearized theory can be considered as fulfilled. The flow may be anticipated to remain supersonic throughout, in spite of the occurrence of one or two oblique shocks. The approach to the problem is analogous to that in the problem of supersonic flow about slender bodies of revolution, treated by von Kármán and Moore.[1] In the case at hand "supersonic sources" of various intensities are placed on the surface of a skeleton cylinder, and the velocities, pressures, and streamlines resulting from such a "source" system are determined. According to the usual procedure, an appropriate system of streamlines may be considered to form the wall contour of the nozzle. Therefore, the present objective is to determine the wall contour and the velocity and pressure field corresponding to a given "source" distribution. The inverse problem will be treated in a second paper.

The influence of the nozzle wall on the velocity field can be best understood by dividing the whole flow field into four districts (see Fig. 6). Starting at the duct entrance, there is first a conical region (1), in which the air stream continues to flow undisturbed. Behind the Mach cone, originating at the entrance rim, the disturbances arising from the duct wall are felt. But they are not felt all at once. In the two intermediate districts, (2) and (3), the influence of the upper or the lower part of the wall section will predominate. From Fig. 6, one can see that a point in districts (2) or (3) is not influenced by source elements of the directly opposite part of the nozzle wall. Disturbances, produced by the entrance rim, are propagated along Mach lines whose extensions form a *second* Mach cone. Behind this second Mach cone begins the rear district (4), in which any point of the flow field is under the combined influence of source elements located at *any* value of the azimuth ω, on the surface of the cylinder.

The analytical investigation is divided into three parts. In Part (A) the source intensity is assumed to be constant all over the surface of the skeleton cylinder. As a second case, in Part (B) the source intensity is assumed to increase linearly along the generatrices of the cylinder. Finally, Part (C) contains the analysis of a source distribution, which is a certain combination of the two previous cases and, apparently, the most satisfactory approach to the problem, insofar as flexibility, generality, and validity of the procedure is concerned.

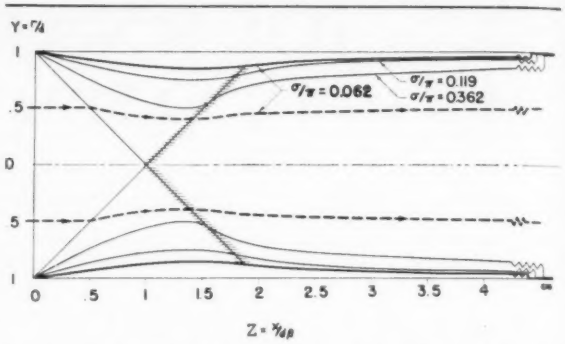

FIG. 1. Wall contours and streamlines of nozzle produced by constant source distribution.

In the case of constant source intensity, it turns out that the streamlines and wall contour of the nozzle form a throat at some distance behind the entrance rim, and the inside diameter increases at the exit section to the same magnitude that it had at the entrance section. Since velocity, density, and pressure are also the same at the rear end as at the entrance, the wave drag originating from the inside of the duct will be zero.

Some quantitative results of the analysis are shown in Fig. 1. The velocities and streamlines of the flow produced by sources of constant strength have been computed and three particular streamlines that start at the rim and represent possible wall contours have been plotted. The wall contours correspond to three different source strengths as indicated in the figure, and, of course, the stronger the source intensity, the larger the deflection of the wall contour from the skeleton cylinder and the more pronounced the throat. The streamlines entering halfway between axis and duct wall are also shown.

The analysis permits one to draw certain conclusions regarding the occurrence of shocks. At the entrance cone a discontinuity of velocity appears which is small except at the vertex of the cone. [See Eqs. (11) and (39).] In other words, the Mach cone at the entrance of the duct represents a conical compression shock that is weak except in the intermediate vicinity of the vertex. It is possible to compute the form of the shock front in second approximation by use of the shock polar equations. The result obtained in this way can be compared with Ferri's computation of the entrance shock carried out by means of the method of characteristics and is shown to be in satisfactory agreement. [See Section III, (3).]

Furthermore, it is found that, on the surface of the second Mach cone, a compression and subsequent expansion wave originate, one immediately behind the other. This result is discussed in Section III, 2, and it is pointed out that a similar phenomenon may occur in the problem of von Kármán and Moore. Some features of this result are outside the range of validity

of the linearized theory—which is to be expected, since at the entrance rim of the cylinder the source intensity increases discontinuously from zero to a finite value. But it can be shown that this pattern constitutes the limiting case of a more general flow pattern which is perfectly *within* the range of this theory. Therefore our results in the vicinity of the second Mach cone are qualitatively correct, although they may not be interpreted quantitatively.

In accordance with the theory of characteristics, the singularity occurring on the second Mach cone is due to properties of the duct rim. Therefore, the features of an air stream entering a duct with a knife-sharp rim have been analyzed. (See Section II, B.) Flow conditions of this character can be materialized if the surface of the skeleton cylinder is covered by a source distribution whose intensity is linearly increasing, starting at the rim. And indeed, the analytical treatment shows that this velocity pattern does not produce any peculiarity at the second Mach cone. There are also no discontinuities of velocity at the entrance cone in this case, so that the whole flow field can be considered to be within the range of validity of the linearized theory. Disregarding boundary-layer effects, the sharp entrance rim of a duct would seem to be a means of avoiding shocks, while a blunt rim will produce them.

Computation of the streamlines that represent the contour of the nozzle wall (see Fig. 2) shows that in this case no throat is produced, but the cross section of the duct narrows down the more one recedes toward the rear. Since the cross section decreases in a logarithmic way, the flow becomes, for practical purposes, parallel after a certain distance from the entrance is reached. However, the ratio of exit to entrance section will be definitely smaller than one, so that a considerable wave drag would result.

It is possible to combine the merits of the last two nozzle shapes without encountering their respective setbacks. Fig. 3 shows the result of this combination which consists of a source intensity that starts to increase linearly at the rim and remains constant after a certain distance B from the entrance is reached. Careful analytical investigation (see Section II, C) shows that the knife-edged rim hinders the formation of a discontinuity of velocity at the entrance or a singularity at the second Mach cone. On the other hand, the constant part of the source layer takes care that the inside diameter, after narrowing down to a throat, increases at the exit section to its original magnitude so that the wave drag is zero. The source distribution that produces this nozzle shape can be resolved into two linearly increasing layers, one consisting of sources and starting at the entrance rim of the duct and the other consisting of sinks and starting a distance B behind—i.e., where, in the previous representation, the constant layer begins (see Fig. 3). As linearly increasing source intensities have been shown to produce flow fields that are everywhere regular, the super position

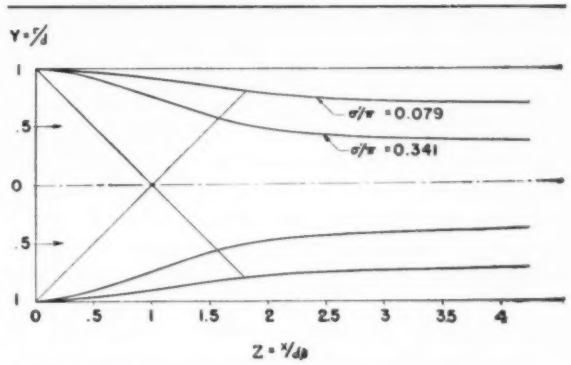

FIG. 2. Wall contours of ducts produced by linearly increasing source distribution.

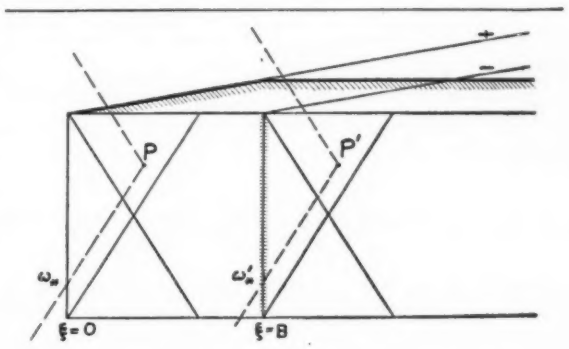

FIG. 3. Analysis of source sink combination; Case C.

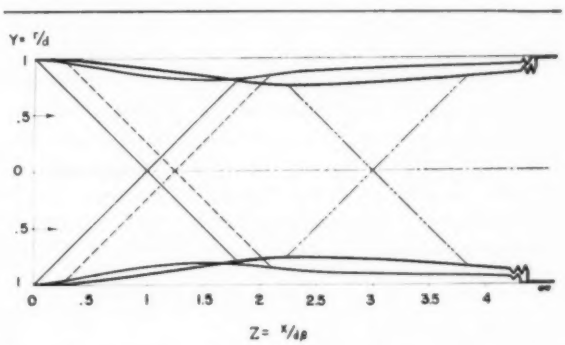

FIG. 4. Wall contours of nozzles produced by two different source sink combinations.

of two such distributions will certainly not produce any singularity in the flow field. By varying the source and sink intensities and by changing the distance B between sources and sinks, the location and size of the throat can be adjusted at will. (See, e.g., the two wall contours of Fig. 4.) Thus, the use of this source distribution (C) represents a flexible procedure that provides results that are valid at all points inside the duct. The first two cases (A) and (B), may be considered as instructive auxiliary considerations.

(II) Analytical Investigation of the Flow Field

(1) General Form of the Velocity Potential

The analytical investigation is based on the computation of the velocity potential, from which the velocity components, the stream function, the pressure, and the wave drag can be derived. Consider "sources" of given intensity per unit area distributed over a circular cylinder upon which a supersonic air stream is impinging. The resulting flow pattern will consist of the undisturbed air stream plus the perturbation flow produced by these supersonic "sources." Of course, since one is dealing with a linearized theory, the perturbation velocities are assumed to be small in comparison with the main flow velocity; this is the case if the cross section of the duct changes slowly. The perturbation flow can be completely described when the velocity potential due to this source distribution is known.

As can be seen from Fig. 5, the potential, $d\Phi$ at point P, contributed by the elemental source area at $x = \xi$, is given by:

$$d\Phi = -d\,\frac{f(\xi)\,d\xi\,d\omega}{\sqrt{(x-\xi)^2 - \beta^2 R^2}} \qquad (1)$$

here $f(\xi)$ is the source strength per unit area at $x = \xi$; the source distribution is axial symmetrical, so that f does not depend on ω. $\beta^2 = M^2 - 1$, M being the main stream Mach Number. R is the distance from the point P to a surface point in the same plane, as explained in Figs. 5 and 7. The denominator in Eq. (1) is a "pseudo distance," which reduces to the real distance between P and the surface element when $M = 0$.

To obtain the total potential at P, an appropriate integration over the surface of the cylinder must be made. It is apparent that only sources contained between the entrance rim and the fore cone of P will affect the potential at P (see Fig. 5). Therefore, the integration over ξ extends from 0 to $x - \beta R$, where x is the abscissa of P.

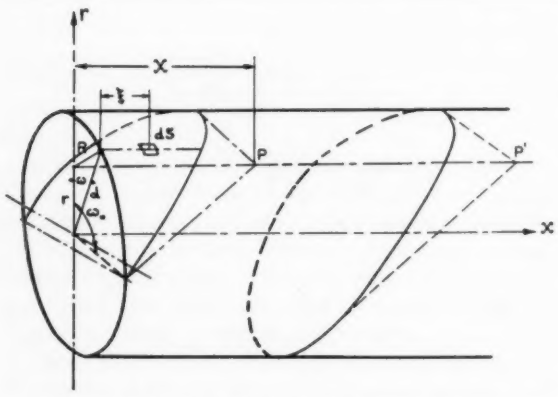

Fig. 5. Geometry of skeleton cylinder and fore cones.

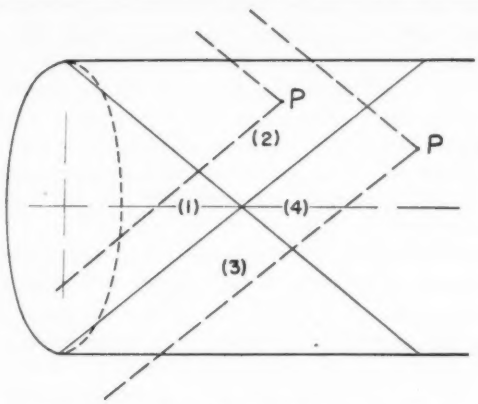

Fig. 6. The four districts of the flow field: (1) zone of silence; (2) and (3) front district; (4) rear district.

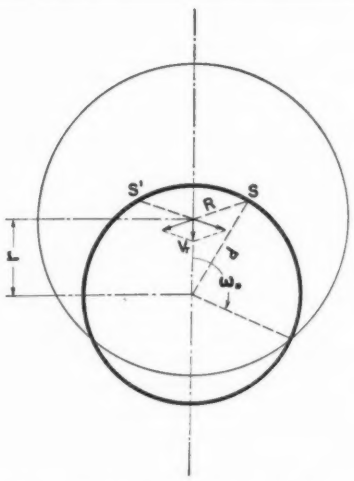

Fig. 7. View of entrance plane of duct, showing intersection of skeleton cylinder and Mach cone of P.

To determine the limits of ω, two cases may arise (see Fig. 6).

When point P is in region (4), called the "rear district," it is obvious that ω runs from $-\pi$ to $+\pi$. However, when P is in regions (2) or (3), called "front district," the fore cone of P intersects only a portion of the cylindrical surface so that ω has the limits $-\omega_*$ and $+\omega_*$. (See also Fig. 7.)

With the understanding that $\omega_* = \pi$ when P is in the rear district, the expression for the total potential at P becomes:

$$\Phi = -2d \int_0^{\omega_*} d\omega \int_0^{x-\beta R} d\xi\,\frac{f(\xi)}{\sqrt{(x-\xi)^2 - \beta^2 R^2}} \qquad (2)$$

From Fig. 7 it can be seen that

$$R^2 = d^2 + r^2 - 2dr\cos\omega \qquad (3)$$

and from Fig. 6 it follows that for $\omega = \omega_*$ the ξ-integration interval reduces to the point $\xi = 0$. Hence,

$$0 = \xi = x - \beta R(\omega_*), \qquad R(\omega_*) = x/\beta \tag{3a}$$

Thus, using Eq. (3),

$$\omega_* = \cos^{-1}\left[d^2 + r^2 - (x^2/\beta^2)\right]/2dr \tag{4}$$

By differentiating Eq. (2) with regard to x and r, one can show that the linearized equation determining an axial symmetrical potential Φ is fulfilled. While the direct verification is lengthy and cumbersome, the proof given in Appendix I is more elucidating.

We have now to carry out the integration in Eq. (2); therefore the treatment will be divided, according to the type of source distribution considered.

(2) *Case A. Constant Source Distribution on Circular Cylinder*

Substituting in Eq. (2) $f(\xi) = A$ and carrying out the ξ-integration, one gets:

$$\Phi = -2Ad \int_0^{\omega_*} d\omega \log \frac{\beta R/x}{1 - \sqrt{1 - (\beta R/x)^2}} \tag{5}$$

Differentiating with respect to r, one gets the radial velocity component:

$$v_r = 2Ad \int_0^{\omega_*} d\omega \frac{r - d\cos\omega}{R^2} \frac{1}{\sqrt{1 - (\beta R/x)^2}} \tag{6}$$

It is appropriate now to introduce the dimensionless variables: $Z = x/\beta d$ and $Y = r/d$.

Upon introduction of a new integration variable,

$$\rho = R^2/d^2 = 1 + Y^2 - 2Y\cos\omega$$

Eq. (6) becomes:

$$v_r = AZY^{-1} \int_b^c \frac{d\rho}{\rho} \frac{\rho - \sqrt{ab}}{\sqrt{(c-\rho)(a-\rho)(\rho-b)}} \tag{7a}$$

for $b \leq c \leq a$: front district;

$$v_r = AZY^{-1} \int_b^a \frac{d\rho}{\rho} \frac{\rho - \sqrt{ab}}{\sqrt{(c-\rho)(a-\rho)(\rho-b)}} \tag{7b}$$

for $b \leq a \leq c$: rear district.

Here, $a = (1+Y)^2$, $b = (1-Y)^2$, and $c = Z^2$.

If point P moves on the second Mach cone, c becomes equal to a. At the integration limits, the *integrand* in Eq. (7a) or (7b) becomes infinite as $1/\sqrt{\rho - b}$ (or $1/\sqrt{c-\rho}$ and $1/\sqrt{a-\rho}$, respectively); this square root singularity of the integrand disappears in the integrated expression for v_r. However, if $c \to a$, the two square root singularities of the integrand coalesce to form an $1/(a-\rho)$ singularity. Then, the integrated expression for v_r becomes logarithmically infinite.

(*a*) *Front District.*—In order to obtain a constant integration interval that is independent of Z and Y, one may introduce:

$$\rho = b + (c-b)\eta$$

so that $0 \leq \eta \leq 1$, when $b \leq \rho \leq c$. Putting

$$k^2 = \frac{c-b}{a-b} = \frac{Z^2 - (1-Y)^2}{4Y}$$

which is smaller than 1 in the front district, Eq. (7a) becomes:

$$v_r = -AZY^{-1/2} \int_0^1 d\eta \times \frac{[(1-Y) - 2k^2\eta]}{[(1-Y)^2 + 4Yk^2\eta]\sqrt{\eta(1-\eta)(1-k^2\eta)}} \tag{8}$$

It can be shown that Eq. (8) can be expressed as a combination of elliptic integrals. The transformations required for that purpose will be explained in a paper by Mack and the authors.[2] Here, however, the solution will be carried out on the basis of an expansion of $1 \div \sqrt{1 - k^2\eta}$, giving:

$$v_r = -AZY^{-1/2} \int_0^1 d\eta \left\{\frac{(1-Y) - 2k^2\eta}{(1-Y)^2 + 4Yk^2\eta}\right\} \times \left[\frac{1 + (1/2)\eta k^2 + (3/8)\eta^2 k^4 + \ldots}{\sqrt{\eta(1-\eta)}}\right] \tag{9}$$

Combining equal powers of η under the same integrals, one gets:

$$v_r = -AZY^{-1/2}\left[(1-Y)I_0 - (1/2)(3+Y)k^2 I_1 - (1/8)(5+3Y)k^4 I_2 - (1/16)(7+5Y)k^6 I_3 - (5/128) \times (9+7Y)k^8 I_4 - \ldots\right] \tag{10}$$

where

$$I_n = \int_0^1 d\eta \frac{\eta^{n-(1/2)}}{(1-\eta)^{1/2}\left[(1-Y)^2 + 4k^2 Y\eta\right]} \tag{10a}$$

which can be evaluated by means of a recursive formula and yield simple rational functions of Y, Z, and k^2.

Upon substituting I_n and k^{2n}, Eq. (10) becomes:

$$v_r = -U\sigma\beta^{-1}Y^{-1/2}\left\{1 - s\left(\frac{3+Y}{4}\right) - (1/2)\,s^2\left(\frac{5+3Y}{8}\right)\left[\frac{Z + 2(1-Y)}{4}\right] - (9/32)s^3\left(\frac{7+5Y}{12}\right) \times \left[\frac{Z^2 + 3Z(1-Y) + (8/3)(1-Y)^2}{8}\right]\ldots\right\} \tag{11}$$

Here two more characteristic dimensionless parameters have been introduced—namely, $\sigma = A\beta\pi/U$ and $s = [Z - (1-Y)]/2Y$; the lines, s = constant, represent the set of rays going through the tip of the Mach cones. The meaning of σ is explained later.

Stokes' three-dimensional representation of the stream function ψ, which can be derived by considering the flux through a cylindrical surface,[3] may be written as either

$$\psi_{x=x} = -\rho_0 \int_{\beta(d-r)}^{x} r v_r \, dx' = -\rho_0 U d^2 \int_{1-Y}^{Z} dZ' \times (\beta U^{-1}) Y v_r(Z', Y) \quad (12a)$$

or

$$\psi_{r=r} = -\rho_0 \beta^2 \int_0^r r' v_x \, dr' = -\rho_0 U d^2 \times \int_0^Y dY' (\beta^2 U^{-1}) Y' v_x(Y,' Z) \quad (12b)$$

By substituting Eq. (11) into Eq. (12a) and carrying out the integration, one gets:

$$\psi = \Psi_0 4\sigma Y^{3/2} s \left\{1 - \left(\frac{1}{2}\right) s \frac{3+Y}{4} - \left(\frac{1}{8}\right) s^2 \times \frac{5+3Y}{8}(1-Y) - \left(\frac{1}{16}\right) s^3 \left[Y \frac{5+3Y}{8} + \frac{15}{16}(1-Y)^2 \frac{7+5Y}{12} \right] - \ldots \right\} \quad (13)$$

here, $\Psi_0 = (1/2)\rho_0 U d^2$ is the flux crossing the entrance section of the nozzle.

The radius of convergence of the series (13) is $s = 1$, since v_r, from which Eq. (13) has been obtained by integration, becomes logarithmically infinite for this value. It can be shown that up to $s = 0.8$ four terms of Eq. (13) provide, for practical purposes, sufficiently accurate results, as may be seen from comparison of Eq. (13) with the exact solution in terms of elliptic integrals (see references 2 and 4), which yields:

$$\psi = \Psi_0 2\pi^{-1}\sigma \{4\sqrt{Y}\,[k'^2 K(k) - E(k)] + Z[\pi + 2(K(k) - E(k))F(k', \theta) - 2K(k)E(k', \theta)]\} \quad (14)$$

here: $k'^2 = 1 - k^2$; $\theta = \sin^{-1}[(1-Y)/Z]$ $(0 < \theta < \pi/2)$.

Before passing over to the determination of the stream function in the "rear district," it is of interest to examine the stream function on the dividing line $s = 1$—i.e., on the second Mach cone. This enables one to obtain a value for ψ at a point where both the front and rear representations fail. As explained later on, the exact value of the stream function on the second Mach cone assumes the form:

$$\psi_{s=1} = 8\Psi_0 \sigma \pi^{-1}[(1+Y) \arctan(\sqrt{Y}) - \sqrt{Y}] \quad (15)$$

The closed form expression (15) for ψ becomes possible, because, for $s = 1$, the previously mentioned elliptic integrals *degenerate*. Numerical evaluation of Eq. (13) for $s = 3/4$ and Eq. (15) for $s = 1$ has shown that the respective values are compatible.

(*b*) *Rear District.*—Analogously, as in the front district, one may now introduce

$$\rho = b + (a - b)\eta$$

and

$$k_1^2 = \frac{1}{k^2} = \frac{a-b}{c-b} = \frac{4Y}{Z^2 + (1-Y)^2}$$

which is smaller than 1 in the rear district. Then Eq. (7b) yields:

$$v_r = -A2Z[Z^2 - (1-Y)^2]^{-1/2} \int_0^1 d\eta \times \frac{[(1-Y) - 2\eta][1 + (1/2)\eta k_1^2 + (3/8)\eta^2 k_1^4 + \ldots]}{\sqrt{\eta(1-\eta)}[(1-Y)^2 + 4Y\eta]} \quad (16)$$

which can be evaluated similarly as Eq. (9) and is shown to vanish asymptotically for large Z as Z^{-2}.

To obtain the stream function, one may use Eq. (12a) in a form more suitable for evaluation in the rear district. Since

$$\psi_{x=\infty} = -\rho_0 \int_{\beta(d-r)}^{x} r v_r \, dx' - \rho_0 \int_x^{\infty} r v_r \, dx' = 0$$

one has

$$\psi(x, r) = -\rho_0 \int_{\infty}^{x} r v_r \, dx' \quad (17)$$

Substituting Eq. (16) into Eq. (17), one obtains:

$$\psi = \Psi_0 \sigma Y^{3/2} k_1 \left\{1 + (1/3)k_1^2 \left[\frac{12 + 9Y - 3Y^2}{16(1+Y)}\right] + (1/5)k_1^4 \left[\frac{75 + 45Y - 25Y^2 + 5Y^3}{128(1+Y)}\right] + \ldots \right\} \quad (18)$$

In terms of elliptic integrals (see references 2 and 4), one obtains:

$$\psi = \Psi_0 2\pi^{-1}\sigma \left\{ \frac{4\sqrt{Y}}{k_1} \left[\frac{1-Y}{1+Y} k_1'^2 K(k_1) - E(k_1)\right] + Z[\pi + 2(K(k_1) - E(k_1))F(k_1', \theta) - 2K(k_1)E(k_1', \theta)] \right\} \quad (19)$$

here: $\theta = \sin^{-1}[(1-Y)/(1+Y)]$; $k_1'^2 = 1 - k_1^2$.

(*c*) *Rear District: Expansion After* ρ/Z^2.—A more convenient representation of the stream function in the rear district is obtained by starting from expression (6) for v_r:

$$v_r = A Y^{-1} \int_0^{\pi} d\omega \frac{\rho - (1 - Y^2)}{\rho} \left(\frac{1}{\sqrt{1 - \rho/Z^2}}\right)$$

expanding $1/\sqrt{1 - \rho/Z^2}$, in powers of ρ/Z^2, one obtains:

$$v_r = A Y^{-1} \int_0^{\pi} d\omega \left[1 - \frac{1 - Y^2}{\rho}\right] \times \left[1 + \left(\frac{1}{2}\right)(\rho/Z^2) + \left(\frac{3}{8}\right)(\rho/Z^2)^2 + \ldots\right] \quad (20)$$

Evaluation of the integrals $\int_0^{\pi} d\omega \, \rho^n(\omega, Y)$ yields simple polynomials of $2n$th degree in Y.

To obtain the stream function, one may use again Eq. (12a), which yields:

$$\psi = \Psi_0 2\sigma Y^2 Z^{-1}[1 + (1/4)Z^{-2}(2 + Y^2) + (1/8)Z^{-4}(3 + 6Y^2 + Y^4) + (5/64)Z^{-6} \times (4 + 18Y^2 + 12Y^4 + Y^6) + \ldots] \quad (21)$$

this becomes identical with Eq. (18) for large Z.

The stream function of our flow pattern is obtained by adding the undisturbed and perturbation stream functions at any point (Z, Y):

$$\Psi = \Psi_0 Y^2 + \psi(Z, Y) = \Psi_0 (d_i/d)^2 \quad (22)$$

The left-hand side of this equation represents the total stream function; the right-hand side represents the constant value that the stream function assumes on the particular streamline which, in front of the duct, is at a distance d_i from the axis. To plot the streamlines, Eq. (22) has to be solved for Y in terms of Z. The streamline representing the wall contour is obtained by putting in Eq. (22) $d_i = d$. This yields:

$$Y^2 = 1 - (1/\Psi_0)\psi(Z, Y) \quad (22a)$$

It may be noted that the lip angle δ, which this wall contour forms with the skeleton cylinder, is given by:

$$\delta \sim \tan \delta = (v_r/U)_{\substack{Z=0 \\ Y=1}} = \pi A/U \quad (23)$$

The dimensionless quantity $\sigma = \pi A\beta/U$, introduced earlier turns out to be

$$\sigma = \frac{\pi A}{U}\frac{1}{\tan \alpha} = \frac{\tan \delta}{\tan \alpha} \sim \frac{\delta}{\alpha} \quad (24)$$

and measures the lip angle in terms of the Mach angle.

(3) *Case B: Source Distribution of Linearly Increasing Strength*

In the following:

$$f(\xi) = A'\xi/\beta d = A'\zeta$$

here: $\zeta = \xi/\beta d$.

A' is a constant which characterizes the rate of source intensity increase. Substituting in Eq. (2), one gets, for the velocity potential:

$$\Phi = -2d\int_0^{\omega_*} d\omega \int_0^{x-\beta R} d\xi \frac{A'(\xi/\beta d)}{\sqrt{(x-\xi)^2 - \beta^2 R^2}} \quad (25)$$

Introducing the dimensionless variables, as before, and in addition,

$$\sigma' = A'\beta\pi/u; \qquad Ud = \Phi_0$$

one can write:

$$\Phi = -\Phi_0 \pi^{-1} 2\sigma' \beta^{-1} \int_0^{\omega_*} d\omega \int_0^{Z-\sqrt{\rho}} d\zeta \frac{A'\zeta}{\sqrt{(Z-\zeta)^2 - \rho}}$$

which, on carrying out the $\zeta =$ integration, yields:

$$\Phi = -\Phi_0 \pi^{-1} \beta^{-1} 2\sigma' \int_0^{\omega_*} d\omega \times \left[Z \log \frac{Z + \sqrt{Z^2 - \rho}}{\sqrt{\rho}} - \sqrt{Z^2 - \rho}\right] \quad (26)$$

Differentiating with regard to r, one now obtains:

$$v_r = U\pi^{-1}\beta^{-1}2\sigma' \left\{\int_0^{\omega_*} d\omega \left[\sqrt{Z^2/\rho - 1}\right]\frac{d\sqrt{\rho}}{dY} + \left[-Z \cosh^{-1}\frac{Z}{\sqrt{\rho}} + \sqrt{Z^2 - \rho}\right]\frac{d\omega_*}{dY}\right\} \quad (27)$$

As shown previously, $\rho(\omega_*) = Z^2$, so that the last of the terms in Eq. (27) vanishes.

Again using ρ instead of ω as integration variable, Eq. (27) transforms into:

$$v_r = U\pi^{-1}\beta^{-1}\sigma' Y^{-1} \int_b^c \frac{d\rho}{\rho} \frac{\sqrt{c-\rho}(\rho - \sqrt{ab})}{\sqrt{(a-\rho)(\rho - b)}} \quad (28a)$$

for $b \leq c \leq a$: front district;

$$v_r = U\pi^{-1}\beta^{-1}\sigma' Y^{-1} \int_b^a \frac{d\rho}{\rho} \frac{\sqrt{c-\rho}(\rho - \sqrt{ab})}{\sqrt{(a-\rho)(\rho - b)}} \quad (28b)$$

for $b \leq a \leq c$: rear district.

In marked difference to the case of constant source distribution, Eqs. (28a) and (28b) contain the factor $\sqrt{c-\rho}$ in the *numerator* instead of the denominator, so that in the limit $c \to a$ the factors $\sqrt{c-\rho}$ and $\sqrt{a-\rho}$ cancel rather than form a cumulative singularity.

(*a*) *Front District.*—Proceeding similarly as in the case of constant sources, one obtains without difficulty series expansions for all the quantities under study. However, by means of the Recurrence Theorem, formulated in Appendix II, the derivations may be considerably shortened. It is proved in Appendix II that

$$v_r^{\text{lin}} = -(\rho_0 d^2 \beta Y)^{-1}\left(\frac{\sigma'}{\sigma}\right)\psi_{const.} \quad (A19)$$

$$v_x^{\text{lin}} = \frac{\partial \Phi_{\text{lin}}}{\partial x} = (d\beta)^{-1}\left(\frac{\sigma'}{\sigma}\right)\Phi_{const.} \quad (A20)$$

$$\psi_{\text{lin}} = \frac{\sigma'}{\sigma}\int_{1-Y}^{Z} dZ' \psi_{const.} \quad (A21)$$

Hence, using Eqs. (A19) and (13), one obtains immediately:

$$v_r^{\text{lin}} = -2\beta^{-1}U\sigma' Y^{1/3} s\left\{1 - \left(\frac{1}{2}\right)s\frac{3+Y}{4} - \left(\frac{1}{8}\right)s^2\frac{5+3Y}{8}(1-Y) - \left(\frac{1}{16}\right)s^3 \times \left[Y\frac{5+3Y}{8} + \left(\frac{5}{16}\right)(1-Y)^2\frac{7+5Y}{12}\right] - \ldots\right\} \quad (29)$$

Since Eq. (29) is convergent for $s < 1$, one may integrate termwise, so that according to Eq. (12a):

$$\psi_{\text{lin}} = \Psi_0 4\sigma' Y^{5/2} s^2 \left\{ 1 - \left(\frac{1}{3}\right) s \frac{3+Y}{4} - \left(\frac{1}{16}\right) s^2 \times \frac{5+3Y}{8}(1-Y) - s^3 \left[\left(\frac{1}{40}\right) \frac{5+3Y}{8} Y + \left(\frac{3}{128}\right) \frac{7+5Y}{12} (1-Y)^2 \right] - \ldots \right\} \quad (30)$$

(*b*) *Solution on the Second Mach Cone.*—From the general expressions [Eqs. (28a) and (28b)], one can see that on the second Mach cone ($a = c$) the integral simplifies to:

$$(v_r)_{k^2=1} = U\pi^{-1}\beta^{-1}\sigma' Y^{-1} \int_b^a \frac{d\rho}{\rho} \frac{\rho - \sqrt{ab}}{\sqrt{\rho - b}}$$

which can be evaluated in closed form—namely,

$$(v_r)_{k^2=1} = -U4\pi^{-1}\beta^{-1}\sigma' \left(\frac{1+Y}{Y} \arctan \sqrt{Y} - \frac{1}{\sqrt{Y}} \right) \quad (31)$$

It is not possible to derive a closed expression for ψ_{lin} at the second Mach cone; in order to make use of Eq. (12a), one needs v_r as function of x, which is not available. However, a simple expression for $\psi_{const.}$ at the second Mach cone can be derived from the above by direct use of Eq. (A19). This expression has already been quoted in Eq. (15).

(*c*) *Rear District.*—To compute the stream function in this case one may apply the recurrence theorem (A21) and obtain:

$$\psi_{\text{lin}} = \Psi_0 2\sigma' Y^2 \left\{ \log 2Z - \left(\frac{1}{8}\right) \left[\frac{1}{Z^2}(2 + Y^2) + \left(\frac{1}{4}\right) \frac{1}{Z^4}(3 + 6Y^2 + Y^4) + \left(\frac{5}{48}\right) \frac{1}{Z^6} \times (4 + 18Y^2 + 12Y^4 + Y^6) + \ldots \right] \right\} \quad (32)$$

As in the case of constant sources, so here the streamlines can also be evaluated by using the relation (22a):

$$Y^2 = 1 - (1/\Psi_0)\psi_{\text{lin}}(Z, Y)$$

By substituting the stream functions (13), (21), (30), and (32) into (22a), it becomes possible to compute shape and location of streamlines and wall contours. The results of such computations are shown in Figs. 1 and 2.

(4) *Case C: Sources Distributed with Combined Linearly Increasing and Constant Strength*

In order to adapt the method to the representation of flow through more general nozzle shapes, an instructive combination of the source distributions treated in Parts (A) and (B) shall be considered in this section. This type of source combination is capable of generalization; at the same time it permits one to retain those particular features of constant or of linear source distributions which are desirable while on the other hand eliminating the undesirable ones.

In Fig. 3 the shaded heavy line represents the considered distribution of source strength along a generatrix of the cylinder: the source strength is linearly increasing between $\xi = 0$ and $\xi = B$ (B being some arbitrary, fixed distance behind the rim), and then it remains at constant strength from $\xi = B$ to $\xi \to \infty$. There is again the same source strength for all azimuth positions for any particular value of ξ.

In order to form the velocity potential of this source combination, it is, of course, possible to compose it, as indicated—namely, by inserting into Eq. (2), first, $f(\xi) = A'(\xi/\beta d)$ and extending the ξ-integration from $\xi = 0$ to $\xi = B$; second, $f(\xi) = A'(B/\beta d)$ and extending the ξ-integration from $\xi = B$ to $\xi = x - \beta R$; finally, by adding the two expressions. It can be shown that this procedure of composing the potential yields in either component potential a singularity; however, in the combined potential the singularities cancel each other; this indicates that, for this source combination (also when the point under consideration moves on the second Mach cone) the velocity field will remain regular.

These features become evident in a more convenient way if the prescribed source combination is formed in another manner, which is also indicated in Fig. 3 by (a) having sources of strength $A'(\xi/\beta d)$ start at $\xi = 0$ and extend indefinitely to the right and (b) having sinks of the same strength start at $\xi = B$ and extend indefinitely to the right. Then the net source strength for $\xi \geq B$ is given by:

$$f(\xi) = A'(\xi/\beta d) - A'(\xi - B)/\beta d = A'B/\beta d$$

as it should be.

In this way one obtains the velocity potential by algebraic addition of two analogous expressions for linear sources and linear sinks, with the following provisos: replace in Eq. (25) A' of the sources with $(-A')$ for the sinks; also replace x of the test point and ξ of the source element, corresponding to the sources, with x' and ξ' for the sinks, where

$$x' = x - B; \qquad \xi' = \xi - B \quad (33)$$

This stipulation expresses the fact that we are, in effect, dealing with *two* cylinders: one on which the linear sources are located, and another one that is covered with linear sinks, the two cylinders being coaxial and identical except that their entrance rims are shifted with regard to each other by a distance B. With this interpretation in mind (see Fig. 3), one can visualize that the source distribution begins at $\xi = 0$, ω extending from $-\omega_*$ to $+\omega_*$, and that the sink distribution starts at $\xi' = 0$—i.e., $\xi = B$, ω extending from $-\omega_*'$ to $+\omega_*'$. Here ω_*, defined by Eq. (4), is the azimuth of the point at which the Mach circle and the rim of the *source* cylinder intersects; ω_*', corresponding to the point of intersection between Mach circle and rim of *sink* cylinder, is obtained by replacing

in Eq. (4) x by x'. Therefore, the following velocity potential of this source sink combination results:

$$\Phi = \Phi_+ + \Phi_-$$

$$= -2d\int_0^{\omega_*} d\omega \int_0^{s-\beta R} d\xi \frac{A'(\xi/\beta d)}{\sqrt{(x-\xi)^2-\beta^2R^2}} + 2d\int_0^{\omega_*'} d\omega \int_0^{s'-\beta R} d\xi' \frac{A'(\xi'/\beta d)}{\sqrt{(x'-\xi')^2-\beta^2R^2}} \quad (34)$$

where

$$\left.\begin{aligned} \omega_* &= \cos^{-1}\frac{1+Y^2-Z^2}{2Y} \\ \omega_*' &= \cos^{-1}\frac{1+Y^2-Z'^2}{2Y} \\ Z' &= (x-B)/\beta d = Z - Z_0 \end{aligned}\right\} \quad (34a)$$

As indicated by Eq. (34), Φ, v_r, and ψ for the source combination can be obtained by superposing two analogous expressions for linear sources, as previously derived.

Since either one of these expressions is regular in the whole flow field, the combination is also regular. Moreover, the combination can be shown to remain finite for $Z \to \infty$, as pointed out at the end of this section.

If one wants to use explicit expressions for ψ, one has to distinguish between the arrangement in which the sinks start in front of the second Mach cone of the sources and the arrangement in which the sinks start behind. (See Figs. 3 and 4.)

As an example, only the first arrangement shall be discussed here. Depending on the various possible positions of the test point P, one may distinguish six cases (see Fig. 8):

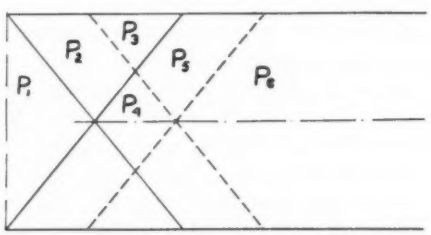

FIG. 8. Districts of flow field occurring in Case C.

Case (1):

$$x < \beta(d-r)$$

Then: $\Phi = 0$.

Case (2):

$$\beta(d-r) < x < \begin{cases} \beta(d+r), \text{ if } 2\beta r < B \\ B+\beta(d-r), \text{ if } 2\beta r > B \end{cases}$$

Then Φ is determined on the basis of source elements alone, and these corresponding to the "front district" only.

Case (3):

$$B+\beta(d-r) < x < \beta(d+r)$$

where $2\beta r > B$.

Then Φ is determined on the basis of source and sink elements corresponding to the respective front districts.

Case (4):

$$\beta(d+r) < x < B+\beta(d-r)$$

where $2\beta r < B$.

Then Φ is determined on the basis of source elements alone, but now these correspond to the rear district.

Case (5):

$$\left.\begin{matrix} B+\beta(d-r), \\ \text{if } 2\beta r < B \\ \beta(d+r), \\ \text{if } 2\beta r > B \end{matrix}\right\} < x < B+\beta(d+r)$$

Then Φ is determined on the basis of source elements corresponding to the rear district and also on the basis of sink elements corresponding to the front district.

Case (6):

$$B+\beta(d+r) < x$$

Then Φ is determined on the basis of both source and sink elements corresponding to their respective rear districts.

Furthermore, as previously explained, $\omega_* = \pi$, if $x > \beta(d+r)$, and $\omega_*' = \pi$, if $x > B+\beta(d+r)$.

Thus, Case (1): $\psi = 0$; Case (2): ψ given by Eq. (30); Case (3): ψ given by a difference of two representations, analogous to Eq. (30), replacing in the second one $s = [Z-(1-Y)]/2Y$ by $s' = [Z'-(1-Y)]/2Y$; Case (4): ψ given by Eq. (32); Case (5): ψ obtained by combining Eq. (32) and a representation derived from Eq. (30) by replacing Z by Z'; Case (6): ψ given by a difference of two representations analogous to Eq. (32), replacing in the second one Z by Z'. It is important to note that by taking the difference, the *logarithmic infinity* of ψ for $Z \to \infty$, as indicated in Eq. (32), *disappears;* for extremely large Z-values, one may write:

$$\psi_6 = \Psi_0 2\sigma' Y^2[(Z_0/Z) + \dots] \quad (35)$$

here $Z_0 = B/\beta d$.

Using the representations of ψ in districts 2, 4, 5, and 6, two different wall contours have been computed and plotted in Fig. 4.

(III) Physical Discussion of Results

(1) Pressure Distribution Inside the Duct

In linearized approximation, the pressure coefficient turns out to be:

$$c_p = \frac{p-p_0}{(1/2)\rho U^2} = -\frac{2v_x}{U}$$

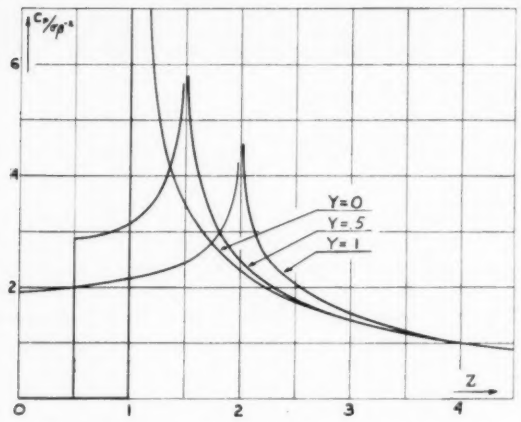

FIG. 9. Pressure distribution for constant sources.

The pressure distribution is known as soon as v_x is determined.

(*a*) *Constant Sources.*—In Case (A) of constant sources, one obtains, by differentiating the perturbation potential Eq. (5) with respect to x:

$$v_x = -2Ad \int_0^{\omega_0} d\omega (x^2 - \beta^2 R^2)^{-1/2} \qquad (36)$$

Eq. (36) turns out to be essentially a complete elliptic integral of the first kind, K. After some transformations, one obtains:

$$c_p^{const.} = 4\beta^{-2}\pi^{-1}\sigma Y^{-1/2} K(k) \qquad (37a)$$

for the front district: $1 - Y \leq Z \leq 1 + Y$; and

$$c_p^{const.} = 4\beta^{-2}\pi^{-1}\sigma Y^{-1/2} k_1 K(k_1) \qquad (37b)$$

for the rear district: $1 + Y \leq Z$.

Here again:

$$k^2 = [Z^2 - (1 - Y)^2]/4Y$$
$$k_1^2 = 4Y/[Z^2 - (1 - Y)^2]$$

On the axis of the skeleton cylinder ($Y = 0$), one obtains from Eq. (36) for the pressure coefficient:

$$c_p^{const.} = 4\beta^{-2}\sigma(Z^2 - 1)^{-1/2} \qquad (38)$$

This holds for the rear region, the front region being restricted to a single point $Z = 1$, $Y = 0$.

From Eq. (37a) we see that, on the front cone ($k = 0$),

$$c_p^{const.} = 2\beta^{-2}\sigma Y^{-1/2} \qquad (39)$$

A discontinuity in the pressure field will develop which represents a conical compression shock that is weak except in the immediate vicinity of the vertex. A comparison of the linearized solution with the solution of the exact differential equation is given at the end of this section.

On the second Mach cone, $k = k_1 = 1$; then the elliptic integrals and c_p become logarithmically infinite. This singularity of the pressure field is due to the fact that the source intensity increases at the entrance rim discontinuously from zero to the value A, corresponding to a finite lip angle, and that this discontinuity is propagated along the characteristic surface. Although the prerequisites of the linearized theory are not fulfilled here, it is explained in Section III, 2, that the region to be excluded from quantitative interpretation is only small.

The graphs of Fig. 9, showing $c_p(Z, Y)$, plotted for $Y = 0$, $1/2$, and 1, give insight into the variation of pressure coefficient inside the duct. The study of this case is an instructive intermediate step before considering the c_p field due to linear sources and that due to the source sink combination described before. One may also note that, in spite of the singularities of the velocity and pressure field, the stream function ψ remains regular, so that the flux balance of the flow pattern is preserved.

(*b*) *Linear Sources.*—In the case of sources with linearly increasing intensity the expression for the pressure coefficient is easily obtained by use of the recurrence theorem proved in Appendix II. Since, by virtue of this theorem:

$$v_x^{lin} = (\beta d)^{-1}\left(\frac{\sigma'}{\sigma}\right)\Phi^{const.} = \left(\frac{\sigma'}{\sigma}\right)\int_{1-Y}^{Z} dZ' v_x^{const.}(Z')$$

one obtains from Eqs. (37a) and (37b):

$$c_p^{lin} = 4\beta^{-2}\pi^{-1}\sigma' Y^{-1/2}\int_{1-Y}^{Z} K(k)\, dZ'$$

for the front region, and

$$c_p^{lin} = c_p^{lin}(1 + Y, Y) + 4\beta^{-2}\pi^{-1}\sigma' Y^{-1/2}\int_{1+Y}^{Z} k_1 K(k_1)\, dZ' \qquad (40b)$$

for the rear region, k and k_1 having the same meaning as previously.

It is clear that, c_p^{lin} being essentially an integral over a function that is finite everywhere except at $Z = 1 + Y$, where it admits a logarithmic singularity, will remain finite for all finite Z-values. The difficulty arising in the case of constant sources is, therefore, removed in the present case.

It is not possible to reduce integrals (40a) or (40b) into a combination of tabulated functions; therefore, approximate methods must be used to evaluate c_p^{lin} at an arbitrary test point. A series expansion for c_p is available, but, because it converges slowly, graphical integration has been preferred.

Still, since the integrand becomes infinite on the second Mach cone ($Z = 1 + Y$), such procedure is applicable only outside the interval $(1 + Y - \mu < Z < 1 + Y + \mu)$, μ being small compared with $(1 + Y)$. To obtain the proper junction, at least two additional values of c_p must be evaluated *analytically*, say $c_p(1 + Y, Y)$ and $c_p(1 + Y + \mu, Y)$. The method used for evaluating these two values of c_p is derived in Appendix III.

Proceeding in the outlined manner, graphs of $c_p^{\text{lin}}(Z, Y)$ were constructed for $Y = 0$, $1/2$, and 1, as shown in Fig. 10. It may be noted that each curve (except that for $Y = 0$) rises gradually with increasing Z, being at first concave and then convex with regard to the Z-axis. On the second Mach cone the curves possess an inflexion point, admitting a *vertical* tangent—i.e., a sudden pressure increment, as in a compression wave. For large Z, all lines are seen to become indistinguishable, and for $Z \to \infty$ they tend logarithmically to infinity.

Again, the case of sources with linearly increasing intensity does not lead to a physically admissible flow pattern. Although c_p is finite at all finite points of the Z–Y-plane, it becomes infinite for large values of Z, which means that the area of the exit section of the stream tubes tends to zero, resulting in an infinite drag.

(*c*) *Source Sink Combination.*—We are now in a position to determine under what conditions an admissible flow pattern may be obtained. Let the source distribution $f(\zeta)$ on the skeleton cylinder be an arbitrary function of ζ, provided that $f(\zeta)$ is continuous everwhere and that $f(0) = 0$. Such a function may be approximated by a superposition of functions of the type:

$$f_n(\zeta) = A_n'(\zeta - \zeta_n), \qquad \text{for } \zeta > \zeta_n$$
$$f_n(\zeta) = 0, \qquad \text{for } \zeta < \xi_n$$

where the ζ_n form an increasing sequence. Let $c_{pn}(Z)$ be the corresponding pressure field. If

$$f(\zeta) = \sum_{n=1}^{N} f_n(\zeta)$$

then

$$\bar{c}_p(Z) = \sum_{n=1}^{N} c_{pn}(Z)$$

where c_p is the pressure distribution corresponding to the source distribution $f(\zeta)$. Since the c_{pn} are finite everywhere except for $Z \to \infty$, $\bar{c}_p$ is likewise finite. For $Z \to \infty$, one obtains, by using the series (32) for $(1/Y)(\partial\psi^{\text{lin}}/\partial Y)$, which according to Eq. (12b) is proportional to v_x^{lin}:

$$\bar{c}_p = 4\beta^{-2}\left[\sum_{n=1}^{N} \sigma_n' \log 2(Z - \zeta_n) - \left(\frac{1}{4}\right)(1 + Y^2)\sum_{n=1}^{N}\frac{\sigma_n'}{(Z-\zeta_n)^2} + \left(\frac{3}{32}\right)\times (1 + 4Y^2 + Y^4)\sum_{n=1}^{N}\frac{\sigma_n'}{(Z-\zeta_n)^4} + \cdots\right] \quad (41)$$

with

$$\sigma_n' = A_n'\beta\pi/U$$

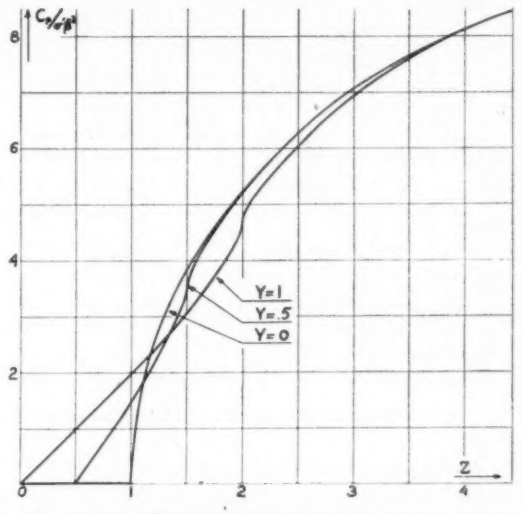

FIG. 10. Pressure distribution for linearly increasing sources.

A more involved argument shows that $\bar{c}_p$ finally takes the form:

$$\bar{c}_p = 4\beta^{-2}\left[\left(\sum_{n=1}^{N}\sigma_n'\right)\log 2Z + \sum_{s=1}^{\infty}\frac{f_s(Y)}{Z^s}\right] \quad (42)$$

where $f_s(Y)$ are polynomials in Y of order $2s$, which remain bounded for $Y \leq 1$ as $s \to \infty$.

From Eq. (42) it is evident that, for $Z \to \infty$, c_p will remain finite *only* if $\sum_{n=1}^{N}\sigma_n' = 0$—i.e., $\sum_{n=1}^{N} A_n' = 0$. If this is the case, then

$$\lim_{Z\to\infty} \bar{c}_p(Z, Y) = 0$$

The meaning of the above is that, in order to eliminate all the singularities that may eventually arise in the flow pattern, the source intensity function $f(\zeta)$ has to be selected so as to approach a constant value for large ζ-values and to vanish for $\zeta = 0$.

As an instructive application, one may consider again the superposition of *two* linear source distributions—namely,

$$N = 2; \qquad A_1' = -A_2' = A'$$
$$\xi_1 = 0; \qquad \xi_2 = B$$

Putting $B/\beta d = 0.25$ and 2.0, respectively, graphs of $c_p(Z)$ for $Y = 0$, $1/2$, and 1 are shown in Fig. 11. One can notice a relation between the form of the wall contour and the pressure distribution along the Z-direction. Beginning at the rim, there starts naturally a slow compression, indicated by a rising c_p; in the region where the duct wall becomes convex toward the axis (front district of sinks), the c_p rise is almost annulled. At the second Mach cone of the sources (shortly behind the throat), a sudden pressure increment occurs, indicating the formation of a compression wave due to

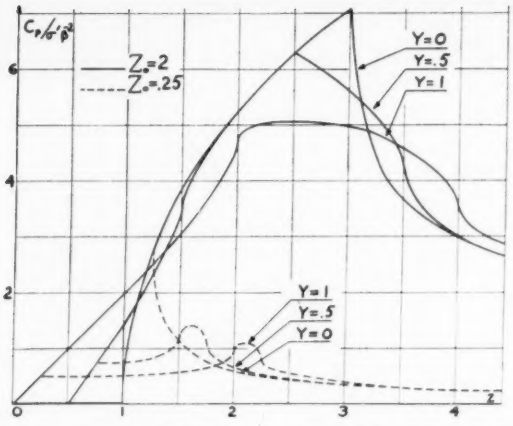

FIG. 11. Pressure distribution for source sink combinations.

the combined effect of all parts of the rim. At the second Mach cone of the sinks (near the inflexion point of the wall contour), a sudden pressure drop occurs, indicating the formation of an expansion wave.

(*d*) *The Drag.*—Application of the momentum theorem to the fluid in the interior of the duct yields, for the drag:

$$D = A_0(p_0 + \rho_0 V_0^2) - A_1(p_1 + \rho_1 V_1^2)$$

where V stands for the total velocity and the subscripts 0 and 1 refer to the entrance and exit sections of the duct. It had been shown previously that for Case (A) of constant sources and in Case (C) of the source sink combination $A_0 = A_1$, $V_0 = V_1$, and $\rho_0 = \rho_1$.

The discussion of the last paragraph has shown that for Cases (A) and (C): $c_p(\infty) = 0$—i.e., $p_0 = p_1 = 0$. Therefore, $D = 0$.

As mentioned before, in the Case (B) of linear sources, $D = \infty$.

(2) *Constant Source Distribution as Limiting Case of Source Sink Combination*

As mentioned in the Introduction, the velocity and pressure field, produced by a distribution of constant sources (A), may be considered as limiting case of the more general flow pattern produced by the source sink combination (C). Qualitatively, this might be anticipated by comparing the pressure curves in Figs. 9 and 11. Upon reducing the distance B, between sources and sinks, gradually to zero, the pressure increments indicating the compression and subsequent expansion waves, which are at distance B in Fig. 11, approach each other, until, in the limit $B \to 0$, described by Fig. 9, the expansion wave follows the compression wave immediately without interval. During this limiting process the pressure values between the two waves increase gradually beyond any bound; this indicates, on the other hand, that these c_p values obtained during the limiting process are outside of the linearized theory. However, if the limiting process is not carried to the end, the c_p values remain permissible within the linearized theory and indicate approximately the true form of the pressure curves.

Consider once more the source distribution (C), represented in Fig. 12 and resolved into a combination of sources and sinks that are a distance B apart from each other. While reducing B but keeping $(B/\beta d)A' = A$ = constant, A' must increase indefinitely; thus, for sufficiently small B values, the intensities $\pm A'$ of the linear sources and sinks (i.e., the slopes of the two parallel lines) will become so large that the prerequisites are no longer fulfilled for applying the linearized theory to test points P lying inside stripes of width B, adjacent to the first and second Mach cones.

It is instructive to verify quantitatively that the formulas derived for the source sink combination [Case (C)] become, in the limit $B \to 0$, identical with the formulas derived for constant sources [Case (A)].

Symbolically, the velocities of the source sink combination may be written in the form:

$$\lim_{B\to 0} \Delta_B v^{\text{lin}}(x) = \lim_{B\to 0} [v^{\text{lin}}(x) - v^{\text{lin}}(x - B)]$$

and after expanding in the vicinity of $B = 0$:

$$\lim_{B\to 0} \Delta_B v^{\text{lin}}(x) = \lim_{B\to 0} \left[B\left(\frac{\partial v^{\text{lin}}}{\partial x}\right)\right]$$

Now $(B/\beta d) = A/A'$, so that, by use of the recurrence theorem,

$$\lim_{B\to 0} \Delta_B v^{\text{lin}}(x) = (\beta d A/A')\frac{\partial v^{\text{lin}}}{\partial x} = v^{\text{const}}(x)$$

One may also carry out this check for front and rear district explicitly and follow up, in detail, how in the limit $B \to 0$ the singularities at the first and second Mach cones gradually build up. (This is shown in Appendix IV.) But the true behavior of the pressure field is better approximated by considering the c_p curve obtained with finite B.

It is interesting to note that the occurrence of a compression wave followed closely by an expansion wave, as well as the singular behavior of the pressure field, if the two waves follow each other directly, also occurs in supersonic flow about slender bodies of revolution. If, following von Kármán and Moore, we put linear sources and, a distance B behind, linear sinks on the

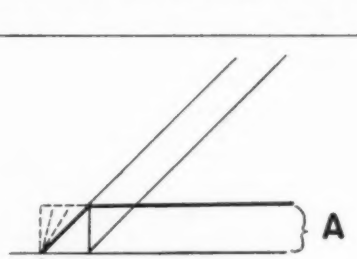

FIG. 12. Case (A) as limit of Case C. $B \to 0$

axis of an ogive, the pressure field shows also in this case a pressure rise, followed by a pressure drop, a distance B thereafter. Again, if distance B is gradually reduced to zero, the pressure increments indicating the compression and expansion, approach each other and grow beyond any bound. In this case, the conical surface, originating at the tip of the ogive and representing an attached shock wave, appears in the linearized theory as singularity of the flow field, at which c_p becomes infinite as $1/\sqrt{1 - (\beta r/x)^2}$. Again, the true behavior of the pressure field is better approximated by considering the c_p curve obtained with finite B.

(3) *Computation of the Form of Entrance Shock, in Second Approximation*

In the preceeding section the singularities of the flow field, produced by constant sources have been shown to build up gradually during a limiting process that allows to interpret actual conditions in a qualitative manner. In the present consideration, an attempt will be made to give further elucidation by computing the form of the entrance shock in second approximation and by comparing these results with Ferri's[6] analysis, carried out by means of the method of characteristics. Among other things, Ferri has shown that, for small lip angles δ, there is a front shock and a reflected shock, each of which has an almost conical shape,* as expected from the linearized theory. According to Fig. 8 of Ferri's paper, a lip angle of 5° produces shock fronts, the curvature of which is slight except in the immediate vicinity of the vertex of the double cone, this vertex region covering approximately 1 per cent of the total area of the shock. One can also read off from Fig. 8 that the velocity increment across the front shock follows approximately a $Y^{-1/2}$-law, if one does not approach the axis closely.

From the linearized theory, a first idea of the curvature of the shock front may be obtained by inserting the velocity field obtained heretofore into the equations of the shock polar.[7] These equations express the slope of the shock front λ in terms of the velocity components before and behind the shock front:

$$\left.\begin{aligned} u_2 &= (1 - \mu^2)u_1 \cos^2\lambda + (c_*^2/u_1) \\ v_2 &= -[(1 - \mu^2)u_1 \cos^2\lambda - u_1 + \\ &\qquad c_*^2/u_1] \cot\lambda = (u_1 - u_2)\cot\lambda \end{aligned}\right\} \quad (43)$$

here

$$\begin{aligned} u_1 &= U \\ c_*^2 &= (U^2/M^2)(\beta^2\mu^2 + 1) \\ \mu^2 &\quad (\gamma - 1)/(\gamma + 1) \end{aligned}$$

For u_2 and v_2, the velocity components behind the shock, we substitute the values, at the Mach lines, as obtained from our linearized theory:

* Interferometric pictures of a supersonic jet, emerging from a circular nozzle, taken by R. Ladenburg,[8] show clearly compression and expansion waves forming a pointed double cone.

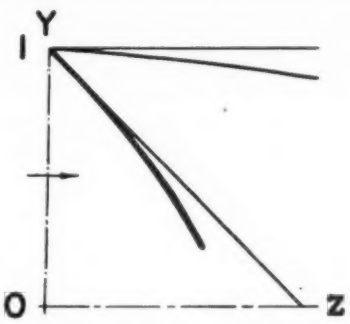

FIG. 13. Shock form, in second approximation.

$$u_2 = v_x = U - \frac{\pi A}{\beta\sqrt{Y}} = U\left(1 - \frac{\delta}{\beta\sqrt{Y}}\right)$$

$$v_2 = v_r = -\frac{\pi A}{\sqrt{Y}} = -\frac{\delta U}{\sqrt{Y}}$$

here, δ is again the lip angle of the duct, which, according to Eq. (24), is σ/β.

The solution of either one of Eqs. (43), yields, up to the first power of δ (δ considered small):

$$\tan\lambda = \pm\frac{1}{\beta}\left(1 + \frac{\delta M^4}{2\beta^3(1 - \mu^2)\sqrt{Y}}\right) = \frac{dY}{dZ} \quad (44)$$

which, when integrated, yields as equation for the approximate shock line:

$$Z = (1 - Y) - \frac{\delta M^4}{2\beta^3(1 - \mu^2)}(1 - \sqrt{Y}) \quad (45)$$

in qualitative agreement with the exact theory. (See Fig. 13.) It is evident that this result is valid only in a region not too far from the nozzle wall, since in the solution procedure use was made of the smallness of δ—i.e., the smallness of u_2 and v_2. In the immediate neighborhood of the wall, the expression (44) for λ can even be shown to be a solution, if one uses the exact differential equation.

Proceeding further along this line, higher approximations of the velocity and pressure field, near the shock, can be computed. With these corrections, it can be shown that the singular values of v and c_p, at the axis, disappear.

(4) *Comparison with Measurements*

It is, of course, desirable to compare the results of the theory with available measurements. Obviously, such comparison can be carried out more successfully after the "inverse problem" has been solved so that the pressure field of an experimentally given nozzle shape can be computed. This will be done in a separate paper (see dissertation of Ch. Mack).

Appendix I: Proof Showing That Eq. (2) Fulfills the Axial Symmetrical Potential Equation for Supersonic Flow

It is known that the Laplace equation (in cylindrical coordinates) is fulfilled by the velocity potential of an incompressible source:

$$\Phi = -c/\sqrt{(x-\xi)^2 + R^2} \tag{A1}$$

where c is the source strength, $(x - \xi)$ is the axial distance, and R is the radial distance between P and the source element, as before. Suppose that incompressible sources of constant intensity c are spread over a cylindrical surface of axial length L, which is subdivided into two parts: a cylinder covered by sources $0 \leq \xi \leq x$, and another one covered by sources $x \leq \xi \leq L$. The contributions of the two cylinders to the potential at $P(x, r)$ shall be considered separately. The solution, representing the contribution of the first cylinder, assumes the form:

$$\Phi = -2d \int_0^{\omega_*} d\omega \int_0^x d\xi \frac{f(\xi)}{\sqrt{(x-\xi)^2 + R^2}} \tag{A2}$$

This expression will certainly fulfill the axial symmetrical form of the Laplace equation:

$$\frac{\partial^2\Phi}{\partial x^2} + \frac{\partial^2\Phi}{\partial r^2} + \frac{1}{r}\frac{\partial\Phi}{\partial r} = 0 \tag{A3}$$

From the point of view of the theory of complex functions, x and ξ may assume complex values and still fulfill differential Eq. (A3). Therefore, if we substitute

$$x - \xi = (1/i\beta)(x' - \xi') \tag{A4}$$

where x' and ξ' are real variables, then we get a solution of the form:

$$\Phi = -2d \int_0^{\omega_*} d\omega \int_0^{x'} d\xi' \frac{f(\xi')}{\sqrt{(x'-\xi')^2 - \beta^2R^2}} \tag{A5}$$

obeying the differential equation,

$$\beta^2\frac{\partial^2\Phi}{\partial x'^2} - \frac{\partial^2\Phi}{\partial r^2} - \frac{1}{r}\frac{\partial\Phi}{\partial r} = 0 \tag{A6}$$

which turns out to be the equation determining the supersonic velocity potential.

It is easily seen that Eq. (A5) becomes imaginary for $\xi' > x' - \beta R$. Therefore, the value of Φ will be complex. Since the real, as well as the imaginary, part of Φ has to satisfy the differential equation separately, one may conclude that Eq. (A6) is fulfilled also by:

$$\Phi = -2d \int_0^{\omega_*} d\omega \int_0^{x-\beta R} d\xi \frac{f(\xi)}{\sqrt{(x-\xi)^2 - \beta^2R^2}} \tag{A7}$$

which is the desired, real value of the velocity potential.

The contributions of the second cylinder covered by sources $x \leq \xi \leq L$ to Φ is zero, since sources downstream of P cannot possibly influence Φ according to the laws of supersonic flow.

Appendix II: A Recurrence Theorem, of Use in Supersonic Source Distributions on Cylindrical Surfaces

Let Φ_I be the potential at the point (x, r) due to a distribution of sources or sinks of local intensity $f(\xi)$, $\xi \geq 0$ on a skeleton cylinder, viz.:

$$\Phi_I = -2d \int_0^{\omega_*} d\omega \int_0^{x-\beta R} d\xi \frac{f(\xi)}{\sqrt{(x-\xi)^2 - \beta^2R^2}} \tag{A8}$$

where $R^2 = d^2 + r^2 - 2dr\cos\omega$, and $R(\omega_*) = x/\beta$, if (x, r) is located in the front district, or $\omega_* = \pi$, if (x, r) is located in the rear district. Φ_I is a solution of the partial differential equation:

$$\frac{\partial^2\Phi}{\partial r^2} + \frac{1}{r}\frac{\partial\Phi}{\partial r} - \beta^2\frac{\partial^2\Phi}{\partial x^2} = 0 \tag{A9}$$

If we put

$$F(x, R) = \int_0^{x-\beta R} d\xi \frac{f(\xi)}{\sqrt{(x-\xi)^2 - \beta^2R^2}} \tag{A10}$$

then

$$\Phi_I = -2d \int_0^{\omega_*} d\omega F(x, R)$$

Integrating Eq. (A10) by parts, we obtain:

$$F(x, R) = \left\{ f(\xi) \log \left[(x-\xi) + \sqrt{(x-\xi)^2 - \beta^2R^2}\right] \right\}_{\xi=0}^{\xi=x-\beta R} +$$

$$\int_0^{x-\beta R} d\xi f'(\xi) \left\{ \log \left[(x-\xi) + \sqrt{(x-\xi)^2 - \beta^2R^2}\right] \right\}$$

or

$$F(x, R) = f(0) \log \left(x + \sqrt{x^2 - \beta^2R^2}\right) - f(x - \beta R) \log (\beta R) + \int_0^{x-\beta R} d\xi f'(\xi) \log \left[(x-\xi) + \sqrt{(x-\xi)^2 - \beta^2R^2}\right] \tag{A11}$$

Now,

$$(v_r)_I = \frac{\partial\Phi_I}{\partial x} = -2dF[x, R(\omega_*)]\frac{\partial\omega_*}{\partial x} - 2d\int_0^{\omega_*} d\omega \frac{\partial F(x, R)}{\partial x} \tag{A12}$$

However, in the front district, $R(\omega_*) = x/\beta$ and $F[x, R(\omega_*)] = 0$; whereas in the rear district, $\omega_* = \pi$ and $\partial\omega_*/\partial x = 0$; hence,

$$(v_r)_I = -2d \int_0^{\omega_*} d\omega \frac{\partial F(\omega, R)}{\partial x} \tag{A12a}$$

and after substituting $F(x, R)$ from Eq. (A11):

$$(v_x)_{\mathrm{I}} = -2d\int_0^{\omega_*} d\omega\left[\frac{f(0)}{\sqrt{x^2-\beta^2R^2}} + \int_0^{x-\beta R} d\xi\,\frac{f'(\xi)}{\sqrt{(x-\xi)^2-\beta^2R^2}}\right] \quad \text{(A13)}$$

Now, consider a *second* source distribution $g(\xi)$ related to the first by

$$g(\xi) = (1/L)\int_0^{\xi} f(\xi')d\xi' \quad \text{(A14)}$$

where L is some characteristic length. Obviously, $g(0) = 0$ and $g'(\xi) = (1/L)f(\xi)$. Let Φ_{II} be the potential due to this new source distribution. Then the expression (A13) certainly applies to $g(\xi)$ and Φ_{II}—i.e.,

$$\frac{\partial\Phi_{\mathrm{II}}}{\partial x} = (v_x)_{\mathrm{II}} = -2\frac{d}{L}\int_0^{\omega_*} d\omega\int_0^{x-\beta R}\times d\xi\,\frac{f(\xi)}{\sqrt{(x-\xi)^2-\beta^2R^2}}$$

which is equal to Eq. (A8), except for the factor $1/L$. Thus, in general, front and rear:

$$\partial\Phi_{\mathrm{II}}/\partial x = (v_x)_{\mathrm{II}} = (1/L)\Phi_{\mathrm{I}} \quad \text{(A15)}$$

provided that the source distribution corresponding to Φ_{II} is related to the source distribution corresponding to Φ_{I} by Eq. (A14).

Now, according to Eq. (12b) and Eq. (A15):

$$\psi_{\mathrm{I}} = -\rho_0\beta^2\int_0^r dr'\,r'\frac{\partial\Phi_{\mathrm{I}}}{\partial x} = -\rho_0\beta^2L\int_0^r dr\quad\frac{\partial^2\Phi_{\mathrm{II}}}{\partial x^2} \quad \text{(A16)}$$

Since, however, Φ_{II} is a solution of the partial differential Eq. (A9):

$$\beta^2\frac{\partial^2\Phi_{\mathrm{II}}}{\partial x^2} = \frac{\partial^2\Phi_{\mathrm{II}}}{\partial r^2} + \frac{1}{r}\frac{\partial\Phi_{\mathrm{II}}}{\partial r} = \frac{1}{r}\frac{\partial}{\partial r}\left(r\frac{\partial\Phi_{\mathrm{II}}}{\partial r}\right) = \frac{1}{r}\frac{\partial}{\partial r}(rv_{\mathrm{II}}) \quad \text{(A17)}$$

we obtain, by substituting Eq. (A17) into (A16):

$$\psi_{\mathrm{I}} = -\rho_0 Lr(v_r)_{\mathrm{II}} \quad \text{(A18)}$$

In order to determine L, consider the case of constant and linear sources: Let

$$f(\xi) = A = U\sigma/\beta\pi \qquad \text{(constant sources)}$$

and

$$g(\xi) = A'(\xi/\beta d) = (U/\beta\pi)\sigma'(\xi/\beta d) \qquad \text{(linear sources)}$$

Obviously, then,

$$g(\xi) = \frac{1}{\beta d}\left(\frac{\sigma'}{\sigma}\right)\int_0^{\xi} f(\xi')d\xi'$$

and comparing this relation with Eq. (14),

$$L = \beta d(\sigma/\sigma')$$

Hence, finally, from Eqs. (A15) and (A18) we obtain:

$$v_x^{\mathrm{lin}} = (\beta d)^{-1}(\sigma'/\sigma)\Phi_{\mathrm{const.}} \quad \text{(A19)}$$

$$\psi_{\mathrm{const.}} = -\rho_0 d\beta\left(\frac{\sigma}{\sigma'}\right)rv_r^{\mathrm{lin}} = -\rho_0 d^2\beta\left(\frac{\sigma}{\sigma'}\right)Yv_r^{\mathrm{lin}} \quad \text{(A20)}$$

and with Eq. (12b):

$$\psi^{\mathrm{lin}} = (\sigma'/\sigma)\int_{1-Y}^{Z} dZ'\,\psi_{\mathrm{const.}} \quad \text{(A21)}$$

These formulas have been used in the text.

Appendix III: A Method for Evaluating c_p^{lin} at the Points (1) $Z = 1 + Y$, Y and (2) $Z = 1 + Y + \mu$, Y, Where $\mu/Y \ll 1$

(1) On the second Mach cone, a well-converging series expansion has been derived. It can be shown that, after some transformations, Eq. (40a) for c_p^{lin} assumes the form:

$$c_p^{\mathrm{lin}}(1 + Y, Y) = 4\sigma'\pi^{-1}\beta^{-2}I(1 + Y, Y) \quad \text{(A22)}$$

here,

$$I(1 + Y, Y) = \int_0^{\pi/2} d\theta\,\log\frac{1 + \gamma\cos\theta}{1 - \gamma\cos\theta} \quad \text{(A23)}$$

and $\gamma = 2\sqrt{Y}/(1 + Y)$. For $\gamma = 0$—i.e., $Y = 0$—Eq. (A23) gives immediately, $I = 0$. Observing that for $Y = 1$, $\gamma = 1$ and that for $Y = 1/2$, $\gamma = 0.94$, we introduce a new parameter ϵ, defined by

$$\epsilon = 1 - \gamma = (1 - \sqrt{Y})^2/(1 + Y)$$

and rewrite Eq. (A23) as

$$I(1 + Y, Y) = 2I_1 + I_2 + 2I_3$$

with

$$\left.\begin{aligned} I_1 &= \int_0^{\pi/2} d\theta\,\log(1 + \cos\theta) = \\ &\quad -(\pi/2)\log 2 + 2\sum_{n=0}^{\infty}\frac{(-1)^n}{(2n+1)^2} = \\ &\quad 1.83 - (\pi/2)\log 2 \\ I_2 &= -\int_0^{\pi} d\theta\,\log(1 + \gamma\cos\theta) = \\ &\quad \pi\log(1 + Y) \\ I_3 &= \int_0^{\pi/2} d\theta\,\log\left[1 - \epsilon\left(\frac{\cos\theta}{1 + \cos\theta}\right)\right] = \\ &\quad -\sum_{n=1}^{\infty}\frac{\epsilon^n}{n}\int_0^{\pi/2} d\theta\,\sum_{m=0}^{n}(-1)^m\frac{C_n^m}{(1 + \cos\theta)^m} \end{aligned}\right\} \quad \text{(A24)}$$

where C_n^m = binomial coefficients = $n!/m!(n - m)!$.

The integrals involved may be computed by means of a recurrence relation giving

$$S_m = \int_0^{\pi/2} \frac{d\theta}{(1+\cos\theta)^m} = \frac{1}{2m-1} + \frac{m-1}{2m-1} S_{m-1}$$

Hence,

$$I_3 = -0.571\epsilon - 0.119\epsilon^2 - 0.035\epsilon^3 - \ldots$$

and, finally, for $c_p(1+Y, Y)$:

$$c_p(1+Y, Y) = 4\pi^{-1}\beta^{-2}\sigma'[\pi \log\left(\frac{1+Y}{2}\right) + 3.68 - 1.142\epsilon - 0.238\epsilon^2 - 0.070\epsilon^3 - \ldots]$$

In particular:

$Y = 1, \epsilon = 0$	$c_p/4\beta^{-2}\pi^{-1}\sigma' = 3.68$
$Y = 1/2, \epsilon = 0.06$	$= 2.77$
$Y = 0, \epsilon = 1, \gamma = 0$	$= 0.00$

(2) To evaluate $c_p(1+Y+\mu, Y)$, closely behind the second Mach cone, set in Eq. (40*a*) and (40b) for $K(k_1)$:

$$K(k_1) \sim \log(4/k_1')$$

change the variable of integration from Z to $\mu = Z - (1+Y)$, expand the integrand into a series of the type $\sum_n (\alpha_n + \beta_n \log\mu)\mu^n$, and integrate. This yields, approximately,

$$c_p(1+Y+\mu, Y) = c_p(1+Y, Y) + 2\beta^{-2}\pi^{-1}\sigma' Y^{-1/2}\left\{\mu\left(1 + \log\frac{32Y}{1+Y} - \log\mu\right) + \frac{1+Y}{8Y}\mu^2\left[\frac{3+2Y+3Y^2}{2(1+Y)^2} - \log\frac{32Y}{1+Y} + \log\mu\right] + \ldots\right\}$$

This expression is valid for $\mu/\sqrt{Y} \ll 1$ and yields, for $\mu = 0.05$, $Y = 1$—i.e., $Z = 2.05$—

$$c_p = 4\pi^{-1}\beta^{-2}\sigma'(3.68 + 0.228)$$

for $\mu = 0.05$, $Y = 1/2$—i.e., $Z = 1.55$—

$$c_p = 4\pi^{-1}\beta^{-2}\sigma'(2.77 + 0.229)$$

For $Y = 0$, when the above formula becomes invalid, a closed formula may be easily obtained; using Eq. (38) one gets:

$$C_p = 4\beta^{-2}\sigma' \int_1^Z \frac{dz'}{\sqrt{Z'^2-1}} = 4\beta^{-2}\sigma' \log\left(Z + \sqrt{Z^2-1}\right) \quad \text{(A25)}$$

After the values of c_p at $Z = 1 + Y + \mu$ have been determined analytically, the remainder of the $c_p^{\text{lin}} =$ curves can again be obtained by graphical integration. Since, however, such a procedure leads to a cumulative error and since the curves $c_p(Z, Y = \text{constant})$ approach each other asymptotically for large values of Z, it is necessary to check their respective positions. Such check is readily obtained, since a series expansion for c_p after Z^{-1} is available.

Using Eq. (32), we obtain:

$$c_p^{\text{rear}} = -\frac{2v_x^{\text{lin}}}{U} = -\frac{2}{\rho_0 U d^2 \beta^2 Y}\left(\frac{\partial\psi}{\partial Y}\right) = 4\beta^{-2}\sigma'\left[\log 2Z - \frac{1}{4Z}(1+Y^2) + \frac{3}{32Z^4}\times(1+4Y^2+Y^4) + \ldots\right] \quad \text{(A26)}$$

Hence, for large values of Z, the c_p-curves become asymptotic with Eq. (A25) and

$$\frac{c_p(Z, U) - c_p(Z, Y')}{Y - Y'} < 0$$

for Z large enough. By means of Eq. (A26), the following values were found for $Z = 10$:

$Y = 0$	$c_p^{\text{lin}}/4\pi^{-1}\beta^{-2}\sigma' = 9.4035$
$= 0.5$	$= 9.4015 (9.433)$
$= 1.0$	$= 9.3955 (9.423)$

For comparison, the figures obtained by graphical integration are placed in parentheses.

Appendix IV: Proof Showing that the Velocities at First and Second Mach Cone, Obtained in Case C, Become, in Limit $B \to 0$, Identical with Velocities Obtained in Case A

Using the front representations [Eq. (30)] of sources and sinks [district (3)], one obtains:

$$\Delta_B v_r^{\text{lin}}(x) = v_r^{\text{lin}}(x) - v_r^{\text{lin}}(x-B) = -2\beta^{-1}U\sigma' U Y^{1/2}\{s[1 - c_1(Y)s - c_2(Y)s^2 - \ldots] - s'[1 - c_1(Y)s' - c_2(Y)s'^2 - \ldots]\}$$

$$= -2\beta^{-1}U\sigma' Y^{1/2}(s-s')\times[1 - c_1(Y)(s+s') - c_2(Y)(s^2+2ss'+s'^2) - \ldots]$$

Now

$$s - s' = \Delta s = \frac{B}{\beta(2r)} = \frac{A}{A'(2Y)}$$

so that

$$\Delta_B v_r^{\text{lin}}(s) = \Delta s[\Delta v_r^{\text{lin}}(s)/\Delta s = -A\pi Y^{-1/2}[1 - c_1(Y)(s+s') + \ldots]$$

and

$$\lim_{B\to 0} \Delta_B v_r^{\text{lin}}(s) \to -A\pi Y^{-1/2} = (v_r^{\text{const.}})_{s=0}$$

As long as B is not yet zero, district (3), in which the above representation holds, does not contain the point $Y = 0$, $Z = 1 - Y$, and no singularity in the flow field arises.

In the vicinity of the second Mach cone, using the rear district representations (32) [district (6)], one may

check on how, in the limit $B \to 0$, the logarithmic singularity of the velocity field gradually builds up:

$$\Delta_B v_r^{\text{lin}}(x) = \frac{A'}{Y} \int_b^a \frac{d\rho}{\rho} \left[\frac{1}{\sqrt{(a-\rho)(\rho-b)}} \right] \times (\sqrt{c-\rho} - \sqrt{c'-\rho})$$

where $c = Z^2$ and $c' = (Z - Z_0)^2$. After expanding,

$$\Delta_B v_r^{\text{lin}} = \frac{A'}{Y} \left(\frac{dc}{dx}\right) \int_b^a \frac{d\rho}{\rho} \left[\frac{1}{\sqrt{(a-\rho)(\rho-b)}} \right] \times \frac{d}{dc} \sqrt{c-\rho} + \dots$$

$$= \left(\frac{BA'}{Y}\right) Z(\beta d)^{-1} \int_b^a \frac{d\rho}{\rho} \times \left[\frac{1}{\sqrt{(a-\rho)(\rho-b)(c-\rho)}} \right]$$

Putting $(B/\beta d)A' = A$, as before:

$$\Delta_B v_r^{\text{lin}} = AZY^{-1} \int_b^a \frac{d\rho}{\rho} \left[\frac{1}{\sqrt{(a-\rho)(\rho-b)(c-\rho)}} \right]$$

Therefore, again,

$$\Delta_B v_r^{\text{lin}} = \Delta s \left(\frac{\Delta v_r^{\text{lin}}}{\Delta s} \right) = v_r^{\text{const.}} + \dots$$

and

$$\lim_{B \to 0} \Delta s \frac{\Delta v_r^{\text{lin}}}{\Delta s} \to \log [Z^2 - (1 + Y)^2]$$

As long as B is not yet zero, one has to take the difference quotient, $\Delta s(\Delta v^{\text{lin}}/\Delta s)$, instead of the derivative $(A/A')(\partial v^{\text{lin}}/\partial z)$; in this case, the above representation, which is only valid for test points lying in the rear districts of *both* sources and sinks, does not include any position of P, for which $Z = 1 + Y$. In the limit $B \to 0$, c is allowed to become equal to a, and the expression in the denominator of the integrand indicates that a logarithmic singularity will be formed. But the true behavior of the pressure field is better approximated by considering the c_p curve obtained with finite B.

References

[1] von Kármán and Moore, Trans. A.S.M.E., June, 1932.

[2] Mack, Ludloff, and Reiche, Journal of Applied Physics, Vol. 18, p. 682, 1947.

[3] Friedrichs, K. O., *Lecture on Fluid Dynamics*, New York University, 1941.

[4] Mack, Ch., Doctoral Dissertation, New York University, 1947.

[5] Ferri, A., N.A.C.A., T.N. No. 1135, 1946.

[6] Ladenburg, Voorhis, and Winckler, Nav. Ord. Report 69-46, 1946.

[7] Applied Mathematics Group, New York University: *Supersonic Flow and Shock Waves*, AMG-NYU No. 62, 1944.

Announcing a New Department . . . Readers' Forum

It has been suggested by several members of the I.A.S. Editorial Committee that the *Journal* open a special department to fill the need for the more immediate communication of essential results of research in the greatly expanded and accelerated fields of the aeronautical sciences. Therefore, it has been decided to establish a new department, the "Readers' Forum," to include letters to the editor for the quick publication of (1) brief reports of important findings in aeronautical sciences and (2) discussions of papers published in the *Journal*.

Specifications for Submission of Material

(1) All letters should be accompanied by a suggested short title, giving some indication to the reader of the subject under discussion.

(2) These letters should not exceed 800 words in length.

(3) Publication will be completed 6 to 8 weeks after receipt of the material.

(4) The Editorial Committee will not hold itself responsible for the opinions expressed by the correspondents, and no proofs will be sent to the authors.

(5) All letters should be double-spaced.

The new department starts with this issue of the *Journal*. (See pages 62–64.) Contributions should be sent to:

Editor, Journal of the Aeronautical Sciences
2 East 64th Street
New York 21, New York

Two-Dimensional Airfoils in Hypersonic Flows*

RICHARD D. LINNELL†

Massachusetts Institute of Technology

SUMMARY

Equations for the force and moment coefficients of a sharp-edged two-dimensional airfoil are developed on the basis of Tsien's hypersonic similarity law. The coefficients are calculated for a flat plate and for three airfoils with thickness. The optimum airfoil is a wedge whose lower surface is flat, with the maximum thickness at mid-chord. The results are valid when the product of the Mach Number and the thickness ratio is of the order of 1.

INTRODUCTION

HYPERSONIC FLOWS are flow fields where the fluid velocity is much larger than the velocity of sound. Hypersonic flows have been treated qualitatively, usually on the basis of the limiting case of an infinite value of the free-stream Mach Number, M^0, which is defined as the ratio of the undisturbed fluid velocity to the velocity of propagation of small disturbances, the velocity of sound. Von Kármán[1] has considered this case when γ, the ratio of specific heats, is 1, for which the relations are particularly simple. He points out that in many ways the dynamics of hypersonic flows is similar to Newton's corpuscular theory of aerodynamics. The pressure acting on an inclined surface is thus greater than the free-stream pressure by a quantity that is approximately proportional to the square of the angle of inclination, instead of the usual linear law of conventional flows. Sänger[2] has used this concept to design the best wing and body shapes for flight at an infinite value of M^0. The qualitative approach, however, is not satisfactory for hypersonic flows whose free-stream Mach Number is finite.

Tsien[3] has developed the similarity laws for hypersonic flows. An affine transformation which expands the flow field laterally, reduces the equations of the flows to a single nondimensional equation. If a series of bodies having the same thickness distribution but different small thickness ratios, δ, are put into different flows such that the parameter $K = M^0\delta$ remains constant, and at angles of attack, α, such that the ratio α/δ remains constant, then the flows are similar in that they are governed by the same transformed velocity potential. K must be of the order of 1.

The hypersonic similarity laws state that the force and moment coefficients for two-dimensional flows can be expressed in the forms

$$C_l = \delta^2 L(K)$$
$$C_d = \delta^3 D(K)$$
$$C_m = \delta^2 M(K)$$

The purpose of this paper is to determine the functions L, D, and M for two-dimensional airfoils.

THE PRESSURE COEFFICIENT

According to the hypersonic similarity law, the pressure coefficient on the surface of an airfoil in a two-dimensional flow can be written in the form

$$C_p = \delta^2 P(K, \xi)$$

Here δ is the thickness ratio of the body, the ratio of the maximum thickness of the body to its length; K is a parameter defined by $K = M^0\delta$; and ξ, a nondimensional coordinate along the chord, is defined by the affine transformation

$$x = b\xi$$
$$y = b\delta\eta$$

of the fluid field. In the x, y axes the midpoint of the body length is at the origin. Its chord, of length $2b$, is on the x-axis.

The pressure at a point on the surface of the airfoil will depend on the free-stream pressure p^0, on the pressure change due to an oblique shock attached to the leading edge to a pressure p_s, and on the pressure change through isentropic expansion to the point on the airfoil and a pressure p. Thus, two relations $(p_s/p^0)(M^0\theta_s)$ and $(p/p_s)(M^0\theta_s, M^0\theta_e)$, must be determined. θ_s is the deflection angle produced by the shock, and θ_e is the angle through which the flow expands.

$M^0\theta_s$ enters in the expansion pressure ratio through the Mach Number after the shock, M_s, which will be the initial Mach Number of the expansion. M_s is determined by the conditions of the shock, so $M_s(M^0\theta_s)$ must be found.

θ_s is a function of the angle of attack and of the slope of the body at the leading edge. It does not vary with ξ. θ_e, however, is a function of the angle of attack and of the thickness distribution along the chord. It is then a function of ξ. After these relations, in addition to the pressure ratios, have been found, the pressure coefficient can be written in terms of K and ξ.

Received June 15, 1948.

* The material in this paper is taken from a Master's thesis at the Massachusetts Institute of Technology, prepared during the winter of 1948 under the direction of Prof. H. S. Tsien.

† Graduate Student.

The Shock Relations

To determine the shock relations consider an oblique attached shock at the nose of a wedge of half angle θ_s. α is the angle of the shock relative to the free-stream flow direction. p_s, the pressure immediately behind the shock, will also be the pressure on the surface of the wedge. The flow will be deflected through the angle θ_s by the shock.

By definition, the pressure coefficient is

$$C_p = \frac{p - p^0}{(1/2)\rho^0 U^2} = \frac{2}{\gamma}\frac{\gamma p^0}{\rho^0}\frac{1}{U^2}\left(\frac{p}{p^0} - 1\right) = \frac{2}{\gamma M^{0^2}}\left(\frac{p}{p^0} - 1\right) \quad (1)$$

Thus,

$$p_s/p^0 = (1/2)\gamma M^{0^2} C_{ps} + 1 \quad (2)$$

The thickness ratio of the wedge is θ_s. The flow parameter is then $K_s = M^0\theta_s$, and from the similarity law

$$C_{ps} = \theta_s^2 P_s(K_s) \quad (3)$$

so

$$p_s/p^0 = (1/2)\gamma K_s^2 P_s + 1 \quad (4)$$

The function P_s must now be determined. p_s/p^0 is given by the relations for oblique shock as[4]

$$\frac{p_s}{p^0} = \frac{2\gamma}{\gamma + 1} M^{0^2} \sin^2 \alpha - \frac{\gamma - 1}{\gamma + 1} \quad (5)$$

Substitution of Eq. (5) in Eq. (1) gives

$$C_{ps} = [4/(\gamma + 1)][\sin^2 \alpha - (1/M^{0^2})] \quad (6)$$

or

$$\sin^2 \alpha - (1/M^{0^2}) = [(\gamma + 1)/4]C_{ps} \quad (7)$$

In order to eliminate α, a relation between α and θ_s is needed. For this, consider[4]

$$\frac{1}{M^{0^2}} = \sin^2 \alpha - \frac{\gamma + 1}{2}\frac{\sin \alpha \sin \theta_s}{\cos(\alpha - \theta_s)} \quad (8)$$

which, in consideration of Eq. (7), becomes

$$\sin \alpha \sin \theta_s / \cos(\alpha - \theta_s) = (1/2)C_{ps} \quad (9)$$

Finally, by expanding the cosine term, Eq. (9) becomes

$$(1/4)C_{ps}^2 \cos^2 \alpha = [1 - (1/2)C_{ps}]^2 \sin^2 \alpha \tan^2 \theta_s \quad (10)$$

Eq. (10) is still general. It is now necessary to make the approximations appropriate for the conditions of hypersonic flows. For small values of θ_s—that is, for thin airfoils at small angles of attack—C_{ps} will be small. For the condition that M^0 is large, in conjunction with small θ_s, α will also be small. Therefore, the appropriate approximations are

$$\left.\begin{aligned}[1 - (1/2)C_{ps}]^2 &\simeq 1\\ \cos^2 \alpha &\simeq 1\\ \tan^2 \theta_s &\simeq \theta_s^2\end{aligned}\right\} \quad (11)$$

With these approximations and Eq. (7), Eq. (10) becomes

$$1/4\, C_{ps} = \theta_s^2 \sin^2 \alpha = \theta_s^2\left(\frac{\gamma + 1}{4} C_{ps} + \frac{1}{M^{0^2}}\right) \quad (12)$$

The substitution of $C_{ps} = \theta_s^2 P_s$ and $K_s = M^0\theta_s$ reduces Eq. (12) to

$$P_s^2 - (\gamma + 1)P_s - 4/K_s^2 = 0 \quad (13)$$

And, finally,

$$P_s = [(\gamma + 1)/2] + \sqrt{[(\gamma+1)/2]^2 + (4/K_s^2)} \quad (14)$$

the positive sign of the radical being required since P_s must be positive.

The value of C_{ps} when M^0 becomes infinite is needed in order to make a comparison with Sänger's results.

$$C_{ps} \to (\gamma + 1)\theta_s^2, \qquad \text{as } M^0 \to \infty \quad (15)$$

In a similar manner the equation for M_s, the Mach Number after the shock, is found to be

$$\frac{M_s}{M^0} = \left\{\frac{1}{[(\gamma + 1)/4]K_s^2 P_s + 1}\right\}^{1/2} \times \left\{\frac{[(\gamma + 1)/4]K_s^2 P_s + 1}{(\gamma/2)K_s^2 P_s + 1}\right\}^{1/2} \quad (16)$$

$K_s^2 P_s$ takes on all values from zero to infinity, so the second term of this expression varies from 1 down to $\sqrt{6/7} = 0.92$, for $\gamma = 1.4$. It could probably be neglected but will be included in all calculations here.

Also, by using Eq. (15),

$$M_s \to \frac{1}{\theta_s}\left[\frac{2}{\gamma}\left(\frac{1}{\gamma - 1}\right)\right]^{1/2}, \qquad \text{as } M^0 \to \infty \quad (17)$$

if $K_s^2 P_s = M^{0^2} C_{ps}$ is much greater than 1—that is, if θ_s is finite. For $\gamma = 1.4$, the square root in Eq. (17) is greater than 1; and since θ_s is small, $1/\theta_s$ is large. Thus, M_s is much greater than 1 in this limiting case. This condition will be used in making the approximations for the expansion relations that must now be determined.

The Expansion Relations

The pressure ratio for the expansion will be determined by consideration of expansion around a corner, which is known as Prandtl-Meyer flow. The relation between the initial Mach Number, M_s, the final Mach Number, M, and the angle of expansion, θ_e, in a Prandtl-Meyer expansion, is given by

$$\theta_e = \sqrt{\frac{\gamma+1}{\gamma-1}}\left(\tan^{-1}\sqrt{\frac{\gamma-1}{\gamma+1}}\sqrt{M^2-1} - \tan^{-1}\sqrt{\frac{\gamma-1}{\gamma+1}}\sqrt{M_s^2-1}\right) - \left(\tan^{-1}\sqrt{M^2-1} - \tan^{-1}\sqrt{M_s^2-1}\right) \quad (18)$$

For hypersonic conditions M_s is much greater than 1, as shown by Eq. (17), and M is greater than M_s. Therefore,

$$\sqrt{M^2-1} \simeq M, \qquad \sqrt{M_s^2-1} \simeq M_s \quad (19)$$

If, then, the arc tangents are expanded in infinite series, Eq. (18) becomes

$$\theta_e = \sqrt{\frac{\gamma+1}{\gamma-1}}\left[\frac{\pi}{2} - \frac{1}{M}\left(\frac{\gamma+1}{\gamma-1}\right)^{1/2} + \frac{1}{3M^3}\left(\frac{\gamma+1}{\gamma-1}\right)^{3/2} + \ldots - \frac{\pi}{2} + \frac{1}{M_s}\left(\frac{\gamma+1}{\gamma-1}\right)^{1/2} - \frac{1}{3M_s^3}\left(\frac{\gamma+1}{\gamma-1}\right)^{3/2} + \ldots\right] - \left(\frac{\pi}{2} - \frac{1}{M} + \frac{1}{3M^3} + \ldots - \frac{\pi}{2} + \frac{1}{M_s} - \frac{1}{3M_s^3} + \ldots\right)$$

$$\theta_e = \frac{2}{\gamma-1}\left(\frac{1}{M_s} - \frac{1}{M}\right) - \frac{1}{3}\left[\left(\frac{\gamma+1}{\gamma-1}\right)^2 - 1\right]\left(\frac{1}{M_s^3} - \frac{1}{M^3}\right) + \ldots \quad (20)$$

The relation between the pressure and Mach Number for an isentropic process such as the expansion is given by

$$\frac{p}{p_s} = \left\{\frac{[(\gamma-1)/2]M_s^2 + 1}{[(\gamma-1)/2]M^2 + 1}\right\}^{\gamma/(\gamma-1)} \simeq \left(\frac{M_s}{M}\right)^{2\gamma/(\gamma-1)} \quad (21)$$

or

$$M = M_s(p/p_s)^{-(\gamma-1)/2\gamma} \quad (22)$$

Substitution of Eq. (22) in Eq. (20) gives

$$\theta_e = \frac{2}{\gamma-1}\frac{1}{M_s}\left[1 - \left(\frac{p}{p_s}\right)^{(\gamma-1)/2\gamma}\right] - \frac{1}{3M_s^3}\left[\left(\frac{\gamma+1}{\gamma-1}\right)^2 - 1\right]\left[1 - \left(\frac{p}{p_s}\right)^{3(\gamma-1)/2\gamma}\right] + \ldots \quad (23)$$

In order to obtain a relation between p/p_s and $M_s\theta_e$, only the first term of this series can be retained. Then,

$$M_s\theta_e = [2/(\gamma-1)][1 - (p/p_s)^{(\gamma-1)/2\gamma}] \quad (24)$$

or

$$p/p_s = \{1 - [(\gamma-1)/2]M_s\theta_e\}^{2\gamma/(\gamma-1)} \quad (25)$$

If $K_e = M^0\theta_e$ is defined, Eq. (25) becomes

$$p/p_s = \{1 - [(\gamma-1)/2](M_s/M^0)K_e\}^{2\gamma/(\gamma-1)} \quad (26)$$

Eq. (26) determines the value of p/p_s for $[(\gamma-1)/2](M_s/M^0)K_e \leq 1$. For $[(\gamma-1)/2](M_s/M^0)K_e \geq 1$, p/p_s is zero. In the latter region the equation will give imaginary values for most values of γ and positive real values for those values of γ which make the exponent an even integer.

The physical reason for this behavior is that the pressure goes to zero for a finite deflection. If the surface of the body deflects more than this limiting value, the flow leaves the surface and the pressure remains zero. When a given deflection is required at a point on the airfoil, then as M^0 increases, it reaches a value at which the maximum physically possible deflection is required. The flow has expanded to an infinite Mach Number and to a zero pressure. This occurs when $[(\gamma-1)/2](M_s/M^0)K_e = 1$. For greater M^0, the pressure at the given point is still zero, but the flow has separated from the surface farther upstream.

By consideration of Eqs. (17) and (25), it is found that

$$\frac{p}{p_s} \to \left[1 - \left(\frac{\gamma-1}{2\gamma}\right)^{1/2}\frac{\theta_e}{\theta_s}\right]^{2\gamma/(\gamma-1)}, \quad \text{as} \quad M^0 \to \infty,\ \theta_s \neq 0 \quad (27)$$

The pressure coefficient can now be written in terms of K_s and K_e.

$$C_p = \frac{2}{\gamma M^{0^2}}\left(\frac{p}{p^0} - 1\right) = \frac{2}{\gamma M^{0^2}}\left(\frac{p}{p_s}\frac{p_s}{p^0} - 1\right) = \left(\theta_s^2 P_s + \frac{2}{\gamma M^{0^2}}\right)\left(1 - \frac{\gamma-1}{2}\frac{M_s}{M^0}K_e\right)^{2\gamma/(\gamma-1)} - \frac{2}{\gamma M^{0^2}} \quad (28)$$

For the case of no shock, θ_s is zero and M_s/M^0 is unity. For no expansion after shock, $C_p = \theta_s^2 P_s = C_{ps}$.

The Deflection Angles

Eq. (28) is not yet a function of K and ξ, so now the deflection angles must be determined from the boundary condition that the flow is tangent to the airfoil surface

at the surface, unless separation occurs by reason of the flow having expanded to a zero pressure.

The values of the deflection angles are then determined by the thickness distribution and angle of attack of the airfoil. The profile of the airfoil is given in x, y axes, with the chord on the x-axis and the midpoint of the chord at the origin. The leading edge is at $-b$, and the trailing edge is at b; the chord is $2b$. The profile must be slender and pointed, as for linearized theory, since the deflection angles have been considered to be small. The x-axis is taken as inclined to the direction of the undisturbed flow at the angle of attack α.

For values of the angle of attack less than the slope of the upper surface at the leading edge, shock will occur on the upper surface; for greater angles of attack, no shock will occur on the upper surface, so the angle of shock deflection will be zero. Thus, the deflection angles must be evaluated in the two regions separately for the upper surface.

For the purpose of writing out the deflection angles, the following notation is convenient: $f(x) = dy/dx =$ slope of the profile; subscript u indicates the upper surface; subscript l indicates the lower surface; subscript $-b$ indicates the leading edge value; and $f_u = f_l$ for symmetrical profiles. Then,

$$\begin{array}{lll} 0 \le \alpha \le f_{-b,u} & \theta_{s,u} = f_{-b,u} - \alpha & \theta_{e,u} = f_{-b,u} - f_u(x) \\ \alpha \ge f_{-b,u} & \theta_{s,u} = 0 & \theta_{e,u} = \alpha - f_u(x) \\ \text{all } \alpha & \theta_{s,l} = f_{-b,l} + \alpha & \theta_{e,l} = f_{-b,l} - f_l(x) \end{array} \tag{29}$$

For the transformation used in the hypersonic similarity law, with $d\eta/d\xi = h(\xi)$, and if $\alpha = \delta\sigma$, where σ is the transformed angle of attack, the deflection angles become

$$\begin{array}{lll} 0 \le \sigma \le h_{-1,u} & \theta_{s,u} = \delta(h_{-1,u} - \sigma) & \theta_{e,u} = \delta[h_{-1,u} - h_u(\xi)] \\ \sigma \ge h_{-1,u} & \theta_{s,u} = 0 & \theta_{e,u} = \delta[\sigma - h_u(\xi)] \\ \text{all } \sigma & \theta_{s,l} = \delta(h_{-1,l} + \sigma) & \theta_{e,l} = \delta[h_{-1,l} - h_l(\xi)] \end{array}$$

If, finally, $\beta(\xi)$ is defined by

$$M^0\theta = M^0\delta\beta = K\beta$$

where the β's are determined by Eqs. (30), then the $M^0\theta$ parameters have been found in terms of K and ξ.

The pressure coefficient can now be written in terms of K, ξ, and σ.

$$C_p/2\delta^2 = [(1/2)\beta_s^2 P_s + (1/\gamma K^2)]\left\{1 - [(\gamma - 1)/2](M_s/M^0)K\beta_e\right\}^{2\gamma/(\gamma-1)} - (1/\gamma K^2) \tag{31}$$

For a given thickness distribution, β_s depends only on the angle of attack. β_e varies with ξ, however. The evaluation of the force and moment coefficients will be simplified by the following notation, which separates those terms of the pressure coefficient which are not functions of ξ from those that are functions of ξ.

$$\left.\begin{array}{l} C_p/2\delta^2 = AB(\xi) - (1/\gamma K^2) \\ A = [(\gamma+1)/4]\beta_s^2 + \sqrt{\left\{[(\gamma+1)/4]\beta_s^2\right\}^2 + (\beta_s^2/K^2)} + (1/\gamma K^2) \\ B = \left\{1 - [(\gamma-1)/2](M_s/M^0)K\beta_e\right\}^{2\gamma/(\gamma-1)} \\ \dfrac{M_s}{M^0} = \left(\dfrac{\gamma-1}{2}K^2A + \dfrac{\gamma+1}{2}\right)^{-1/2}\left(\dfrac{\gamma-1}{2\gamma^2}\dfrac{1}{K^2A} + \dfrac{\gamma+1}{2\gamma}\right)^{1/2} \end{array}\right\} \tag{32}$$

$$\begin{array}{lll} 0 \le \sigma \le h_{-1,u} & \beta_{s\,u,} = h_{-1,u} - \sigma & \beta_{e,u} = h_{-1,u} - h_u(\xi) \\ \sigma \ge h_{-1,u} & \beta_{s\,u,} = 0 & \beta_{e,u} = \sigma - h_u(\xi) \\ \text{all } \sigma & \beta_{s\,l,} = h_{-1,l} + \sigma & \beta_{e,l} = h_{-1,l} - h_l(\xi) \end{array}$$

When using Eqs. (32) to evaluate the pressure coefficient on, say, the upper surface of the profile, the subscript u must be added to all terms depending on β's. When writing out the full term, the correct β's should be used.

Force and Moment Coefficients

Now that the pressure coefficient has been determined, it can be used to evaluate the lift, drag, and moment coefficients. The forms

$$\left.\begin{array}{l} C_l = (1/2b)\displaystyle\int_{-b}^{b}\left((-C_{p,u} + C_{p,l})dx = \int_{-1}^{1}\left(-\frac{1}{2}C_{p,u} + \frac{1}{2}C_{p,l}\right)d\xi\right. \\ C_d = (1/2b)\displaystyle\int_{-b}^{b}[-C_{p,u}(\alpha - f_u) + C_{p,l}(\alpha + f_l)]dx = \delta\int_{-1}^{1}\left[\sigma\left(-\frac{1}{2}C_{p,u} + \frac{1}{2}C_{p,l}\right) + \frac{1}{2}h_uC_{p,u} + -h_lC_{p,l}\right. \\ C_{m(c/2)} = \dfrac{-1}{(2b)^2}\displaystyle\int_{-b}^{b}(-C_{p,u} + C_{p,l})x dx = -\frac{1}{2}\int_{-1}^{1}\left(-\frac{1}{2}C_{p,u} + \frac{1}{2}C_{p,l}\right)\xi d\xi \end{array}\right\} \tag{33}$$

TABLE 1

Coefficients for Two-Dimensional Hypersonic Flows

$$\frac{C_l}{\delta^2} = -A_u \mathrm{I}_u + A_l \mathrm{I}_l \qquad \frac{C_d}{\delta^2} = \sigma \frac{C_l}{\delta^2} + A_u \mathrm{II}_u + A_l \mathrm{II}_l \qquad \frac{C_{m(c/2)}}{\delta^2} = A_u \mathrm{III}_u - A_l \mathrm{III}_l$$

$$A = \frac{\gamma+1}{4}\beta_s^2 + \sqrt{\left(\frac{\gamma+1}{4}\beta_s^2\right)^2 + \frac{\beta_s^2}{K^2} + \frac{1}{\gamma K^2}} \qquad K = M^0\delta,\ \sigma = \alpha/\delta$$

M^0 = free-stream Mach Number

δ = thickness ratio

α = angle of attack

$$\mathrm{I} = \int_{-1}^{1} \left[1 - \frac{\gamma-1}{2}\frac{M_s}{M^0} K\beta_s(\xi)\right]^{2\gamma/(\gamma-1)} d\xi$$

$$\mathrm{II} = \int_{-1}^{1} h(\xi)\left[1 - \frac{\gamma-1}{2}\frac{M_s}{M^0} K\beta_s(\xi)\right]^{2\gamma/(\gamma-1)} d\xi$$

Sub u or l, upper or lower surface. The same subscript appears on terms as on β's therein. Sub -1, value at leading edge.

$$\mathrm{III} = \frac{1}{2}\int_{-1}^{1} \xi\left[1 - \frac{\gamma-1}{2}\frac{M_s}{M^0} K\beta_s(\xi)\right]^{2\gamma/(\gamma-1)} d\xi$$

$$\frac{M_s}{M^0} = \left(\frac{\gamma-1}{2}K^2A + \frac{\gamma+1}{2}\right)^{-1/2}\left(\frac{\gamma-1}{2\gamma^2}\frac{1}{K^2A} + \frac{\gamma+1}{2\gamma}\right)^{1/2}, \text{ second term may be neglected.}$$

$0 \leqq \sigma \leqq h_{-1,u}$	$\beta_{s,u} = h_{-1,u} - \sigma$	$\beta_{s,u} = h_{-1,u} - h_u(\xi)$
$\sigma \geqq h_{-1,u}$	$\beta_{s,u} = 0$	$\beta_{s,u} = \sigma - h_u(\xi)$
all σ	$\beta_{s,l} = h_{-1,l} + \sigma$	$\beta_{s,l} = h_{-1,l} - h_l(\xi)$

$h(\xi) = (1/\delta)(dy/dx)(\xi)$, where $(dy/dx)(x)$ is for the surface of a slender pointed airfoil whose leading edge is at $x = -b$, with a chord $2b$ on the x-axis, which is inclined at the angle of attack α to the flow. For symmetry, $h_u = h_l$.

When

$$[(\gamma-1)/2](M_s/M^0)K\beta_s(\xi) \geq 1$$

the terms containing it are zero.

For K greater than 10 the following approximations can be made.

$$A = \frac{\gamma+1}{2}\beta_s^2; \qquad \frac{\gamma-1}{2}\left(\frac{M_s}{M^0}\right)K = \left(\frac{\gamma-1}{2\gamma}\right)^{1/2}\frac{1}{\beta_s}, \qquad \beta_s \neq 0$$

Region of validity of equations: $M^0 \geq 5$, K order of 1.

will be considered sufficiently accurate for the thin profiles and small angles of attack under consideration. Positive moments are taken as tending to raise the leading edge. By substitution of the pressure coefficient from Eqs. (32), the coefficients become

$$\left.\begin{aligned}
C_l/\delta^2 &= -A_u\int_{-1}^{1} B_u d\xi + A_l\int_{-1}^{1} B_l d\xi = -A_u \mathrm{I}_u + A_l \mathrm{I}_l \\
\frac{C_d}{\delta^2} &= \sigma\frac{C_l}{\delta^2} + A_u\int_{-1}^{1} h_u B_u d\xi + A_l\int_{-1}^{1} h_l B_l d\xi - \frac{1}{\gamma K^2}\int_{-1}^{1}(h_u + h_l)d\xi = \sigma\frac{C_l}{\delta^2} + A_u\int_{-1}^{1} h_u B_u d\xi + \\
&\qquad A_l\int_{-1}^{1} h_l B_l d\xi = \sigma\frac{C_l}{\delta^2} + A_u \mathrm{II}_u + A_l \mathrm{II}_l \\
C_{m(c/2)}/\sigma^2 &= A_u\int_{-1}^{1}(1/2)\xi B_u d\xi - A_l\int_{-1}^{1}(1/2)\xi B_l d\xi = A_u \mathrm{III}_u - A_l \mathrm{III}_l
\end{aligned}\right\} \quad (34)$$

The last term in the drag expression drops out, since

$$\int_{-1}^{1} h\, d\xi = \int_{-1}^{1}(d\eta/d\xi)d\xi = \int_{-1}^{1} d\eta = 0 \qquad (35)$$

by definition of the x-axis. The terms I, II, and III are defined by Eqs. (34).

The combination of Eqs. (32) and (34) provides a method for the determination of the force and moment coefficients of two-dimensional airfoils in hypersonic flows. This method is summarized in Table 1.

The physical significance of the various terms in Table 1, especially I, II, III, becomes clearer when it is noted that A is equal to $(1/\gamma K^2)(p_s/p^0)$ and therefore represents the pressure ratio due to the shock at the leading edge. Similarly, the term B of Eq. (32) is equal to p/p_s and thus represents the expansion pressure ratio at any point on the chord. Thus, I, the integral sum of the product of the expansion pressure ratio and the element of the nondimensional chord, $d\xi$, over which it acts, is a contribution to the lift force. When this product is multiplied by the local nondimensional inclination of the airfoil surface to its chord, $h(\xi)$, a contribution to the drag is obtained (term II), or if it is multiplied by the local coordinates, ξ, a moment contribution results (term III).

The β terms clearly represent the variation of the nondimensional inclination of the surface of the airfoil to the free stream.

The Flat Plate

The method of determining the lift, drag, and moment coefficients of two-dimensional airfoils in hypersonic flows, which is summarized in Table 1, can be applied to a flat plate as a simple illustration. For this case δ cancels out, leaving the new parameter $M^0\alpha$, which will be defined as K_0.

For a flat plate $h_u = h_l = 0$. Then, for all σ—that is, for all α—Table 1 gives the following results.

$\beta_{s,u}$	$= 0$	$\beta_{s,l}$	$= \sigma$
$\beta_{e,u}$	$= \sigma$	$\beta_{e,l}$	$= 0$
$(M_s/M^0)_u$	$= 1$	$(M_s/M^0)_l$	= not needed
I_u	$= 2\{1 - [(\gamma - 1)/2]K\sigma\}^{2\gamma/(\gamma-1)}$	I_l	$= 2$
II_u	$= 0$	II_l	$= 0$
III_u	$= 0$	III_l	$= 0$
A_u	$= 1/\gamma K^2$	A_l	$= \sigma^2\left[\frac{\gamma+1}{4} + \sqrt{\left(\frac{\gamma+1}{4}\right)^2 + \frac{1}{K^2\sigma^2}}\right] + \frac{1}{\gamma K^2}$

Since $\alpha = \delta\sigma$ and $K = M^0\delta$, then $K\sigma = K_0$, so the coefficients are

$$C_l = \alpha^2\left[\frac{\gamma+1}{2} + \sqrt{\left(\frac{\gamma+1}{2}\right)^2 + \frac{4}{K_0^2}}\right] + \frac{2}{\gamma M^{0^2}}\left[1 - \left(1 - \frac{\gamma-1}{2}K_0\right)^{2\gamma/(\gamma-1)}\right]$$

$$C_d = \alpha C_l$$

$$C_{m(c/2)} = 0$$

When $(1/2)(\gamma + 1)K_0 \geq 1$, the second term of the lift coefficient becomes merely $2/\gamma M^{0^2}$. C_l/α^2 can be written as a function of K_0 only.

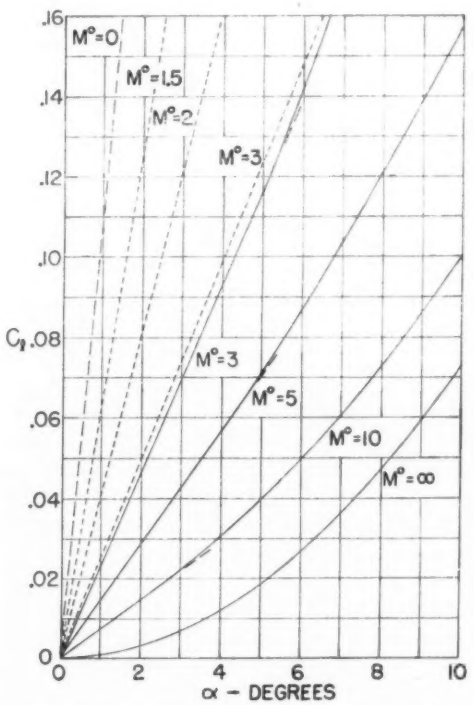

FIG. 1. Lift coefficient C_l of a flat plate vs. angle of attack α at various Mach Numbers M^0. Solid curves—hypersonic theory; dashed curves—Ackeret theory.

$$\frac{C_l}{\alpha^2} = \frac{\gamma+1}{2} + \sqrt{\left(\frac{\gamma+1}{2}\right)^2 + \frac{4}{K_0^2}} + \frac{2}{\gamma K_0^2}\left[1 - \left(1 - \frac{\gamma-1}{2}K_0\right)^{2\gamma/(\gamma-1)}\right]$$

C_l and C_l/α^2 and their derivatives are continuous at $(1/2)(\gamma + 1)K_0 = 1$.

These equations confirm the statement that for large values of M^0 the lift is approximately proportional to the square of the angle of attack. But they also provide a quantitative evaluation of the degree of validity of this statement. It is not strictly true until M^0 is infinite, when

$$C_l = (\gamma + 1)\alpha^2$$

For finite values of M^0, the lift curve starts from the origin as a straight line, which rapidly becomes parabolic as the quadratic term becomes important. The point of transition from a linear relation approaches the origin as M^0 approaches infinity.

The values of the lift coefficient given by this hypersonic equation, with $\gamma = 1.4$, are shown in Fig. 1 for $M^0 = 3$, 5, 10, and ∞. The decreasing linear range as M^0 increases is indicated, but the most conspicuous feature is the extremely small lift coefficients available in the hypersonic region. The curves for $M^0 = 0$, with the incompressible fluid theory slope of 2π per radian, and for $M^0 = 1.5$, 2, and 3, with the linearized supersonic theory slope of $4/\sqrt{M^{0^2} - 1}$, are also shown in Fig. 1 for comparison. The family of curves emphasizes the rapid decrease of the lift coefficient as the free-stream Mach Number increases. For large angles of attack in the hypersonic region, the linear theory underestimates the lift and therefore is not satisfactory.

Airfoils with Thickness

The hypersonic force and moment coefficients have been calculated, by use of the equations of Table 1, for three simple airfoils with thickness. The three airfoils are:

TABLE 2
Equations: Airfoils with Thickness

$$\frac{C_l}{\delta^2} = -A_u \mathrm{I}_u + A_l \mathrm{I}_l \qquad \frac{C_d}{\delta^3} = \sigma \frac{C_l}{\delta^2} + A_u \mathrm{II}_u + A_l \mathrm{II}_l \qquad \frac{C_{m(c/2)}}{\delta^2} = A_u \mathrm{III}_u - A_l \mathrm{III}_l$$

Double Wedge

$$-1 \le \xi \le 0,\ h_u = 1,\ h_l = 1;\quad 0 \le \xi \le 1,\ h_u = -1,\ h_l = -1;\quad \beta_{s,u} = 1 - \sigma,\ \beta_{s,l} = 1 + \sigma$$

$\sigma \le 1$

$$A_u \mathrm{I}_u = A_u + A_u\left[1 - (\gamma - 1)\left(\frac{M_s}{M^0}\right)_u K\right]^{2\gamma/(\gamma-1)}$$

$$A_u \mathrm{II}_u = A_u - A_u\left[1 - (\gamma - 1)\left(\frac{M_s}{M^0}\right)_u K\right]^{2\gamma/(\gamma-1)}$$

$$A_u \mathrm{III}_u = -(1/4) A_u \mathrm{II}_u$$

Lower surface equations of same form

$\sigma \ge 1$

$$A_u \mathrm{I}_u = \frac{1}{\gamma K^2}\left[1 - \frac{\gamma-1}{2} K(\sigma - 1)\right]^{2\gamma/(\gamma-1)} + \frac{1}{\gamma K^2}\left[1 - \frac{\gamma-1}{2} K(\sigma + 1)\right]^{2\gamma/(\gamma-1)}$$

$$A_u \mathrm{II}_u = \frac{1}{\gamma K^2}\left[1 - \frac{\gamma-1}{2} K(\sigma - 1)\right]^{2\gamma/(\gamma-1)} - \frac{1}{\gamma K^2}\left[1 - \frac{\gamma-1}{2} K(\sigma + 1)\right]^{2\gamma/(\gamma-1)}$$

$$A_u \mathrm{III}_u = -(1/4) A_u \mathrm{II}_u$$

Lower surface as for $\sigma \le 1$

Single Wedge

$$-1 \le \xi \le 0,\ h_u = 2,\ h_l = 0;\quad 0 \le \xi \le 1,\ h_u = -2,\ h_l = 0;\quad \beta_{s,u} = 2 - \sigma,\ \beta_{s,l} = \sigma$$

$\sigma \le 2$

$$A_u \mathrm{I}_u = A_u + A_u\left[1 - 2(\gamma - 1)\left(\frac{M_s}{M^0}\right)_u K\right]^{2\gamma/(\gamma-1)}$$

$$A_u \mathrm{II}_u = 2A_u - 2A_u\left[1 - 2(\gamma - 1)\left(\frac{M_s}{M^0}\right)_u K\right]^{2\gamma/(\gamma-1)}$$

$$A_u \mathrm{III}_u = -(1/8) A_u \mathrm{II}_u$$

$$A_l \mathrm{I}_l = 2A_l,\ A_l \mathrm{II}_l = A_l \mathrm{III}_l = 0, \text{ for all } \sigma$$

$\sigma \ge 2$

$$A_u \mathrm{I}_u = \frac{1}{\gamma K^2}\left[1 - \frac{\gamma-1}{2} K(\sigma - 2)\right]^{2\gamma/(\gamma-1)} + \frac{1}{\gamma K^2}\left[1 - \frac{\gamma-1}{2} K(\sigma + 2)\right]^{2\gamma/(\gamma-1)}$$

$$A_u \mathrm{II}_u = 2\frac{1}{\gamma K^2}\left[1 - \frac{\gamma-1}{2} K(\sigma - 2)\right]^{2\gamma/(\gamma-1)} - \frac{2}{\gamma K^2}\left[1 - \frac{\gamma-1}{2} K(\sigma + 2)\right]^{2\gamma/(\gamma-1)}$$

$$A_u \mathrm{III}_u = -(1/8) A_u \mathrm{II}_u$$

Single Parabolic

$$h_u = -4\xi,\ h_l = 0;\quad \beta_{s,u} = 4 - \sigma,\ \beta_{s,l} = \sigma$$

$\sigma \le 4$

$$A_u \mathrm{II}_{uu} = -\frac{1}{4}\left[\frac{2}{3\gamma - 1}\frac{A_u}{K}\left(\frac{M^0}{M_s}\right)_u\right]\left\{\left[1 - 4(\gamma - 1)\left(\frac{M_s}{M^0}\right)_u K\right]^{(3\gamma-1)/(\gamma-1)} - 1\right\}$$

$$A_u \mathrm{II}_u = \left[\frac{2}{3\gamma - 1}\frac{A_u}{K}\left(\frac{M^0}{M_s}\right)_u\right]\left\{\left[1 - 4(\gamma - 1)\left(\frac{M_s}{M^0}\right)_u K\right]^{(3\gamma-1)/(\gamma-1)} + 1\right\} + \frac{1}{2}\left[\frac{1}{3\gamma - 1}\frac{1}{2\gamma - 1}\frac{A_u}{K^2}\left(\frac{M^0}{M_s}\right)_u^2\right]\left\{\left[1 - 4(\gamma - 1)\left(\frac{M_s}{M^0}\right)_u K\right]^{(4\gamma-2)/(\gamma-1)} - 1\right\}$$

$\sigma \ge 4$

$$A_u \mathrm{I}_u = -\frac{1}{4}\left(\frac{2}{3\gamma - 1}\frac{1}{\gamma K^3}\right)\left\{\left[1 - \frac{\gamma-1}{2} K(\sigma + 4)\right]^{(3\gamma-1)/(\gamma-1)} - \left[1 - \frac{\gamma-1}{2} K(\sigma - 4)\right]^{(3\gamma-1)/(\gamma-1)}\right\}$$

$$A_u \mathrm{II}_u = \left(\frac{2}{3\gamma - 1}\frac{1}{\gamma K^3}\right)\left\{\left[1 - \frac{\gamma-1}{2} K(\sigma + 4)\right]^{(3\gamma-1)/(\gamma-1)} + \left[1 - \frac{\gamma-1}{2} K(\sigma - 4)\right]^{(3\gamma-1)/(\gamma-1)}\right\} + \frac{1}{2}\left(\frac{1}{3\gamma - 1}\frac{1}{2\gamma - 1}\frac{1}{\gamma K^4}\right)\left\{\left[1 - \frac{\gamma-1}{2} K(\sigma + 4)\right]^{(4\gamma-2)/(\gamma-1)} - \left[1 - \frac{\gamma-1}{2} K(\sigma - 4)\right]^{(4\gamma-2)/(\gamma-1)}\right\}$$

All σ: $A_u \mathrm{III}_u = -(1/8) A_u \mathrm{II}_u$ $\quad A_l \mathrm{I}_l = 2A_l$ $\quad A_l \mathrm{II}_l = A_l \mathrm{III}_l = 0$

(1) A chordwise symmetrical, symmetrical double wedge, which will be called a double wedge.

(2) A chordwise symmetrical single wedge whose lower surface is flat. It will be called a single wedge.

(3) A chordwise symmetrical single parabolic profile whose lower surface is flat. It will be termed a single parabolic profile.

The slope of the upper surface of the profile at the leading edge divides the angle of attack into two regions. For angles of attack less than this value, shock will occur on the upper surface of the profile, with a consequent loss of lift. Therefore it is desirable to operate at angles of attack greater than this value. For this reason the angle of attack equal to the slope of the upper surface at the leading edge will be called the critical angle of attack. For the three profiles considered here, the critical angles of attack are δ, 2δ, and 4δ, respectively. Thus the critical values of the transformed angle of attack, σ, are 1, 2, and 4.

For an airfoil at an angle of attack above the critical, the contribution of the upper surface is increasingly negligible as M^0 increases. And, since most of the lift is furnished by the lower surface, any expansion on the lower surface is detrimental. Thus, the best profile in the hypersonic region will have a flat lower surface.

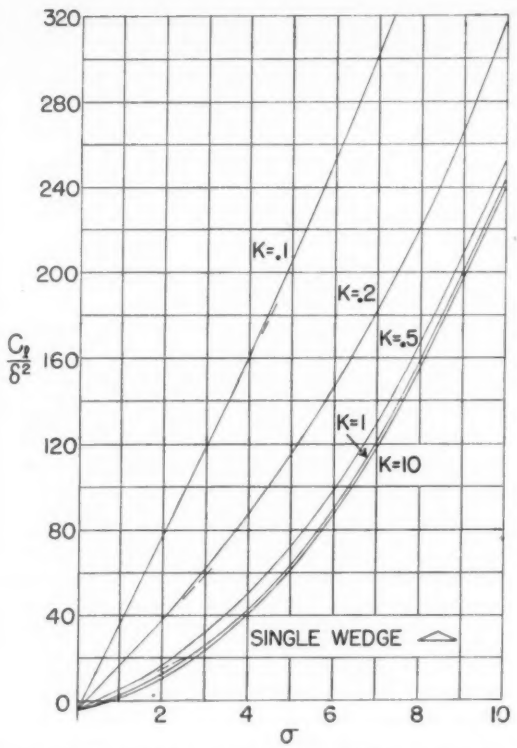

FIG. 2. C_l/δ^2 of a single wedge airfoil vs. σ for various values of K. δ, thickness ratio; $\sigma = \alpha/\delta$; $K = M\delta$.

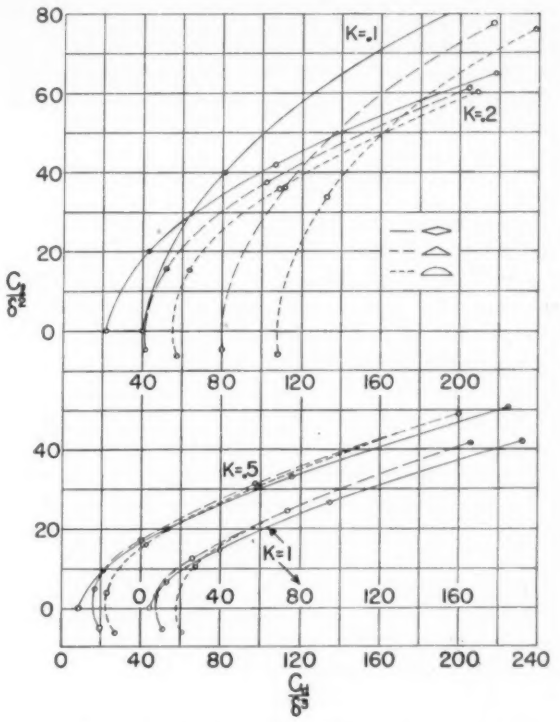

FIG. 4. Polars for double wedge, single wedge, and circular arc airfoils. Large scale.

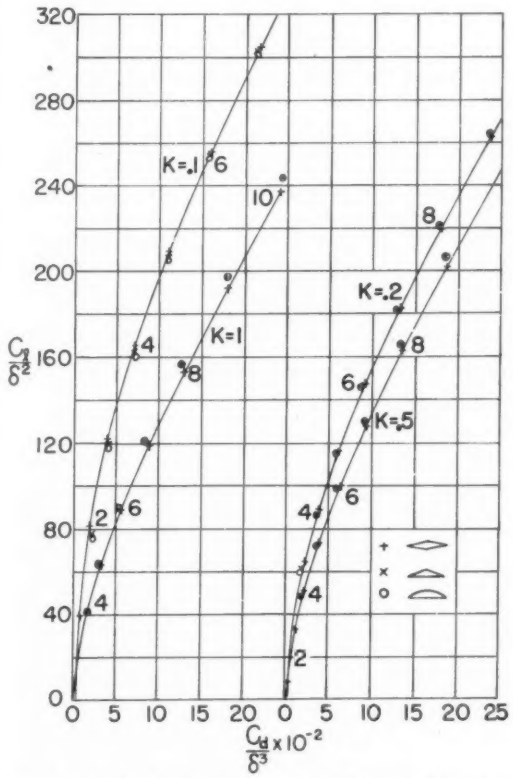

FIG. 3. Polars for double wedge, single wedge, and circular arc airfoils. C_d, drag coefficient.

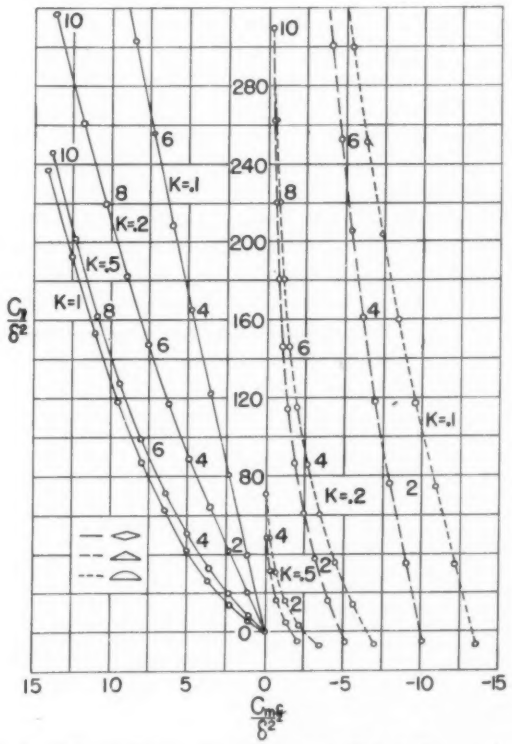

FIG. 5. Lift coefficient vs. moment coefficient $C_{m(c/2)}$ about half-chord point.

The equations obtained by use of the relations of Table 1, and used to plot Figs. 2–5, are shown in Table 2. The values of A and M_s/M^0, which are functions of β_s, are to be determined by the equations given for them in Table 1.

Discussion of Results

The results of the calculation of the hypersonic coefficients for the three airfoils with thickness are shown in Figs. 2–5. Fig. 2 shows the lift curve of the single wedge profile; Figs. 3 and 4 present the polars for all three profiles, in two different scales; and Fig. 5 shows the moment curves for all three profiles.

Fig. 2, the lift curve of the single wedge, is similar to the lift curve of the flat plate, Fig. 1. The effect of the thickness ratio on the characteristics of hypersonic airfoils can be found from any of the families of curves. Since K is directly proportional to both δ and M^0, a change in δ will have the same effect as a change of M^0 in the same ratio, and vice versa.

In Fig. 3 the curve for the double wedge is drawn, with only the points for the other two profiles shown in the interests of clarity. The curves for $K = 1$, 10, and ∞ fall almost on each other. The single parabolic profile never has a $\delta L/D$ ratio better than the single wedge, but for low values of lift the single wedge is superior. A comparison between the single and double wedge shows that the single wedge is again superior, except for low values of lift. The transition value of the lift increases as K decreases. The single wedge is superior in this comparison. The increasing superiority of the flat bottom profiles as K increases is also indicated by Fig. 3.

Fig. 4 shows the polars to a larger scale so that the maximum $\delta L/D$ can be investigated. In hypersonic flows the wave drag is small, so the skin friction will be an important part of the total drag. The maximum $\delta L/D$ indicated by Fig. 4 may be appreciably reduced by the skin friction. When friction is not considered, the single wedge has the greatest maximum $\delta L/D$ for $K \geq 0.5$. When friction is considered, the minimum value of K for which this is true will decrease. Simultaneously, the maximum $\delta L/D$ will decrease, and the lift coefficient at maximum $\delta L/D$ will increase.

Fig. 5 shows that the moment for the double wedge in the hypersonic region is positive and increases as K increases. As K increases, the center of pressure thus moves forward at a constant lift coefficient. It does not reach the quarter-chord point. The moment coefficients of the single wedge and the single parabolic profiles are negative about the mid-chord. As K increases, they increase algebraically, as for the double wedge, but these profiles approach zero as a limit (above the critical angle of attack).

On the basis of a smaller (negative) moment the single wedge profile is superior to the parabolic profile at all lift coefficients. This is a result of the smaller leading edge slope of the upper surface, for equal thickness ratios, of the single wedge profile. This difference between the two profiles also accounts for the difference in $\delta L/D$'s noted in connection with Fig. 3. A criterion for chordwise symmetric profiles for hypersonic flows can thus be made. For chordwise symmetric profiles the slope of the upper surface at the leading edge should be a minimum. The profile that meets this condition is the wedge upper surface.

The above results, for an infinite M^0, have been compared with Sänger's results, and the agreement is satisfactory.

References

[1] von Kármán, Th., *The Problem of Resistance in Compressible Fluids*, Proceedings of the 5th Volta Congress, Rome, pp. 275–277, 1936.

[2] Sänger, E., *R-Antriebe*, Der Deutschen Akademie Der Luftfahrtforschung, Berlin, pp. 189–194, 1943.

[3] Tsien, H. S., *Similarity Laws of Hypersonic Flows*, Journal of Mathematics and Physics, Vol. XXV, No. 3, pp. 247, October, 1946.

[4] Liepmann, H., and Puckett, A., *An Introduction to Aerodynamics of a Compressible Fluid*, pp. 57 and 58; John Wiley and Sons, Inc., New York, 1947.

Linearized Theory of Supersonic Control Surfaces

P. A. LAGERSTROM* AND MARTHA E. GRAHAM*

California Institute of Technology

SUMMARY

The purpose of the present paper is to make some contributions to the aerodynamic theory of control surfaces in supersonic flight. The control surfaces discussed have trapezoidal or triangular plan forms and are attached to an immovable surface ("wing") so that a mutual interference exists between the stationary surface and the deflected control surface. The linearized theory is used exclusively. The basic property computed is the pressure distribution induced by the deflection of the control surface; from this pressure distribution, lift, and center of pressure are found. It will be seen that, in general, only a comparatively small part of the wing is influenced by the deflection of the control surface, so that most of the aerodynamic load will be carried by the control surface itself. However, in the cases considered in this report, the interference is favorable—i.e., the total lift on the wing and on the control surface induced by a deflection is greater than the total lift obtained by the same deflection of an isolated control surface. This depends mainly on the fact that the mutual dependence of the upper and lower surfaces near a subsonic edge (which causes loss of lift as compared to the two-dimensional value) is prevented by the presence of a wing. For real fluids there might be some communication between upper and lower surfaces, because of leakage through the "gap" between wing and deflected surface. This leakage, which is not taken into account in the linearized theory, could cause loss of lift. There are many similar phenomena that tend to reduce lift which may not be treated in the linearized theory and which are intimately connected with the viscous properties of the fluid. Thus, in general, while linearized theory gives a fair prediction of lift and wave drag of a wing, it is expected to give values that are too high when applied to control surfaces. Correction factors will have to be found from experiments; from the suspected importance of viscous effects, it seems advisable to pay much attention to the Reynolds Number in such experiments.

The present paper is an abbreviated version of reference 1, which contains detailed explanations, computations, and also some discussion of the applicability of the theory to real fluids. The basic formulas for pressure distribution are taken from the theory of conical flow and may be found in references 2 and 3.

NOTATION

C_L = lift coefficient resulting from aileron deflection based on aileron area

$C_{L_{2\text{-dim.}}}$ = two-dimensional lift coefficient $= 4\delta m$

C_p = pressure coefficient

$C_{p_{2\text{-dim.}}}$ = two-dimensional pressure coefficient $= 2\delta m$

A. R. = aspect ratio of aileron

a = $m \tan \varphi$ (denotes position of leading edge of aileron)

b = $\tan \beta / \tan \mu$ (denotes position of outboard edge of aileron)

c = $\tan \gamma / \tan \mu$ (denotes position of inboard edge of aileron)

d = chord of aileron

M = free-stream Mach Number

m = $1/\sqrt{M^2 - 1} = \tan \mu$

q = $\frac{1}{2}\rho U^2$

t = $\tan \tau / \tan \mu$

$l_{C.P.}$ = ray on which center of pressure is located

U = free-stream velocity

α = angle of attack

β = angle denoting position of outboard ("free") edge of aileron

γ = angle denoting position of inboard edge of aileron

δ = angle of deflection of control surface with reference to wing

μ = Mach angle

ρ = density

τ = angle denoting arbitrary position on aileron or adjacent wing

φ = angle of sweepback of leading edge of aileron

Presented at the Aerodynamics Session, Sixteenth Annual Meeting, I.A.S., New York, January 26–29, 1948.

* Guggenheim Aeronautical Laboratory.

RECTANGULAR PLAN FORM

THIS ELEMENTARY EXAMPLE is well adapted to illustrate the fundamental principles. Consider a rectangular wing ABCD (Fig. 1) with a rectangular aileron AIEF deflected so that the increase in angle of attack as compared with zero deflection is δ.

It follows from the superposition principle[4] that the effect of deflecting the wing is obtained by superimposing the solution for (b) in Fig. 1 on the solution for the wing with undeflected aileron. The solution for (b) is the same as that for a rectangular wing of plan form AIEF except in the Mach cone from E. This is exactly the region where the interference between the wing and the aileron takes place. The presence of the flat plate at zero angle of attack to the left of EF corresponds to the presence of the wing. It means that the deflected surface may induce no downwash on EFG but that, on the other hand, a pressure differential can be carried here by the plate. Since $\alpha = 0$, this pressure differ-

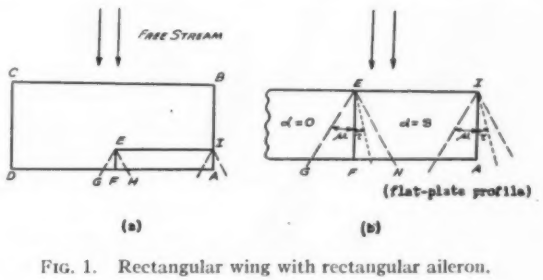

FIG. 1. Rectangular wing with rectangular aileron.

ential is zero outside the Mach cone from E. Without knowledge of the actual pressure distribution, one may conclude immediately that the lift coefficient in EGH based on the area of the deflected part (EFH) has the two-dimensional value $4\delta m$. This is so, for, if a new wing is formed by interchanging right and left in Fig. 1b and the two wings are superimposed, the pressure distribution in the Mach cone from E will be two-dimensional.

Actually, the pressure distribution may be found from a well-known solution by the following procedure. To fix the ideas, assume $\delta > 0$. Consider a nonlifting wing of plan form AIEF with a wedge profile of half angle δ. It is well known that the pressure in the Mach cone is given by the formula

$$C_p/C_{p_{2\text{-dim.}}} = (1/\pi) \arccos(-t) \qquad (1)$$

Since this nonlifting wing does not induce any downwash in the plane of the wing, a flat plate at zero angle of attack may be inserted there without changing the flow characteristics. Assume that this flat plate covers at least EFG. Then communication between the upper and lower surfaces is excluded in the triangle EGH. Consequently, if the lower surface is kept intact and the upper surface changed so that the wing has zero thickness, Eq. (1) is still valid for the lower surface. But the wing so obtained is exactly the wing in Fig. 1b. Thus, conditions on the lower surface are known. For zero thickness the perturbation pressure is antisymmetric in the plane of the wing—i.e., on the upper surface it has the same absolute value but opposite sign as compared with corresponding points on the lower surface. Since C_p is referred to $C_{p_{2\text{-dim.}}}$, Eq. (1) is valid for both upper and lower surfaces in region EGH of Fig. 1b. Summarizing these results for the pressure distribution on the lifting surface in Fig. 1b gives the following formulas.

In the deflected part outside the Mach cones from E and I:

$$C_p/C_{p_{2\text{-dim.}}} = 1 \qquad (2a)$$

In the Mach cone from I

$$C_p/C_{p_{2\text{-dim.}}} = (1/\pi) \arccos(1 + 2t) \qquad (2b)$$

In the Mach cone from E

$$C_p/C_{p_{2\text{-dim.}}} = (1/\pi) \arccos(-t) \qquad (2c)$$

By integrating Eq. (2c) it is found that the loss in lift (as compared to the two-dimensional value) in the region EFH is given by

$$\text{Loss in lift in EFH} = 2q\delta m^2 d^2/\pi \qquad (3)$$

This is compensated for by an induced lift in EFG of exactly the same amount.

It should be noted that the plan form of the wing is entirely irrelevant except as it affects the area of the portion of the wing inside the Mach cone from E. Thus, a change in chord length of the wing or in the sweepback of the leading edge has no effect on the lift of the control surface according to the linearized theory. For a real fluid, however, the chord length will influence the thickness of the boundary layer and thus, presumably, also the effectiveness of the aileron.

Also note that Eq. (2c) predicts no pressure equalization due to leakage through the gap EF. How much leakage there is depends on many factors beyond the scope of linearized theory.

Effect of Sweepback

As an example of the effect of sweepback consider the wing-aileron combination in Fig. 2.

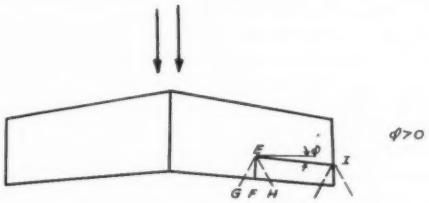

Fig. 2.

By methods similar to those indicated in the previous section, one obtains the following formulas for the pressure and lift in EGH.

$$\frac{C_p}{C_{p_{2\text{-dim.}}}} = \frac{1}{\pi\sqrt{1-a^2}} \arccos\left(\frac{a-t}{1-at}\right) \qquad (4)$$

for $-1 \leq t \leq 1, a < 1 - (m/\text{A. R.})$. The lift coefficient in EGH based on the total area EGH is one-half of the sweepback value. However, for $\varphi > 0$, the area EFH is greater than half the area EGH, so that one will not obtain the correct value of the lift by assuming that C_p is zero in EGF and has its sweepback value in EHF. Actually, one obtains

$$\text{Lift in EGF} = \frac{2q\delta m^2 d^2}{\pi(1-a^2)}\left\{1 - \frac{a \arccos a}{\sqrt{1-a^2}}\right\} \qquad (5)$$

where $a < 1 - (m/\text{A. R.})$.

Triangular Plan Form: Free Edge Supersonic

Consider the wing-aileron combination in Fig. 3. The edge FG is referred to as the free edge. It is

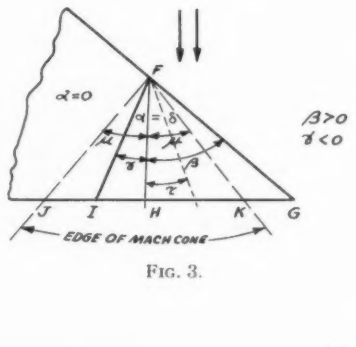

Fig. 3.

supersonic if $\beta > \mu$. If the other edge IF is supersonic, there is no interference between wing and aileron, and the aileron may be treated as a separate wing. Hence, it will be assumed that $|\gamma| < \mu$. Then there is interference between the wing and the aileron in the triangle FJK. This interference effect is easily computed by the method mentioned in Section 1. One starts with a nonlifting wing of plan form IFG and wedge profile with half angle δ. By insertion of a flat plate at zero angle of attack in IJF, the upper and lower surfaces are made independent, and one may change over to zero thickness without disturbing the flow below the wing (in the case $\delta > 0$). The pressure distribution is then found to be

$$\frac{C_p}{C_{p_{2\text{-dim.}}}} = \frac{b}{\pi\sqrt{b^2-1}} \arccos\left(\frac{1-bt}{b-t}\right) + \frac{c}{\pi\sqrt{1-c^2}} \ln\left|\frac{1-ct-\sqrt{(1-c^2)(1-t^2)}}{t-c}\right| \quad (6)$$

for $-1 \leq t \leq 1, b > 1, -1 < c \leq 0$.

$$C_p/C_{p_{2\text{-dim.}}} = b/\sqrt{b^2-1}$$

for $t > 1, b > 1, -1 < c \leq 0$. In the limiting case $b = 1$, Eq. (6) reduces to

$$\frac{C_p}{C_{p_{2\text{-dim.}}}} = \frac{1}{\pi}\sqrt{\frac{1+t}{1-t}} + \frac{c}{\pi\sqrt{1-c^2}} \ln\left|\frac{1-ct-\sqrt{(1-c^2)(1-t^2)}}{t-c}\right| \quad (6')$$

for $-1 \leq t \leq 1, b = 1, -1 < c \leq 0$

By integration it was found that the lift coefficient based on the deflected area has its two-dimensional value. A similar result was obtained for $\gamma = -\beta$ in reference 5. It follows easily from a reversibility theorem due to W. D. Hayes for the case when $|\gamma| > \mu$. For the case $|\gamma| < \mu$, the explanation is to be found in another general theorem to be discussed elsewhere.

Triangular Plan Form: Free Edge Subsonic

In the wing aileron combination shown in Fig. 4, upper and lower surfaces are no longer independent

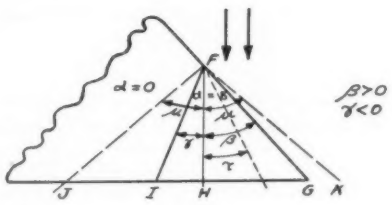

Fig. 4.

since the free edge FG is swept behind the Mach cone. This necessitates different methods of solution. The lifting case may no longer be reduced to the symmetrical case. However, the pressure distribution was easily obtained by the methods of conical flow. The results are:*

$$\frac{C_p}{C_{p_{2\text{-dim.}}}} = \frac{2}{\pi}\left[\frac{c}{\sqrt{1-c^2}} \ln\left|\frac{\sqrt{(1+c)(b-t)}-\sqrt{(b-c)(1+t)}}{\sqrt{(1+b)|t-c|}}\right| + \frac{b}{1+b}\sqrt{\frac{b-c}{1-c}}\sqrt{\frac{1+t}{b-t}}\right] \quad (7)$$

for $-1 \leq t \leq b, 0 \leq b \leq 1, -1 < c \leq 0$.

$$C_p/C_{p_{2\text{-dim.}}} = (2/\pi)(1/\sqrt{1-t^2})$$

for $-1 \leq t \leq 1, b = 1 = -c$.

In spite of the complicated formula for the pressure distribution, the center of pressure and the lift coefficient have the simple forms

$$t_{\text{C.P.}} = (3b + 2c - 1)/4 \quad (8)$$

for $0 \leq b \leq 1, -1 \leq c \leq 0$.

* The method due to Evvard[6] is also well adapted to this problem, especially when the edges of the control surfaces are curved. Calculations carried out independently by H. S. Ribner, by this method, check the results given in the present report.

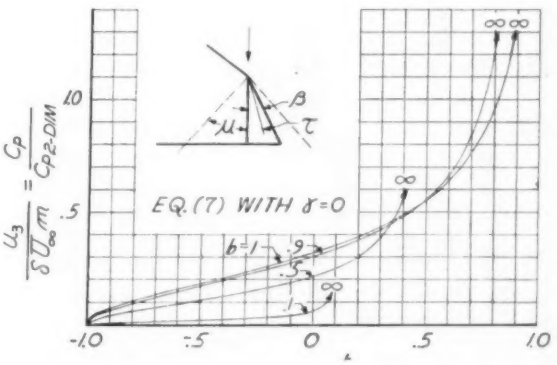

Fig. 5. Effective pressure distribution on narrow triangular aileron with side parallel free-stream direction.

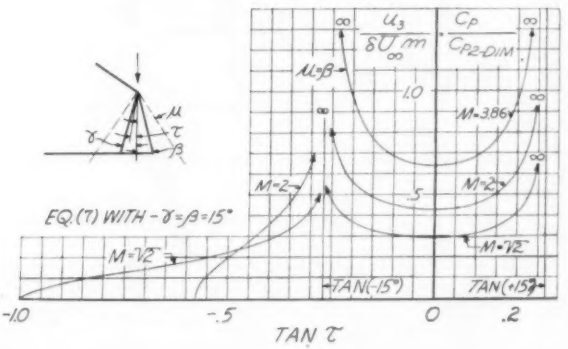

Fig. 6. Effective pressure distribution on narrow triangular aileron with half apex angle = 15°.

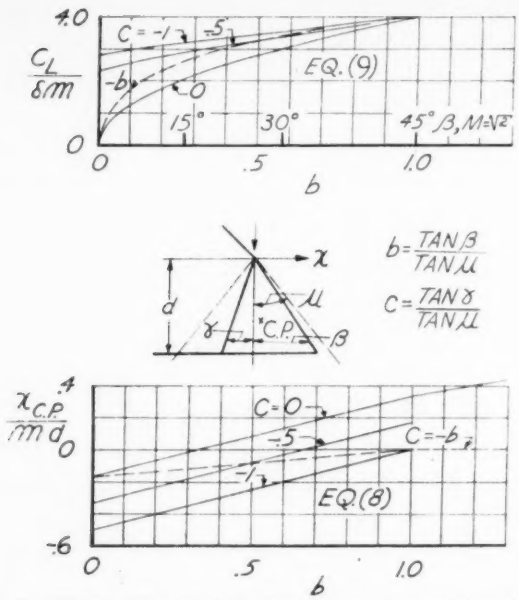

FIG. 7. **Effective lift and center of pressure for several triangular ailerons.**

$$C_l/\delta_m = 4\sqrt{(b - c)/(1 - c)} \qquad (9)$$

for $0 \leq b \leq 1$, $-1 \leq c \leq 0$.

Thus, for a subsonic leading edge, the lift coefficient, based on the deflected area, is smaller than the two-dimensional value. How it varies with the angles β and γ is best seen from the accompanying graphs: Figs. 5–8.

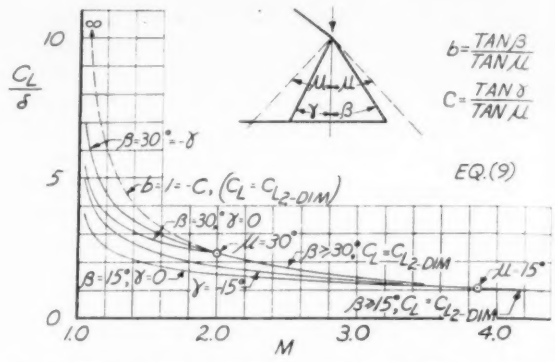

FIG. 8. **Effective lift coefficient vs. Mach Number for several triangular ailerons.**

REFERENCES

[1] Lagerstrom, P. A., and Graham, M. E., *Linearized Theory of Supersonic Control Surfaces*, Douglas Report No. SM-13060, July, 1947.

[2] Hayes, W. D., Browne, S. H., and Law, R. J., *Linearized Theory of Conical Supersonic Flow with Application to Triangular Wings*, North American Report NA-46-818.

[3] Lagerstrom, P. A., JPL Progress Report No. 4–36, December, 1947.

[4] Lagerstrom, P. A., and Graham, M. E., *Downwash and Sidewash Induced by Three-Dimensional Lifting Wings in Supersonic Flow*, Douglas Report SM-13007, April, 1947.

[5] Puckett, A. E., *Supersonic Wave Drag of Thin Airfoils*, Journal of the Aeronautical Sciences, Vol. 13, No. 9, p. 475, September, 1946.

[6] Evvard, J. C., *Distribution of Wave Drag and Lift in the Vicinity of Wing Tips at Supersonic Speeds*, N.A.C.A. T.N. No. 1382, 1947.

Changes of Address

Since the Post Office Department does not as a rule forward magazines to forwarding addresses, it is important that the Institute be notified of changes in address 30 days in advance of publishing date to ensure receipt of every issue of the *Journal* and *Review*.

Notices should be sent directly to the Institute of the Aeronautical Sciences, 2 East 64th Street, New York 21, N.Y.

Efficient Applications of Stringer Panel and Multicell Wing Construction

GEORGE GERARD*
New York University

SUMMARY

Under the structural loading conditions of transonic Mach Number flight, stringer panel type of wing construction and multicell construction were examined to determine the conditions under which each indicated efficient structural applications.

From an analysis of structures of optimum design, stringer panel wings appear to have a wide range of efficient application. Only in the range of extremely high loadings and small thickness ratios does multicell construction indicate efficient applications.

It is to be noted that the results obtained are strongly influenced by practical considerations involved in the manufacture of such wings.

INTRODUCTION

THE EXTERNAL GEOMETRY of transonic aircraft wings is almost wholly dictated by aerodynamic requirements of high Mach Number flight. It is necessary that compromises in aerodynamic design required to attain structural efficiency be kept to a minimum, and, therefore, the structure must be designed within limitations defined almost exclusively by aerodynamic considerations.

Thus, design conditions are encountered wherein the thickness ratio of the wing is small and the bending moments large. Consequently, the cover must carry tremendous loading per inch. Also, it is essential that the cover be nonbuckling, and, while this requirement probably increases structural efficiency, it precludes construction that may cause serious shear lag effects.

Under such conditions, it appears that in the preliminary design stages the designer has a choice of the type of construction (from a purely structural standpoint) which he may utilize for the wing. As shown in Fig. 1, it is possible to use skin-stringer panels for the covers separated by two webs which are more or less conventional design. It is also possible to use a multicell box in which a thick skin is stabilized by a series of webs. Presented with such a choice, it is of interest to investigate which type of construction has efficient structural applications from a weight standpoint.

SYMBOLS

Refer to Fig. 1:

b_w = thickness of wing, in.
c = empirical term, a measure of stringer panel efficiency
E = modulus of elasticity, lbs. per sq.in.
K = instability coefficient, $K = \pi^2 k/12(1 - \nu^2)$
L' = effective rib spacing (includes end fixity coefficient), in.
N_x = loading per chordwise inch, lbs. per in.
n = number of multicell bays ($n + 1$ = number of webs)
nb_s = structural chord, in.
t = thickness, in.
σ = stress, lbs. per sq.in.
Σ = solidity
$\gamma, \bar{c}, \bar{\varphi}$ = variables defined in Eq. (17)

Subscripts

$cr.$ = critical
w = web
s = upper wing surface or compression cover
t = lower wing surface or tension cover
$-$ = – (over a symbol) denotes average or effective value

ANALYSIS

Assumptions

(A) It is assumed that the modulus of elasticity, E, is constant, and no attempt is made to include corrections for inelastic buckling in the general case.

(B) The wing is assumed to act under pure bending only, and, consequently, the structural weight required to carry shear loads is not considered.

(C) The bending load is assumed to be resisted by the idealized boxes shown in Fig. 1, consisting of a "structural chord" nb_s and thickness b_w.

(D) In order to have a reasonable criterion by which the upper and lower wing surfaces could be designed, it was decided that the lower surface would be designed to carry one-half the loading the upper surface carries.

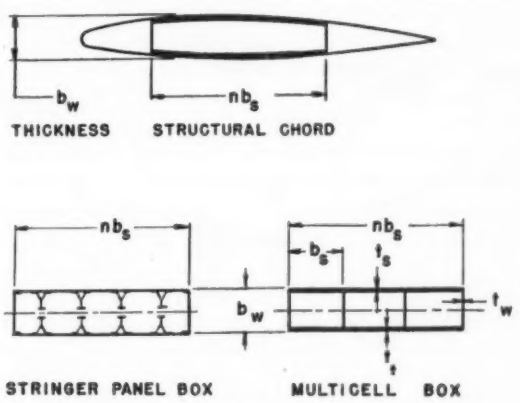

FIG. 1. Idealized box sections used for analysis.

Received July 28, 1948.

* Instructor, Guggenheim School of Aeronautics, College of Engineering.

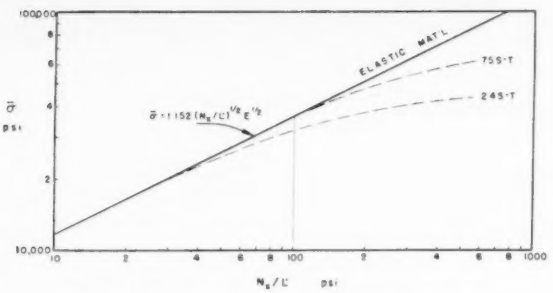

FIG. 2. Optimum curve for Y-stringer panels.[2]

This would correspond approximately to an inverted flight condition, and, consequently, both surfaces would be designed from consideration of axial compressive loading.

Optimum Panel Design

If the wing utilizes skin-stringer panel construction as shown in Fig. 1, it is necessary to know, for the purposes of general analysis, the geometry of panels of minimum weight.

The design of optimum panels was discussed by Zahorski,[1] who suggested that the optimum panel stress for a given compressive loading was obtained when instability of the skin occurred simultaneously with primary and secondary instability of the stringers. For this condition, the optimum stress is given

$$\bar{\sigma} = c(EN_x/L')^{1/3} \tag{1}$$

where c depends upon the crippling stress of the stringer and the panel geometry.

The N.A.C.A.[2] has conducted an extensive program to determine optimum stringer panel proportions that would result in minimum weight for a given loading. The results of this program have shown that, of all shapes tested, use of a Y stringer panel results in minimum weight. These results are shown on Fig. 2.

Also drawn on Fig. 2 is an extrapolation of the straight-line portion of the curve such as would probably exist for an aluminum alloy with an extremely high proportional limit. It is interesting to note that the slope of this line is exactly one-half as predicted by Eq. (1),* although this line represents the envelope to a set of semiempirical curves obtained by varying the panel geometry.

By taking the modulus of elasticity of the panels, which were constructed of extruded 75S-T Y-stringers and Alclad 75S-T sheet as $E = 10 \times 10^6$ lbs. per sq.in., the equation of the optimum curve is

$$\bar{\sigma} = 1.152(EN_x/L')^{1/3} \tag{2}$$

From Eqs. (1) and (2), c, which is the direct measure of the structural efficiency of the panel, has a value for the Y-stringer panel of

$$c = 1.152 \tag{3}$$

By comparing values of this coefficient for various stringer shapes, a direct insight into the panel efficiency is obtained.

From Zahorski's analysis,[1] the coefficient c has its highest value when the crippling stress and the radius of gyration of the stringer are highest and when the stringer spacing is close. The N.A.C.A.[2] investigation has substantiated this and has also shown that riveting of the stringer to the skin must be strong—i.e., large diameter rivets closely spaced.

It is to be noted that, since the optimum curve is an envelope, its use ignores existence of only standard sheet gages and presupposes a large variety of extruded stiffener sizes. All of these considerations that lead to high structural efficiency present increasing difficulties in construction.

Solidity of Stringer Panel Wing

When considering the weight of a stringer panel wing section shown in Fig. 1, it is convenient to utilize the concept of "solidity." Solidity is defined as the ratio of the area of the elements comprising the cross section to the total area of the cross section enclosed by the outer contours. It is evident that the solidity is directly proportional to the weight of the structural material.

In addition to the general assumptions of this analysis, the following assumptions pertain: (E) the weight of the ribs that are required to stabilize the cover is assumed negligible; (F) the centroidal depth of the stringer panel box, is assumed to be equal to the total depth, b_w.

The effective thickness of the upper stringer panel is

$$\bar{t}_s = N_x/\bar{\sigma} \tag{4}$$

Substituting for $\bar{\sigma}$ from Eq. (1),

$$\bar{t}_s = (1/c)(N_x L'/E)^{1/3} \tag{5}$$

According to assumption (D),

$$N_{x_t} = (1/2)N_x$$

therefore

$$\bar{t}_t = (1/c)(N_x L'/2E)^{1/3} \tag{6}$$

The solidity of the box comprising the two covers and two webs shown in Fig. (1) is given by

$$\Sigma = [(\bar{t}_s + \bar{t}_t)nb_s + 2b_w t_w]/nb_s b_w \tag{7}$$

Substituting Eqs. (5) and (6) for $\bar{t}_s$, $_t$ and noting that, for a simply supported web in bending for which $\sigma_{cr.} = \bar{\sigma}$,

$$t_w/b_w = \sqrt{12(1 - \nu^2)\bar{\sigma}/25\pi^2 E}$$

the following equation for solidity is obtained

* The value of the exponent is obtained from the slope of the logarithmic plot.

$$\Sigma = \frac{(1.707/c)\,(N_x L'/E)^{1/2}}{nb_s}\left(\frac{nb_s}{b_w}\right) + \sqrt{\frac{12(1-\nu^2)c}{25\pi^2}}(N_x/L'E)^{1/4}\left(\frac{b_w}{nb_s}\right) \quad (8)$$

Solidity of Multicell Wing

The method of analysis for determining the optimum number of webs to be used for a multicell wing has been presented in a previous paper.[3] The solidity of a multicell is given by

$$\Sigma = [nb_s t_s + (n+1)b_w t_w + nb_s t_t]/nb_s b_w \quad (9)$$

The thicknesses of the compression cover and webs are determined by the condition that the members are simply supported and buckle simultaneously. Thus,

$$t_w/t_s = (2/5)(b_w/b_s) \quad (10)$$

and since

$$N_x = \sigma_{cr} t_s = K_s E t_s^3/b_s^2$$

Thus

$$t_s = \sqrt[3]{N_x b_s^2/K_s E} \quad (11)$$

The thickness of the tension skin is determined from assumption (D). Thus, from Eq. (11)

$$t_t/t_s = \sqrt[3]{1/2} = 0.794 \quad (12)$$

Combining Eqs. (10) to (12) with Eq. (9) as shown in reference 3, the expression for solidity of a multicell box that includes a lower surface designed to carry one-half the load of the upper surface becomes

$$\Sigma = \sqrt[3]{\frac{N_x}{K_s E n b_s}}\, n^{1/3}\left[\frac{1.794}{n}\left(\frac{nb_s}{b_w}\right) + \frac{2(n+1)}{5}\left(\frac{b_w}{nb_s}\right)\right] \quad (13)$$

The optimum number of webs which will yield minimum solidity and consequently minimum weight is obtained from the condition $\partial\Sigma/\partial n = 0$. Performing the differentiation leads to the result:

$$n(4n+1) = 5(1.794)(nb_s/b_w)^2 \quad (14)$$

In reference 3, the multicell was considered to have a lower surface designed to carry a tension load equal to the compressive load of the upper surface. Hence, the thickness of the tension skin was independent of the number of webs used, and for this case the optimum number of webs is given by

$$n(4n+1) = 5(nb_s/b_w)^2 \quad (15)$$

From Fig. 3, it is evident that use of Eq. (15) results in a smaller number of webs for a given structural thickness ratio, b_w/nb_s, than Eq. (14). Furthermore, use of the optimum number of webs given by Eq. (15) results in about a 4 per cent increase in solidity over that obtained by utilizing Eq. (14). Since the weight penalty is small for the large reduction in number of webs, it was thought desirable to use Eq. (15) in conjunction with Eq. (13) in this analysis, and this procedure was followed.

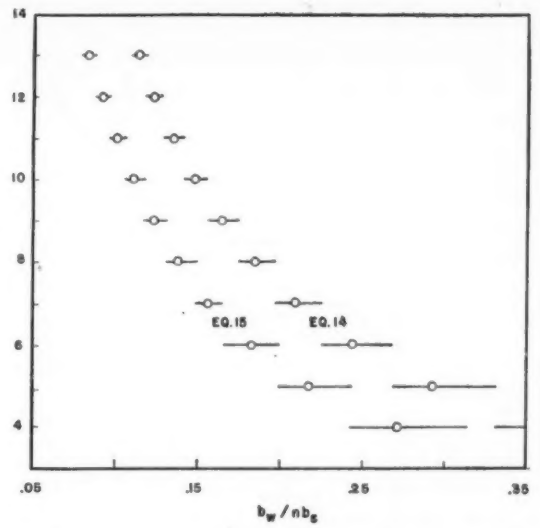

FIG. 3. Optimum number of bays for a multicell box according to Eqs. (14) and (15).

EFFICIENT STRUCTURAL APPLICATIONS

An examination of the solidity equations for the stringer panel and multicell box, Eqs. (8) and (13), indicates that the following variables are involved:

N_x = cover loading per inch
b_w/nb_s = structural thickness ratio
nb_s = structural chord
L' = effective rib spacing

(n, the number of bays, is specified by the structural thickness ratio for optimum conditions.)

Consequently, for a given structural chord and effective rib spacing, it is possible to construct a chart of solidity versus structural thickness ratio for various values of compressive loading. Such a chart was

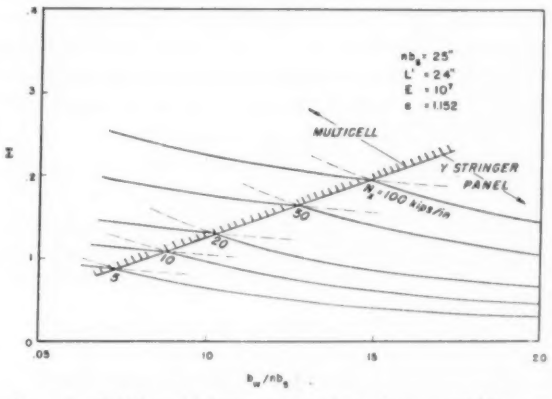

FIG. 4. Solidity–thickness ratio chart for a specific case using optimum conditions. Intersection of solidity curves of stringer panel box and multicell determine boundary curve.

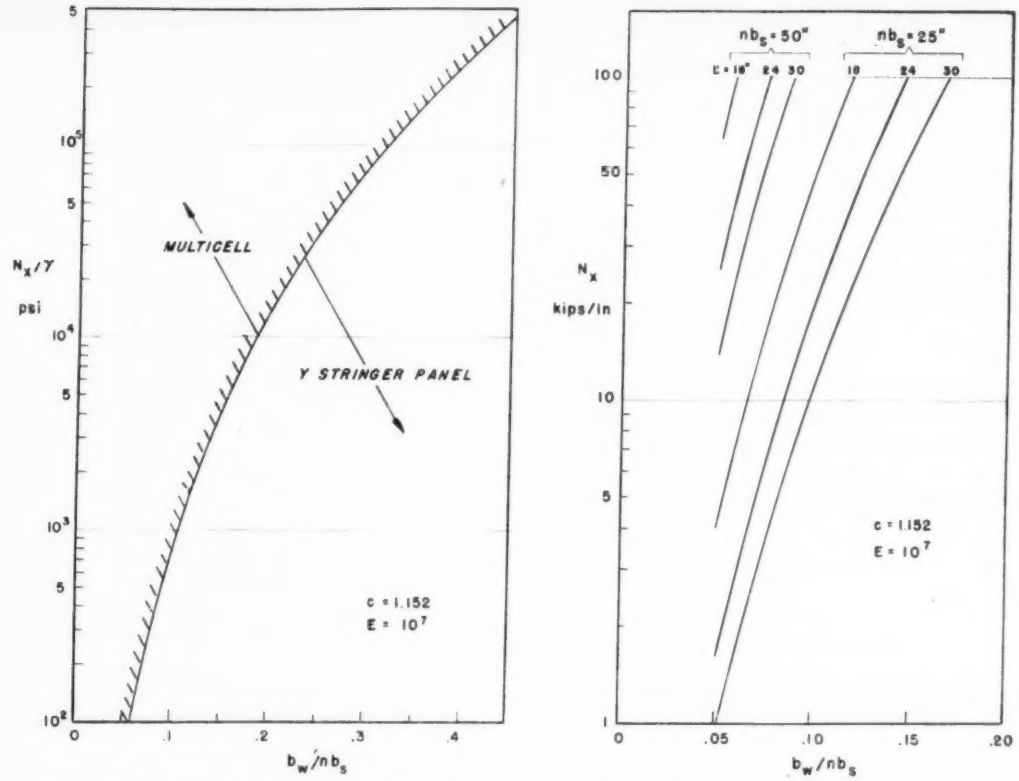

FIGS. 5 and 6. Boundary curves that determine efficient structural applications of each type of construction.

drawn in Fig. 4 for the specific case of $nb_s = 25$ in., $L' = 24$ in.

In Fig. 4, the regions of efficient application of both types of construction are clearly evident. To the right of the intersection or boundary curve, a stringer panel box is more efficient, while, to the left of this curve, the multicell box is more efficient.

Boundary Curve

By equating Eqs. (8) and (13), the boundary curve can be directly determined without constructing a chart similar to Fig. 4. In doing so, the portion of the solidity contributed by the two webs in the stringer panel box may be neglected, since it was found by calculations that in the region of the intersection the webs contribute less than 5 per cent to solidity. Thus, equating Eqs. (8) and (13),

$$\frac{(1.707/c)(N_x L'/E)^{1/2}}{nb_s}\left(\frac{nb_s}{b_w}\right) = \sqrt[3]{\frac{N_x}{K_s E nb_s}}\, n^{1/3}\left[\frac{1.794}{n}\left(\frac{nb_s}{b_w}\right) + \frac{(2n+1)}{5}\left(\frac{b_w}{nb_s}\right)\right] \quad (16)$$

Rearranging terms,

$$N_x \frac{(L')^3}{(nb_s)^4} = E\left(\frac{c}{1.707\sqrt[3]{K_s}}\right)^6 \times n^2\left[\frac{1.794}{n} + \frac{2(n+1)}{5}\left(\frac{b_w}{nb_s}\right)^2\right]^6 \quad (17)$$

Now, introducing the following

$$\gamma = (nb_s)^4/(L')^3$$
$$\bar{c} = c/1.707\sqrt[3]{K_s}$$
$$\bar{\varphi} = n^{1/3}\left[\frac{1.794}{n} + \frac{2(n+1)}{5}\left(\frac{b_w}{nb_s}\right)^2\right]$$

Eq. (17) can be written in the form

$$N_x/\gamma = \bar{c}^6 \bar{\varphi}^6 E \quad (18)$$

The $\bar{\varphi}$ term can be calculated from data of Fig. 3, since the optimum number of webs depends solely upon the structural thickness ratio. Thus, by letting c take on the value given in Eq. (3) and letting $K_s = 3.64$, as for an efficiently designed simply supported plate of negligible taper,[4] and also letting $E = 10^7$ lbs. per sq.in. for aluminum alloys. Fig. 5 can be drawn.

It is evident that the boundary curve is strongly influenced by the nature of c, since it appears as a sixth-order term in Eq. (18). Thus, any departure from optimum panel dimensions such as use of standard sheet gages, wider spacing of stiffeners, and larger rivet pitch would result in a considerable shift in the boundary curve.

Similarly, use of less than the optimum number of webs would result in a shift in the boundary curve, since the $\bar{\varphi}$ term also appears as a sixth-power term. In reference 3, however, it was found that a reduction in the number of webs of two or three from the optimum

number resulted in an increase of only 5 per cent at low values of structural thickness ratios.

It is interesting to note that the modulus of elasticity, E, enters into the equation for the boundary curve. Use of a steel alloy rather than an aluminum alloy would move the boundary curve to the left on Fig. 5, whereas use of a magnesium alloy would shift the curve to the right. It is not evident what effect exceeding the proportional limit would have on the boundary curve, particularly since the effective modulus is a function of stress rather than loading.

In Eq. (18), the γ term is a function of the structural chord and the effective rib spacing. To permit a better understanding of where the transition from stringer panel to multicell construction occurs, Fig. 6 was drawn for specific values of L' and nb_s. This figure indicates that, for optimum construction, the boundary curve occurs at extremely low structural thickness ratios. Consequently, stringer panel construction can be utilized more efficiently than multicell construction in almost the entire range of thickness ratios.

Discussion

The analysis conducted on structures of optimum design indicated that the transition from stringer panel to multicell construction occurs in possibly only a few highly specialized instances where the loading may be high or the thickness ratio may be low. The feasibility of constructing wings of the type specified by optimum considerations does not enter into the analysis, and, hence, constructional details may lead to conclusions that invalidate the result of the analysis in certain thickness ranges. Consequently, it is pertinent to consider what effect deviations from optimum construction would have on the boundary curve. While the analysis involves certain ratios, it is necessary to consider the absolute dimensions of certain parameters in establishing limits.

Stringer Depth

An important consideration that would provide a cutoff to the boundary curve is that the stringer depth should probably not exceed one-quarter of the total depth of the structure. If the stringer were made considerably deeper, there is a definite loss in efficiency because the centroidal depth of the covers decreases, and also the stress distribution is such that the stress decreases from a maximum at the surface to zero at the center of the box. In addition, if the depth were too great, the stringers would touch.

Riveting

Rivet pitch and diameter have an appreciable effect on the strength of a stringer panel, particularly at high values of loading. According to reference 2, panels of optimum design, using N.A.C.A. countersinking methods, require an average rivet pitch equal to 6.5 times the skin thickness and a rivet diameter of 1.2 times the combined skin and stringer leg thicknesses.

The rivet diameter requirement can be met, but the pitch requirement is such that the rivet heads are practically touching. An investigation was made using the test data of reference 5 to determine the effect of increasing the rivet pitch to a value more likely to be used by the aircraft industry. For a rivet pitch equal to 15 times the skin thickness, which appears to be a reasonable criterion based on industry practice, a reduction in failing stress, δ, of approximately 15 per cent from the optimum value occurred for values of N_x/L' greater than 0.5 kips per in.

Stringer Spacing

Optimum conditions require that the skin and stringers become unstable simultaneously necessitating close stringer spacing. If, for example, the centerline spacing of the Y stringers is increased to 4 in. from the optimum spacing, the data of reference 2 indicated a reduction of about 20 per cent in failing stress for a given N_x/L'.

Other Variables

Other considerations that reduce the failing stress from the optimum value are use of standard sheet gages and only a limited variety of extruded Y stringer sizes. Since the Y stringer has the highest values of c, [Eq. (3)] and was used in the analysis, use of a Z stringer (which has the advantages that it can be formed, requires fewer rows of rivets, and also results in better aerodynamic fairing) would result in a lower value of c and a consequent reduction in failing stress.

Multicell Webs

From a manufacturing standpoint, it appears difficult to use more than three bays in a multicell wing. Consequently, this factor tends to compensate at low thickness ratios for the above factors which tend to decrease the efficiency of stringer panels. The effect of using only three bays can be estimated from reference 3.

It is evident that the range of variables that influence conditions other than optimum is so great as to preclude a general investigation for other than optimum conditions. For such cases, it is necessary to confine the study to specific cases. This can be done by constructing a chart similar to Fig. 4 for the types of stringer panels and multicell construction considered feasible.

Conclusions

Based on optimum design of stringer panels and multicell wings and the assumptions of the analysis, it appears that stringer panel wings have a wide range of

efficient structural application. Only in the region of extremely high loadings and small thickness ratios does multicell construction indicate efficient application.

However, the practical considerations involved in the manufacture of such wings influence strongly the boundary between the two regions of efficient application. Consequently, an analysis such as presented herein should be made for the types of construction considered feasible to decide the type of structure to be used in specific cases.

References

[1] Zahorski, A., *Effects of Material Distribution on Strength of Panels*, Journal of the Aeronautical Sciences, Vol. 11, No. 3, pp. 247–253, July, 1944.

[2] Dow, N. F., and Hickman, W. A., *Design Charts for Flat Compression Panels Having Longitudinal Extruded Y-Section Stiffeners and Comparison with Panels Having Formed Z-Section Stiffeners*, N.A.C.A. T.N. No. 1389, August, 1947.

[3] Gerard, G., *Optimum Number of Webs Required for a Multicell Box Under Bending*, Journal of the Aeronautical Sciences, Vol. 15, No. 1, pp. 53–56, January. 1948.

[4] Pines, S., and Gerard, G., *Instability Analysis and Design of an Efficiently Tapered Plate Under Compressive Loading*, Journal of the Aeronautical Sciences, Vol. 14, No. 10, pp. 594–599, October, 1947.

[5] Dow, N. F., and Hickman, W. A., *Effect of Variation in Diameter and Pitch of Rivets on Compressive Strength of Panels with Z-Section Stiffeners. Panels of Various Lengths with Close Stiffener Spacing*, N.A.C.A. T.N. No. 1421, September, 1947.

Notice to Contributors

Manuscripts submitted for publication *must be* double- or triple-spaced originals. There should be wide margins on both sides of the sheets and triple spacing around formulas to allow for the marking of directions for the printer.

Original drawings (jet black India ink on white paper or tracing cloth) should accompany the manuscript. *(Blueprints are not acceptable.)* Photographs *must be* on glossy white paper.

Only the simplest formulas should be typewritten; all others should be carefully written in pen and ink. The difference between capital and lower-case letters and Greek symbols should be clearly distinguished.

See inside back cover of this issue for further details.

The Boundary Layer of Yawed Infinite Wings

J. M. WILD*
Cornell University

SUMMARY

An approximate solution to the boundary-layer equations for an infinite yawed cylinder is obtained by an extension of the Kármán-Pohlhausen method. From this solution the direction of the flow in the boundary layer and the displacement and momentum thicknesses of the spanwise flow component may be calculated.

To illustrate this method, the boundary layer over a yawed infinite wing at a lift coefficient just below the stall is calculated, and typical results are presented graphically. A strong spanwise flow is found which is in qualitative agreement with experimental observations.

INTRODUCTION

THE UNSATISFACTORY AERODYNAMIC CHARACTERISTICS of sweptback wings at high angles of attack, coupled with their increasing use on tailless and high-speed aircraft, have emphasized a significant discrepancy between experimentally obtained results and theoretical predictions of these characteristics when the theory is based upon the frictionless-fluid approximation. Accumulating experimental evidence—e.g., tuft studies indicating large spanwise outflows in the boundary layers of these wings—points to the strong possibility that viscous effects can no longer be safely neglected in sweptback or yawed finite-wing theories. To explore this possibility, a program has been laid out to investigate the three-dimensional boundary layers of finite wings and to determine the effects of such flows upon the wing characteristics. Sears,[1] as a first step in this program, has calculated the cases of the laminar boundary layer of the yawed infinite flat plate and of a certain yawed infinite cylinder, both at zero lift.

In continuation of this program, the laminar boundary layer of an infinite wing just below the stall is considered here. It will be shown that an approximate solution to this problem may be obtained by means of a simple extension of the Kármán-Pohlhausen method.

THE BOUNDARY-LAYER EQUATIONS

It has been shown by Prandtl,[2] and independently by various other authors,[1, 3, 4] that the Navier-Stokes equations (in the boundary-layer approximation) for a uniform, yawed cylinder infinite in extent in a steady, incompressible flow reduce to the form

$$u\frac{\partial u}{\partial x} + w\frac{\partial u}{\partial z} = -\frac{1}{\rho}\frac{\partial p}{\partial x} + \nu\frac{\partial^2 u}{\partial z^2} \tag{1}$$

$$\partial p/\partial z = 0 \tag{2}$$

$$u\frac{\partial v}{\partial x} + w\frac{\partial v}{\partial z} = \nu\frac{\partial^2 v}{\partial z^2} \tag{3}$$

where x, y, z are curvilinear coordinates defined as in Fig. 1, p is the static pressure, ρ is the density, ν is the kinematic viscosity, and u, v, w are the velocity components in the directions x, y, z, respectively. In particular, these authors point out that Eqs. (1) and (2) are independent of the spanwise velocity component and that these equations, along with the equation of continuity,

$$(\partial u/\partial x) + (\partial w/\partial z) = 0 \tag{4}$$

constitute the usual two-dimensional problem of plane flow about the same cylinder at zero yaw in a free stream of velocity U, the velocity component in the x-direction.

Approximate solutions to the plane problem were provided by Pohlhausen,[5] who, at the suggestion of von Kármán, expressed the boundary-layer velocity profile in the form of a quartic

$$\frac{u}{u_1} = A_0 + A_1\left(\frac{z}{\delta_x}\right) + A_2\left(\frac{z}{\delta_x}\right)^2 + A_3\left(\frac{z}{\delta_x}\right)^3 + A_4\left(\frac{z}{\delta_x}\right)^4, \qquad 0 \le z \le \delta_x \tag{5}$$

where u_1, is the potential velocity outside the boundary layer, δ_x is the boundary-layer thickness, and the A_i's are functions of x alone, determined to satisfy certain boundary conditions as well as Eq. (2). The boundary-layer thickness δ_x is then calculated to satisfy Eqs. (1)

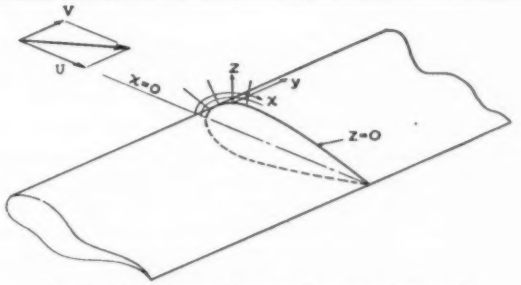

FIG. 1. Sketch showing coordinate system used.

Presented at the Aerodynamics Session, Sixteenth Annual Meeting, I.A.S., New York, January 26–29, 1948.

* Associate Professor of Aeronautical Engineering.

and (4). This solution is well known and has been applied to a wide variety of problems with satisfactory results.

Pohlhausen's method may be extended to the determination of the boundary-layer velocity component in the y-direction on an infinite yawed wing—i.e., to satisfy Eq. (3). To retain the same degree of approximation as Pohlhausen, it will be assumed that the profile of the velocity component v can be expressed as a quartic of the form

$$\frac{v}{v_1} = B_0 + B_1\left(\frac{z}{\delta_y}\right) + B_2\left(\frac{z}{\delta_y}\right)^2 + B_3\left(\frac{z}{\delta_y}\right)^3 + B_4\left(\frac{z}{\delta_y}\right)^4, \qquad 0 \leq z \leq \delta_y \quad (6)$$

where v_1 is the local potential velocity outside of the boundary layer (in the case of the infinite wing, a constant equal to the y-component V of the free-stream velocity), and the B_i's are functions of x. The "boundary-layer thickness" of the spanwise velocity component, δ_y, is the distance over which v increases from zero at the airfoil surface to its potential-flow value, just as δ_x represents the corresponding distance for the component u. For brevity, δ_x will be referred to as the thickness of the "u-layer" and δ_y as that of the "v-layer."*

The functions $B_0, B_1, \ldots$ are now required to satisfy the following boundary conditions:

$$\left.\begin{array}{ll} v = 0 & \text{when } z = 0 \quad \text{(Prandtl no-slip condition)} \\ v'' = 0 & \text{when } z = 0 \quad \text{(cf. reference 6)} \\ v = v_1 & \text{when } z = \delta_y \\ v' = 0 & \text{when } z = \delta_y \\ v'' = 0 & \text{when } z = \delta_y \end{array}\right\} \text{(To assure a smooth transition to the potential velocity)} \quad (7)$$

where the primes denote differentiation with respect to z. Under these conditions Eq. (6) becomes

$$\frac{v}{v_1} = 2\left(\frac{z}{\delta_y}\right) - 2\left(\frac{z}{\delta_y}\right)^3 + \left(\frac{z}{\delta_y}\right)^4, \qquad 0 \leq z \leq \delta_y \quad (8)$$

In this equation it is of interest to note that the nondimensional profile of the v-layer is constant and, in particular, that separation profiles cannot occur (i.e., $v' \neq 0$ for $z = 0$). This is consistent with the fact that for the infinite wing there are no spanwise pressure gradients.

By integration of Eq. (3) with respect to z, or from momentum considerations, the momentum form of the v-layer equation is

$$\frac{d}{dx}\int_0^{\delta_y} u(v - v_1)dz = -\nu\left(\frac{\partial v}{\partial z}\right)_{z=0} \quad (9)\dagger$$

If the values of u and v from Eqs. (5) and (8) are introduced into Eq. (9) and the integration carried out, an ordinary differential equation for δ_x/δ_y results, the form of which depends upon the relative magnitudes of δ_x and δ_y. Let ξ denote δ_x/δ_y; then for $\delta_y \geq \delta_x$ $(\xi \leq 1)$,

$$\xi' = \frac{2\frac{\xi}{\lambda} - A\left(1 + \frac{u_1}{u_1'}\frac{\delta_x'}{\delta_x}\right) - C\frac{u_1}{u_1'}}{B(u_1/u_1')} \quad (10a)$$

and for $\delta_y \leq \delta_x (\xi \geq 1)$,

$$\xi' = \frac{2\frac{\xi^3}{\lambda} - \alpha\left(1 + \frac{u_1}{u_1'}\frac{\delta_x'}{\delta_x}\right) - \gamma\frac{u_1}{u_1'}}{\beta(u_1/u_1')} \quad (10b)$$

where the prime denotes differentiation with respect to x, and

$$\left.\begin{array}{l} \lambda = u_1'\delta_x^2/\nu, \text{ following Pohlhausen} \\ A, B, C \\ \alpha, \beta, \gamma \end{array}\right\} \text{ are functions of } A_i, B_i, \text{ and } \xi, \text{ as given in the appendix} \quad (11)$$

The terms (11) are to be evaluated from the numerical results of the two-dimensional von Kármán-Pohlhausen solution so that, in general, an analytical solution for ξ is not possible. It can be seen, from Eqs. (10a) and (10b), moreover, that at the forward stagnation line $(x = 0)$ $u_1 = 0$ and the denominator vanishes. Thus, ξ' is infinite at the stagnation line unless the numerator also vanishes. Rejecting an infinite value of ξ' as physically impossible, one obtains from the appropriate Eqs. (10a) and (10b) a quintic equation giving the possible values of ξ at the stagnation line. A numerical solution indicates that the only physically acceptable value is $\xi = 0.766$. Thus, the initial condition for the solution of Eqs. (10) is $\xi = 0.766$ at $x = 0$. Since this is a singular point, the best method for obtaining a solution appears to be that of isoclines. An analogous situation exists in the two-dimensional problem and is discussed in various references.[5, 6]

From this solution, the v-layer profile is at once obtained, and such auxiliary results as the direction of flow in the boundary layer and the displacement and momentum thicknesses of the v-layer are readily calculated. The calculations are not essentially complicated by the fact that a choice between Eqs. (10a) and (10b) must be made. The upper and lower parts of the isocline diagram are simply calculated from the respective equations, so that the shift is always made when the solution crosses the line $\xi = 1$.

Numerical Results

The configuration chosen to illustrate the above method is an infinite elliptic cylinder, with the ratio of

* To be more exact, of course, there exists only one boundary layer and a corresponding boundary-layer thickness over any body—namely, the layer wherein the resultant velocity vector deviates substantially from potential-flow vector. The present nomenclature is used for convenience. The true boundary-layer thickness at any point of the surface is equal to the greater of δ_x and δ_y

† Cf. reference 7.

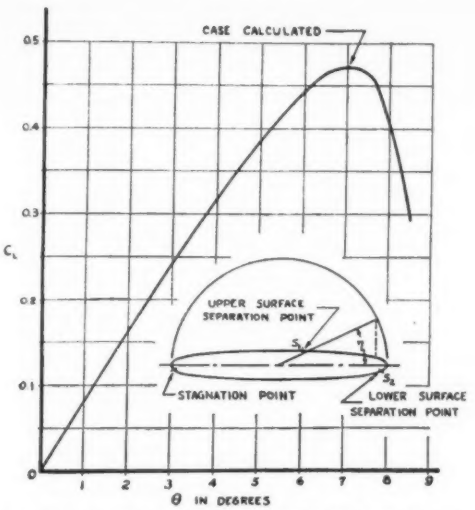

FIG. 2. Lift curve of elliptical cylinder investigated.

the major to the minor axes of 6:1, at an angle of attack of 7° relative to the U-velocity component. This corresponds to the maximum lift coefficient (shown in Fig. 2) as calculated by Howarth.[8] In carrying out this lift calculation, Howarth obtained the Pohlhausen solution for the laminar boundary layer over the unyawed cylinder. These data were used in the subsequent calculations and materially reduced the labor involved in obtaining the three-dimensional solution. In general, it would be necessary to obtain the two-dimensional solution before proceeding to the three-dimensional case.

It was convenient to use the eccentric angle η (defined in Fig. 2) as the independent variable in carrying out the integration of Eqs. (10a) and (10b), rather than x. The integration of this equation by the isocline method is shown in Fig. 3, the solution being indicated by the heavy solid line. The dashed lines are two "neighboring" solutions constructed to check the accuracy of the isocline procedure but not satisfying the initial condition of finite ξ' at $x = 0$.

Typical profiles of the velocity components u and v corresponding to this solution are shown in Fig. 4. In Fig. 5 the "limiting streamline" at $z = 0$ is drawn on a projected plan view of a wing with 45° sweep, in comparison with the corresponding potential-flow streamline. Since the stagnation point for plane flow about the cylinder at this incidence is on the lower surface, the flow at this location is not shown in this figure. The short-line segments on this figure have been drawn in the "limiting" direction of the flow at the surface—i. e.,

$$dy/dx = \lim_{z \to 0} (v/u)$$

Thus, they may be imagined as representing yarn tufts attached to the surface of the airfoil to indicate the flow direction. For other angles of sweepback, the flow direction may be obtained by multiplying these slopes by the tangent of this angle.

In practice, the tufts undoubtedly assume a direction corresponding to some intermediate streamline or streamlines. From the available data it appears that these intermediate streamlines lie between the limiting cases shown, but the w-velocity component would have to be determined in order to draw them accurately.

The ratio of the displacement thicknesses

$$\frac{\delta_x^*}{\delta_y^*} = \frac{\int_0^{\delta x} [1 - (u/u_1)]dz}{\int_0^{\delta y} [1 - (v/v_1)]dz} \tag{12}$$

is shown in Fig. 6. Similarly, the ratio of the momentum thicknesses

$$\frac{\theta_{xx}}{\theta_{yy}} = \frac{\int_0^{\delta x} (u/u_1)[1 - (u/u_1)]dz}{\int_0^{\delta y} (v/v_1)[1 - (v/v_1)]dz} \tag{13}$$

is shown in Fig. 7.

Concluding Remarks

A laminar boundary layer such as was assumed in the numerical calculations above could, in practice, exist only at extremely low values of the Reynolds Number because of the inherent instability of such layers. The results obtained here, nevertheless, appear to be in at least qualitative agreement with tuft observations on actual sweptback wings, since a strong outward flow in the boundary layer is obtained. This outward flow is more pronounced than that on the symmetrical cylinder investigated by Sears,[1] presumably because of the stronger chordwise pressure gradients that are present. It would appear from this, at least qualitatively, that the outward flow is increased with increasing lift. This is also in agreement with tuft observations.

It should be noted, however, that this spanwise component of flow does not have any effect upon such aerodynamic characteristics as the lift, transition, or separation for the infinite wing. In fact, the basic Eqs. (1)–(4) are such as to preclude the possibility of any such effects occurring.* It appears that these effects can arise only on finite wings.

The present extension of Pohlhausen's procedure to the yawed wing appears suitable for estimation of the laminar boundary-layer characteristics in certain areas of sweptback wings. In view of the analogy between the v-layer and the temperature layer near a heated surface,[1] the same procedure should be useful in analogous heat-transfer calculations for either straight or swept wings.

* A more detailed discussion of this point is given in references 1 and 4.

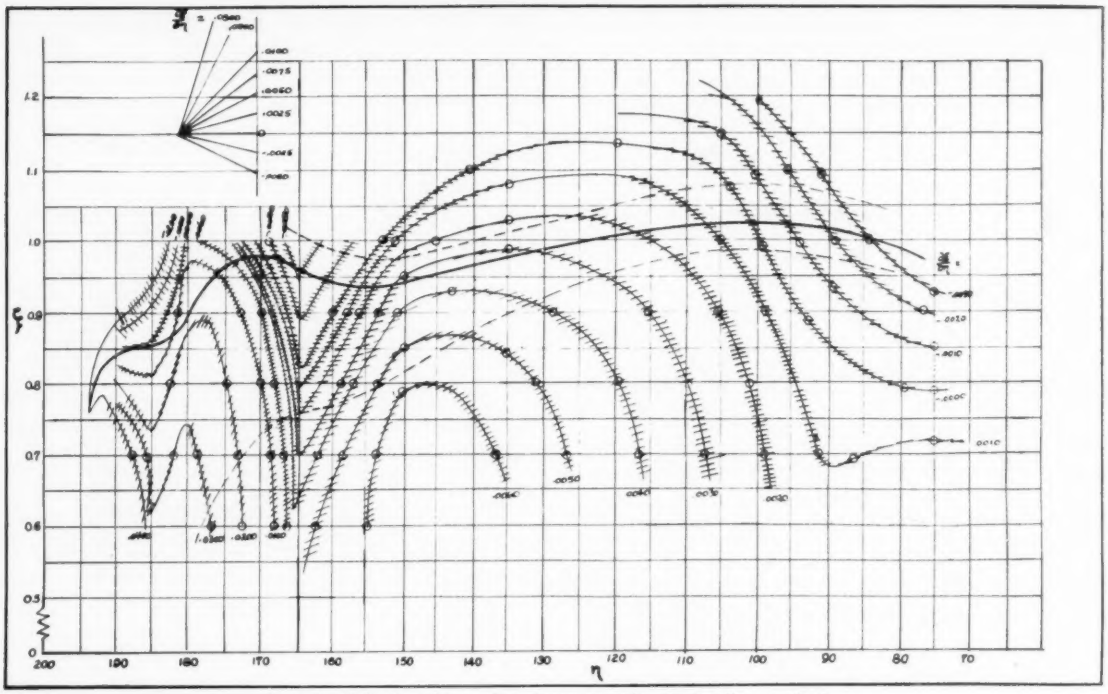

FIG. 3. Solution of boundary-layer equation by isocline method.

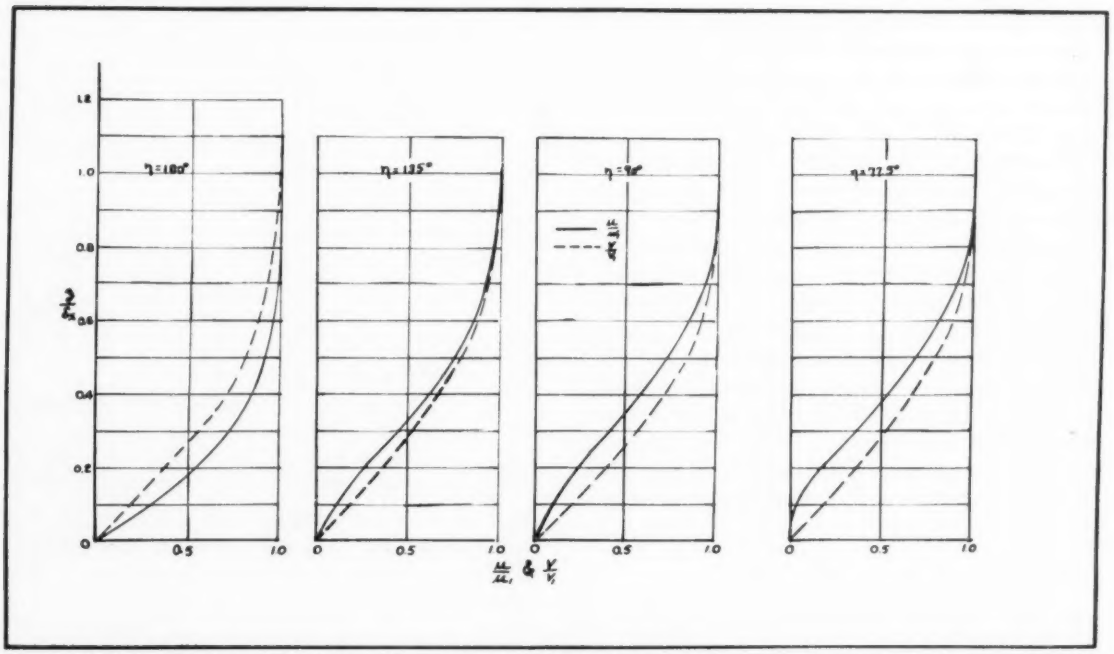

FIG. 4. Typical spanwise and chordwise velocity components in the boundary layer at varying chordwise locations along the wing.

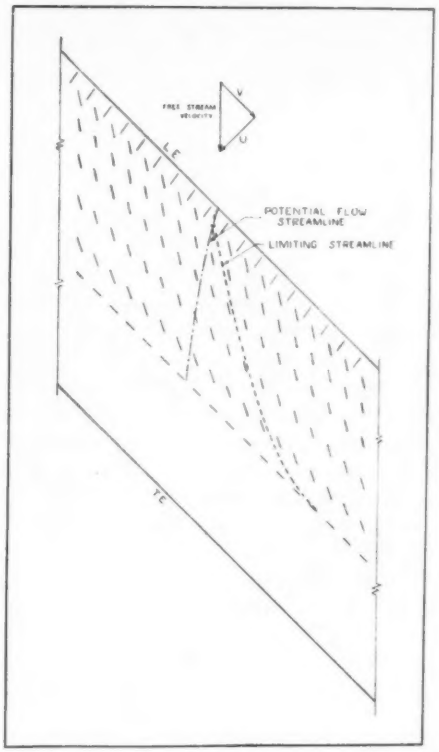

FIG. 5. Plan view of the potential flow and limiting streamline at the surface and surface tufts of wing; angle of yaw, 45°.

APPENDIX

The coefficients in Eqs. (10a) and (10b) may be evaluated from the following:

$$A = 0.3\xi^{-1} + D_1 - D_2\xi + D_3\xi^3 - D_4\xi^4$$
$$B = -0.3\xi^{-2} - D_2 + 3D_3\xi^2 - 4D_4\xi^3$$
$$C = D_1' - D_2'\xi + D_3'\xi^3 - D_4'\xi^4$$

where

$$D_1 = \sum_{i=1}^{4} [A_i/(i+1)] - 1$$

$$D_2 = \sum_{i=1}^{4} [2A_i/(i+2)] - 1$$

$$D_3 = \sum_{i=1}^{4} [2A_i/(i+4)] - (1/2)$$

$$D_4 = \sum_{i=1}^{4} [A_i/(i+5)] - (1/5)$$

and

$$\alpha = 0.06667A_1 + 0.02381A_2\xi^{-1} + 0.01072A_3\xi^{-2} + 0.00556A_4\xi^{-3}$$
$$\beta = -(0.13334A_1\xi^{-1} + 0.07143A_2\xi^{-2} + 0.04288A_3\xi^{-3} + 0.02780A_4\xi^{-4})$$
$$\gamma = 0.06667A_1' + 0.02381A_2'\xi^{-1} + 0.01072A_3'\xi^{-2} + 0.00556A_4'\xi^{-3}$$

The primes denote differentiation with respect to x. The B_i's of Eq. (6) have been introduced into these expressions numerically as indicated by Eq. (8).

REFERENCES

[1] Sears, W. R., *The Boundary Layer of Yawed Cylinders*, Journal of the Aeronautical Sciences, Vol. 15, No. 1, p. 49, January, 1948.

[2] Prandtl, L., *On Boundary Layers in Three-Dimensional Flow*, R. & T. No. 64, British M. A. P. Volkerode, May 1, 1946.

[3] Struminsky, V. V., *Glissement d'une aile dan un gaz visqueux compressible*, C. R. (Doklady) Acad. Sci. U.R.S.S. (N.S.) 54, 765–768, 1946.

[4] Jones, R. T., *Effects of Sweepback on Boundary Layer and Separation*, N.A.C.A. T.N. No. 1402, July, 1947.

[5] Prandtl, L., *The Mechanics of Viscous Fluids*, Division G of *Aerodynamic Theory* (Vol. III), W. F. Durand, Ed., especially pp. 108–111; Springer, Berlin, 1935.

[6] Goldstein, S., and others, *Modern Developments in Fluid Dynamics*, especially Vol. I, Chapt. IV, Paragraph 60; Oxford, 1938.

[7] Tetervin, N., *Boundary-Layer Momentum Equations for Three-Dimensional Flow*, N.A.C.A. T.N. No. 1479, October, 1947.

[8] Howarth, L., *The Theoretical Determination of the Lift Coefficient for a Thin Elliptic Cylinder*, Proc. Royal Soc. of London, Vol. 149A, p. 558, March–April, 1935.

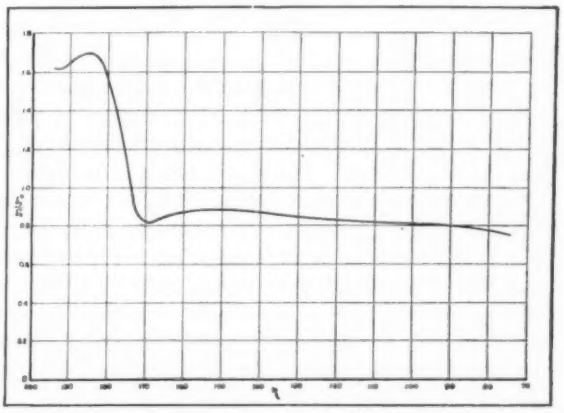

FIG. 6. Ratio of spanwise to chordwise boundary-layer displacement thicknesses.

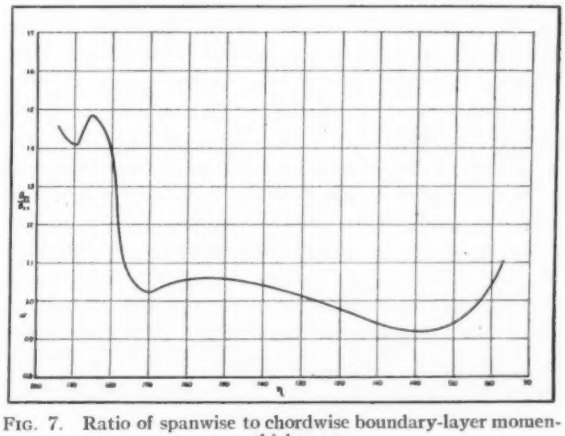

FIG. 7. Ratio of spanwise to chordwise boundary-layer momentum thicknesses.

Problems and Progress in Low-Pressures Research*

E. D. KANE† AND R. G. FOLSOM‡
University of California at Berkeley

ABSTRACT

The nature of the theoretical and experimental problems associated with the field of rarefied gas dynamics is discussed. The types of laboratory equipment judged to be most suitable for studying these problems are low-pressure supersonic wind tunnels, molecular beams, and rotating cylinders. Experimental results with a model wind tunnel and typical supersonic nozzles illustrate the existence of the expected large viscous effects and possible slip at the boundary. The techniques used and under development for pressure measurement and flow visualization are described.

INTRODUCTION

THE MECHANICS OF FLOW of a gas at low pressures, or rarefied gas dynamics, has reached the stage of engineering importance. The term "low pressures" is understood to mean low absolute pressures of 1 in. Hg or less. Subsonic gas flow in pipes under low-pressure conditions prevails in vacuum systems used in the preparation of vitamins, drugs, or in similar distillation processes. There is a fair body of theory and experimental information available for this type of flow. There are virtually no experimental data or adequate theoretical treatments available for supersonic flow in a rarefied gas (sometimes called "super-aerodynamics"), and it is the investigation of this field which is the primary purpose of the research program to be discussed. For the aeronautical engineer or the aerodynamicist, a knowledge of fluid mechanics as applied to the supersonic flow of a gas at low pressures is necessary to understand the problem of flight at extreme altitudes.

Applications of the available theory of gas dynamics to low-pressure phenomena are limited because the fluid cannot be described in terms of a continuum but must be discussed on the basis of the motion of individual molecules. A useful criterion in estimating the magnitude of low-pressure effects is the molecular mean free path, which can be defined approximately as a distance a molecule will travel, on the average, before it undergoes a collision with another molecule. When the pressure is high (or more properly speaking, the density), the individual molecules of gas are close together, and the mean free path is correspondingly small. When the pressure is decreased, the number of molecules per unit volume decreases, and the average distance that an individual molecule will travel before impact increases. In order to fix the magnitude of the mean free path quantitatively, Table 1 shows some values of molecular mean free path at different altitudes and pressures. For example, at an altitude of 75 miles the molecular mean free path is about 1 ft. At this altitude, the atmosphere can no longer be considered a continuum for an object with a characteristic dimension of 1 ft. If the characteristic dimension of the object was 1,000 ft., then the atmosphere might behave essentially like a continuum for that large object.

Elementary physical reasoning suggests that the ratio of mean free path divided by characteristic dimension (L/D) provides one important parameter to describe the magnitude of low-pressure effects. As discussed by Tsien,[1] this L/D ratio is proportional to the ratio Ma/Re, the constant of proportionality being roughly 1.5. The question of how large the L/D or Ma/Re number ratio must become before the methods of continuum fluid mechanics begin to require correction is not clear. Based on theoretical and experimental considerations for subsonic flow in a pipe, the ordinary gas dynamics theory requires correction when the L/D ratio becomes larger than about 0.001. Schamberg[2] estimates that if L/D is 0.005, the skin friction coefficient for a flat plate moving at a Mach Number of 3, decreases by 10 per cent from the value predicted by ordinary gas dynamics theory.

As pointed out by Tsien,[1] each phase of the non-continuum flow problem can be subdivided logically into three parts, depending on the magnitude of the pressure. For appreciable but small mean free paths, called the slip region, ordinary gas dynamics begins to fail. For mean free paths that are large compared to the body dimensions (L/D large), collisions of a molecule with a surface are much more frequent than collisions with other molecules. This region might be termed "fully developed" molecular flow. There is a transition region where the frequency of collisions with a wall and collisions with other molecules is of the same order of magnitude. Analytical treatment of these three regions may well require three kinds of theoretical development. Large gaps exist at present

Presented at the Heat Transfer and Fluid Mechanics Institute, Los Angeles, June 21–23, 1948. Received July 6, 1948.

* This work is being done under Office of Naval Research Contract No. N7-ONR-295-Task 3 with the Department of Engineering, University of California, Berkeley, Calif.

† Research Engineer, Department of Engineering.

‡ Professor of Mechanical Engineering.

TABLE 1

Molecular Mean Free Path for "Adopted Atmosphere" and for Room Temperatures

Pressure		"Adopted Atmosphere"*				
		Altitude		Temperature,	Mean Free	Mean Free Path at 70°F., Ft.
Mm. Hg	Lbs. per sq.ft.	Miles	Ft. × 10^{-5}	°F.	Path, Ft.	
760	2,110	0	0	70	3.1×10^{-7}	3.1×10^{-7}
180	500	6.6	0.35	−70	1.0×10^{-6}	1.3×10^{-6}
7.9	22	19	1.0	−70	2.5×10^{-5}	3.0×10^{-5}
0.57	1.6	32	1.7	170	5.0×10^{-4}	4.1×10^{-4}
2.7×10^{-2}	0.075	49	2.6	−30	7.5×10^{-3}	8.7×10^{-3}
3.6×10^{-4}	0.99×10^{-3}	76	4.0	220	1	0.66
6.5×10^{-6}	1.8×10^{-5}	114	6.0	760	90	36
5.0×10^{-7}	1.4×10^{-6}	152	8.0	1,300	1,500	460

* Values from *AAF Technical Report 5632*, "A Design Manual for Determining the Thermal Characteristics of High Speed Aircraft" Chapt. III, 1947.

in portions of the theory and particularly in experimental information.

The Boundary Layer

Shortly after 1900, Prandtl introduced the modern concept of flow of real fluids, pointing out that the flow of a real fluid of small viscosity differs from an ideal fluid only in the region near a solid surface (the boundary layer). In this region, the frictional effects are appreciable, and the fluid undergoes a loss of momentum related to the frictional force at the surface. The general character of the boundary layer is indicated normally by the magnitude of Reynolds Number. At low pressures the boundary layer is laminar, since Reynolds Number becomes small because of the decrease in density. Solutions have been developed for laminar flow over a smooth flat plate with zero pressure gradient in the direction of flow. The boundary-layer thickness δ becomes

$$\delta = (\text{constant})(x\nu/u)^{1/2} \tag{1}$$

where

x = distance from leading edge of plate
ν = kinematic viscosity of fluid
u = free-stream velocity of fluid relative to plate

The constant is estimated from 1.7 to 8, depending on the assumptions as to compressibility, the exact definition of δ, etc. In order of magnitude, Eq. (1) can be written

$$\delta = 5\sqrt{x\nu/u} \tag{2}$$

Dividing by a characteristic linear dimension D gives

$$\delta/D = 5Re_D^{-1/2}\sqrt{x/D} \tag{3}$$

For $\delta/D = 1/2$, let $x = x_0$ in Eq. (3) and solve for x_0.

$$x_0/D = Re_D \times 10^{-2} \tag{4}$$

If D is the diameter of a nozzle and $Re_D = 100$, Eq. (4) indicates that the boundary layer may be expected to fill the nozzle when the nozzle length equals the nozzle diameter. Reynolds Numbers of this order are possible in small nozzles at low pressures, and it is apparent that viscous effects become important to flow geometry at low pressures.

When mean free paths are large, experiments show that another effect occurs which modifies Eqs. (1) to (4). One of the boundary conditions used in deriving Eq. (1) was that the fluid velocity at a solid surface is zero. Low-pressure flow experiments in pipes indicate that a finite "slip" velocity occurs at a solid boundary, resulting in a change of the velocity distribution from the surface out to the free stream. The "slip" is a surface phenomenon, but, unlike the boundary layer, its character is determined by the nature of molecular interactions at the surface rather than by the viscous characteristics of the fluid. Information regarding reflection (specular or diffuse) and accommodation coefficients becomes of primary importance. A solution for flow over a flat plate may be obtained under the assumption that the velocity distribution function remains the same as in laminar flow, except that a discontinuity occurs at the boundary. This solution gives an asymptotic expression for "boundary-layer" thickness as

$$\delta/x \sim L/x \text{ for } L/x > 1/Ma \tag{5}$$

where L = molecular mean free path, Ma = Mach Number and the other quantities were defined previously. Eq. (5) indicates that at low pressures the boundary-layer thickness becomes independent of Reynolds Number, a result quite different from Eq. (1).

Present estimates of the magnitude of L/D for the "slip" region depend on experiments in pipes where no curvature, small pressure gradients, and no shocks exist. Preliminary experiments with nozzles indicate that "slip" may occur at smaller L/D values. Similar results might be expected with airfoils when curvature and pressure gradients are appreciable.

In supersonic flow the nature of the shock wave and shock patterns are important. The shock wave is thin at normal pressures, although elementary considerations would indicate that the minimum thickness is probably several molecular mean free paths. As the density decreases, the shock-wave thickness must increase and the usual concept of the shock as a discontinuity no longer holds. The interactions of a

shock region at low pressures with a laminar boundary layer that is partly subsonic and partly supersonic are complex.

Possible Types of Experimental Equipment

With the problem of fluid flow at low pressures roughly defined, the question of suitable types of laboratory equipment for experimental investigations arises. In general, studies may be made on objects moved through stationary air or on stationary objects placed in an air stream. Special equipment will be necessary to study the details of the boundary phenomena.

(1) *Flight Testing*

Certain types of flow data may be obtained from recording or telemetering instruments carried by a rocket into the upper atmosphere as in the experiments being conducted with the V-2 at White Sands.[3] The highest altitudes reached have been in the order of 115 miles.

(2) *Towing the Model*

Since large volumes at low pressure are achieved easily with modern vacuum pumps and design techniques, it is reasonable to consider sending a model through such an atmosphere. A firing chamber (of the type available at Aberdeen Proving Ground) could be adapted for this purpose. A variation of this idea is to attach a model to the end of a rotating arm that rotates at high speeds in a minimum-sized tank. The major difficulty with these schemes is instrumentation. Drag forces at low pressures are small, and a fast recording of pressure readings is difficult at low pressures.

(3) *Low-Pressure Wind Tunnel*

A conventional supersonic wind tunnel with modifications designed to give low-pressure high-speed flow is an attractive possibility for studies in the "slip" region. The flow about different stationary models can be studied conveniently. The instrumentation problems are simplified, and the operating conditions are under the control of the investigators.

(4) *Molecular Beam*

A molecular beam (of the type used for atomic and nuclear studies) provides a uniform stream of molecules suitable for studies of molecular interaction with surfaces at extremely low pressures. Information on reflection and accommodation coefficients may be obtained for controlled conditions at a given surface.

(5) *Rotating Cylinder*

Tsien[1] suggested that an extension of Millikan's rotating cylinder experiments to high speeds would provide fundamental information on "slip" flows. Preliminary design studies have indicated that with suitable geometry the whole range of molecular flow phenomena, from "slip" through "fully developed molecular flow" could be obtained with this type of equipment.

Instrumentation Problems

In considering the use of experimental equipment to investigate low-pressure problems, the question of suitable instrumentation is important. Static or impact pressures can be measured with an appropriate type of low-pressure gage.[4] In dealing with gas-flow problems, it is necessary that at least one other property of the gas be measured. Temperature is a possibility, but the difficulties in measuring local temperatures are great. Direct measurement of density seems to be a more attractive possibility, particularly if the means used to obtain quantitative density measurements can also be used to show visually the nature of the flow pattern.

(1) *Pressure Measurements*

If pressures at a wall tap or from an impact tube are to be obtained under low-pressure conditions, it is necessary to choose the dimensions of the system with care if impractically long response times are to be avoided.[5] Fig. 1 illustrates a typical gaging system

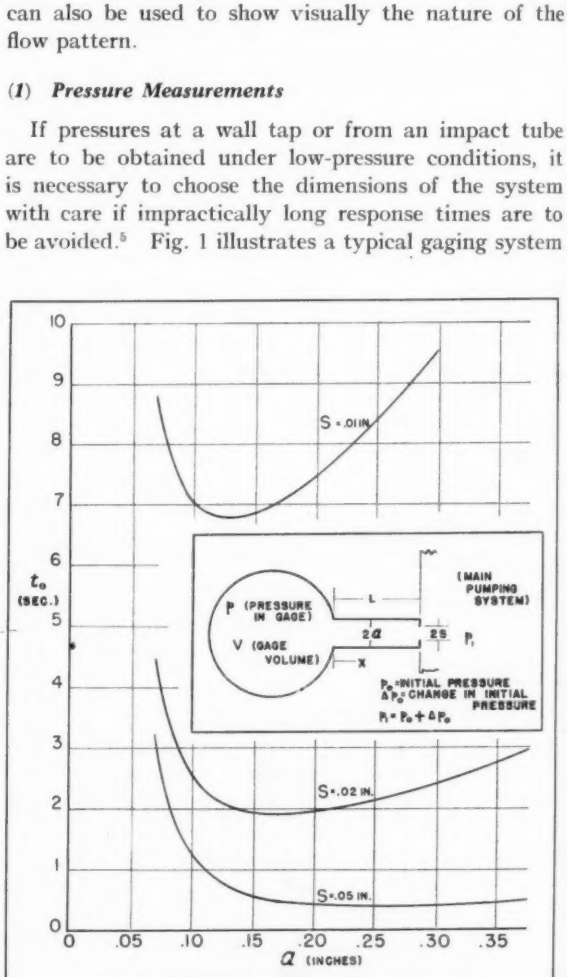

FIG. 1 - RESPONSE TIME CHARACTERISTICS FOR A SELECTED SYSTEM V = 2 IN.^{3} L = 5 IN. T = 530° R

idealized as an orifice (wall tap), connecting line, and gage tube volume. The curves indicate the effect of geometry on the time required to reach equilibrium after the system pressure is changed. Response times in the order of hours are easily possible with improper designs.

The meaning of an impact tube reading when the mean free path is of the same order as the tube diameter is a problem under investigation. A theoretical analysis has been developed and an experimental check will be made.

Three basic types of pressure gages are being used on wind tunnel measurements. The McLeod gage[4] is the standard, and its use is limited to secondary gage calibration. It can be constructed to cover almost any low-pressure range, but considerable time is required to obtain a reading. A precision U-tube manometer, filled with butyl phthalate mixed with low vapor pressure oil to give a convenient specific gravity at 70°F., is used for pressures over 500 microns (0.5 mm.) and up to about 6 mm. of Hg. The Pirani gage[4] is useful over a pressure range from 1 to 500 microns of Hg. In the Pirani gage, the temperature of a hot wire is a function of the pressure. Normally, two Pirani tubes are provided, one of which is sealed off at a definite pressure and placed in one leg of the bridge circuit, while the other is connected to the system. If the two tubes are maintained at the same temperature, the effect of atmospheric temperature variations is essentially canceled out. An indicating and recording system capable of giving the readings of 16 gages simultaneously has been developed.

Probably the most difficult problem of pressure measurement is the detection system of the molecular beam. With a background pressure of 5×10^{-6} mm. Hg, it will be necessary to detect a pressure differential of 10^{-11} mm. Hg. The first development in this direction uses ion gages (triode tubes in which pressure changes produce changes in plate current), one tube being used to probe the beam, while the other registers background pressure. Pressure differences of 5×10^{-9} mm. Hg have been measured with present equipment.

(2) *Flow Visualization*

For ordinary wind-tunnel work the shadowgraph, Schlieren, and interferometer techniques are used to visualize the flow. These light refraction methods are subject to decreased sensitivity as the fluid density decreases. At the lower pressures (less than 1 mm. of Hg abs.) these methods can no longer be employed in small wind tunnels.

In attempting to develop new methods of flow visualization, consideration has been given to the property of molecules for absorption of radiation of given wave lengths or emission of radiation when properly excited.[6] Typical possibilities are exhibited by oxygen, which

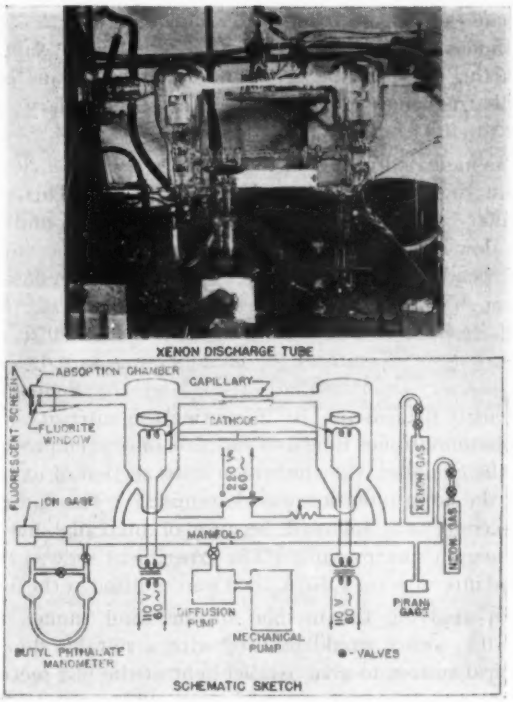

FIG. 2. Xenon tube (schematic sketch combined with photograph).

has a strong absorption band at a wave length of about 1,470Å.; by mercury vapor with a strong absorption band at 2,537Å.; and by ozone, which has its maximum absorption at about 2,537Å. Preliminary investigations have shown that flow visualization is possible for a limited range of low pressures with any of these gases. In general, three problems are involved:

(1) The generation of monochromatic light of the proper wave length.

(2) The production and introduction of the gas or vapor.

(3) Detection of the radiation passing through and absorbed partially by the gas.

Preliminary work with the mercury vapor absorption flow visualization process indicates expected difficulties connected with low vapor pressure of mercury and the proper interpretation of measurements because of the reactions of the relatively heavy mercury molecule. The quantities of ozone required for reasonable sensitivity with an ozone absorption method are of such magnitude that ozone generation and storage become a major problem. Ozone in liquid form is unstable and highly explosive. The oxygen absorption flow visualization method appears to offer the best possibilities.

The oxygen absorption method has been studied in detail. A hot cathode discharge tube with a Xenon atmosphere has been developed for the production of light of the required 1,470Å. wave length. Details

of an experimental lamp are shown in Fig. 2. The cathodes are fed from a 220-volt, 60-cycle supply. Starting of the tube is accomplished by means of a radio-frequency (27.4 mc.) field at the capillary (approximately $^1/_4$ in. I.D.) of the tube.

As indicated in Fig. 2, the capillary section is viewed from the end through a fluorite window. This particular tube was provided with a chamber around the window in which the oxygen pressure could be varied independently of the tube pressure. Radiation passing through the fluorite window excited fluorescent material coated on a second window in the chamber. If the oxygen pressure in the chamber was raised, some of the radiation was absorbed, and the fluorescent intensity decreased. By measuring this intensity with a photomultiplier tube as a function of oxygen pressure in the chamber, the absorption cross section of oxygen for the lamp radiation was determined. This indirect procedure was followed because of unavailability of a vacuum spectrograph. The experiment showed that good intensities of 1,470Å. light were emitted by the tube.

In applying the method to the wind tunnel, the 1,470Å. source would be used with a suitable fluorite optical system to give parallel light at the test section. Light traversing the test section would be absorbed by an amount depending on the path length and density, giving a nonuniform light distribution at exit from the test section. The changes in intensity over the test section would then be detected by photographic films, observations of a fluorescent screen, or equivalent means. To indicate the magnitude of the effect, for a 2 to 1 density ratio, a change in 1,470Å. intensity of 50 per cent is expected at 100 microns of mercury if the gas is 100 per cent oxygen. If air is used, the intensity change will be about 10 per cent.

When properly excited, nitrogen produces a radiation that persists after the excitation has been removed. This afterglow phenomenon, being explored by Prof. J. Kaplan, may provide a practical method for flow visualization at low pressures.

Low-Pressure Supersonic Wind Tunnels

The development of wind tunnels at Berkeley for low-pressure supersonic flow considers only the continuous operating, nonreturn, open, or closed throat type of tunnel. Three sizes of tunnels are under investigation, the smaller units being limited in usefulness but more economical to operate. Preliminary investigations with the smaller units have proved necessary in determining the performance and geometry of the largest tunnel.

The smallest tunnel[7] has a 1- by $^3/_8$-in. rectangular test section operating at a pressure of 1 in. Hg abs. at $M = 2.4$. A single-stage steam ejector exhausting to the atmosphere provides the driving energy. This tunnel will not operate at pressures low enough to show molecular flow effects. Preliminary work has been completed, and the unit now provides equipment suitable for many student tests.

The largest tunnel now under construction will have a test section of about 150 sq.in. in area and will be suitable for tests on models with a characteristic dimension of about 1 in. The pumping system is based on a five-stage steam ejector[7] selected on the basis of economic operation and flexibility of performance.

The medium tunnel was built with a 1- by 1-in. test section to permit experimentation on nozzle and diffuser design on an economical scale and to provide a suitable means for developing instrumentation for low-pressure conditions. The general arrangement of the tunnel is shown in Fig. 3. Tracing the flow cycle of gas through the tunnel, atmospheric air is passed through a dryer, flow rate meters, a needle valve, and into a settling chamber or reservoir where stagnation pressure and temperature can be measured. The gas then passes through a supersonic nozzle to the test section; then through a diffuser into a large ballast tank, the purpose of which is to damp out high-frequency fluctuations in the pumping system performance; and then into the first-stage vacuum pump. This pump raises the gas pressure to the range of 200 to 3,000 microns of Hg, depending on operating conditions. The gas is raised to atmospheric pressure and discharged by a second pump of the mechanical positive displacement type.

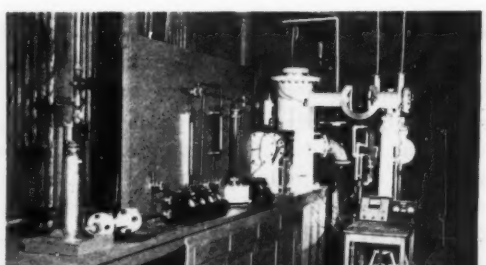

NO. 2 WIND TUNNEL

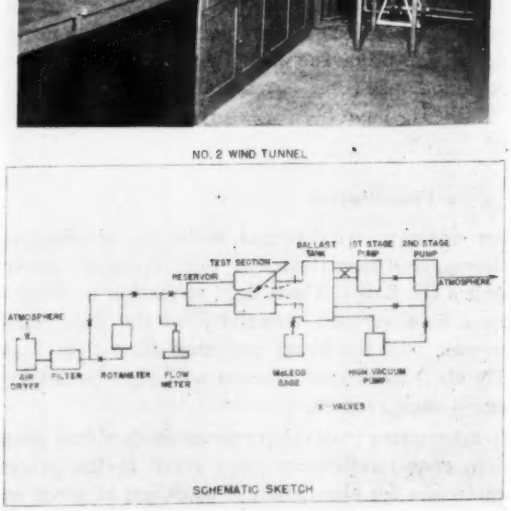

SCHEMATIC SKETCH

Fig. 3. No. 2 wind tunnel (schematic sketch combined with photograph).

It will be noted from Fig. 3 that a high vacuum pump (capable of producing pressures of about 10^{-6} mm. of Hg abs.) is connected to the ballast tank. This pump is useful for calibrating the pressure gages without removing them from the tunnel. The calibration standard is a McLeod gage.

To start the tunnel, the inlet needle valve and downstream valve are closed, and the mechanical pump is connected directly to the wind tunnel. When no leaks exist this pump will bring the pressure in the tunnel from atmospheric down to about 0.75 mm. Hg in 3 min. The pump is then closed off from the tunnel, the downstream valve is opened, and the fore pump in series with the mechanical pump brings the pressure down to less than 5 microns of Hg in about 2 min. Then the inlet valve is opened sufficiently to give the desired rate of gas flow through the tunnel. Control of tunnel operating conditions is obtainable by adjusting one or more of the following variables: (a) inlet valve position, (b) downstream valve position, and (c) pump performance.

The volumetric and weight rate of flow obtainable with the first-stage pump at a given intake pressure can be varied by changing the power input to the pump. This high vacuum pump is a commercial oil jet unit, using a low vapor pressure oil that is vaporized in a boiler and expanded through a supersonic nozzle to give a pumping action analogous to that of a steam jet ejector or water jet pump. Approximately constant volumetric flow rate can be obtained with this unit over a pressure range from about 70 to 300 microns of Hg.

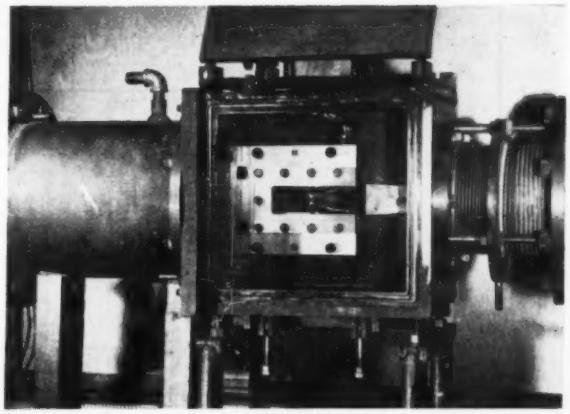

FIG. 4. Photograph of nozzle in No. 2 wind tunnel.

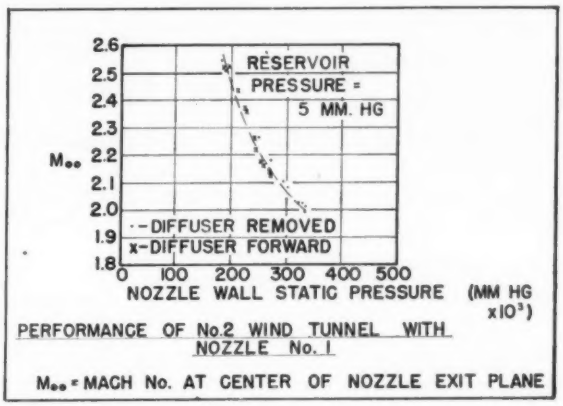

FIG. 5.

PRELIMINARY EXPERIMENTAL RESULTS

(1) *Diffuser Performance*

The viscous effects at low pressures make the problem of diffuser design for pressure recovery difficult.[8] It is probable that large pressure ratios, of the magnitude obtainable in supersonic tunnels operating at normal pressures, cannot be achieved in a wind tunnel for low-pressure testing. Tests were run with the diffuser shown in Fig. 4 in position in the tunnel. The position of the diffuser along the axis of the tunnel was adjustable in the range from about $\frac{1}{8}$ to 2 in. from the end of the nozzle. With this particular diffuser the ratio of ballast tank pressure to nozzle static pressure was about 1.3 with the diffuser in place as compared to 1.1 with no diffuser. Because of the small gain in tunnel performance achieved in this diffuser, it has not been used for regular test work. Development of a possibly better diffuser has not been considered of major importance at this time.

(2) *Wind-Tunnel Performance*

The performance of the wind tunnel with a particular nozzle is shown in Fig. 5. These data were obtained by setting the inlet valve to give a constant reservoir or supply pressure to the nozzle of 5 mm. of Hg. The downstream valve was used to throttle the flow and control the test chamber and ballast tank pressures. Impact tube pressures were read at the center of the exit plane of the nozzle and were combined with static pressures read at the nozzle wall to calculate the apparent Mach number, M_∞.

The first effect noticed when operating the tunnel was that, in closing the downstream valve, the pressure in the test section as measured at the nozzle wall tap immediately began to increase. This phenomenon was contrary to what would be expected in a supersonic wind tunnel operating at normal pressures, where the effect of downstream changes is not apparent at the test section until a shock pattern has been moved forward into that section. The tentative explanation is that the thick boundary layers existing in the tunnel permit transmission of downstream effects to the upstream portions of the nozzle through fluid which is at subsonic velocities.

Using the one-dimensional nonviscous compressible flow theory, a constant Mach Number = 4 would be

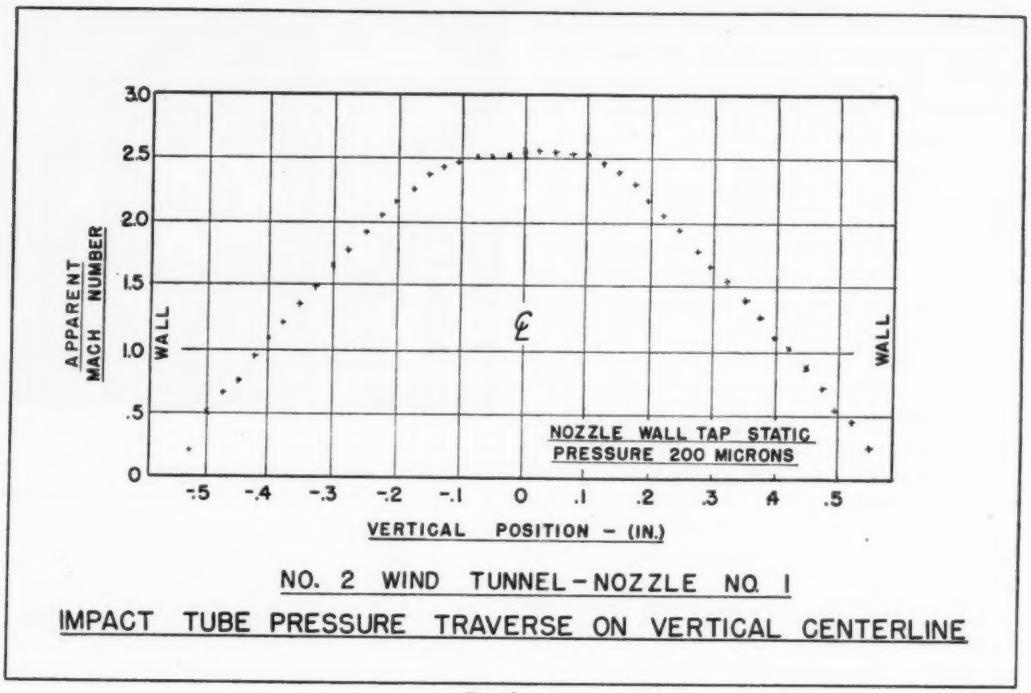
APPARENT MACH NUMBER
3.0
2.5
2.0
1.5
1.0
.5
0
WALL
WALL
NOZZLE WALL TAP STATIC PRESSURE 200 MICRONS
-.5 -.4 -.3 -.2 -.1 0 .1 .2 .3 .4 .5
VERTICAL POSITION — (IN.)
NO. 2 WIND TUNNEL - NOZZLE NO. 1
IMPACT TUBE PRESSURE TRAVERSE ON VERTICAL CENTERLINE

FIG. 6.

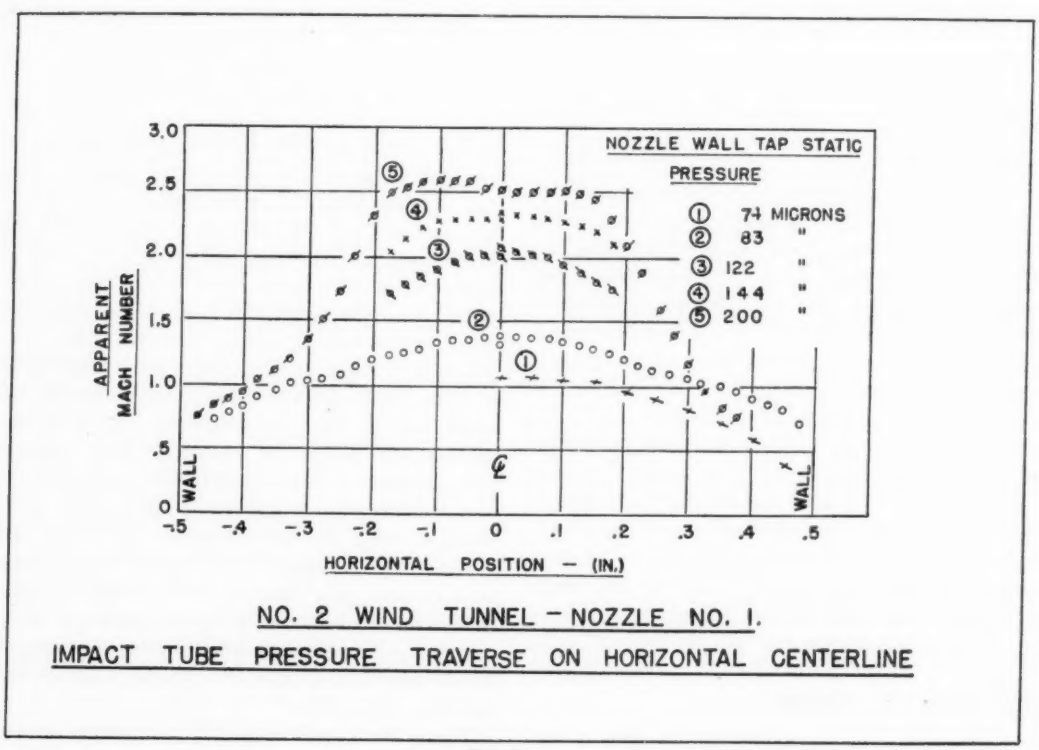
APPARENT MACH NUMBER
3.0
2.5
2.0
1.5
1.0
.5
0
WALL
WALL
NOZZLE WALL TAP STATIC PRESSURE
① 74 MICRONS
② 83 "
③ 122 "
④ 144 "
⑤ 200 "
-.5 -.4 -.3 -.2 -.1 0 .1 .2 .3 .4 .5
HORIZONTAL POSITION — (IN.)
NO. 2 WIND TUNNEL - NOZZLE NO. 1.
IMPACT TUBE PRESSURE TRAVERSE ON HORIZONTAL CENTERLINE

FIG. 7.

expected with this nozzle. From Fig. 5, the maximum value of M_∞ for the given reservoir pressure (with the downstream valve open) was about 2.55. It is characteristic of the operation of this low-density wind tunnel that the Mach Number obtainable depends on the effective sectional area of the nozzle as influenced by the boundary-layer thickness.

(3) *Nozzle Performance*

Using an impact tube (0.027 in. I.D. and 0.047 in. O.D.), pressure distributions were obtained at a plane $^1/_8$ in. upstream from the exit plane of a rectangular nozzle (designed in the diverging portion by the method of characteristics for $M = 4$ with no correction for boundary-layer thickness). The results are expressed in terms of an apparent Mach Number determined by the usual Rayleigh formula, using the static pressure measured at a pressure tap at the plane of the impact tube in a diverging wall of the nozzle. In all tests the diffuser was removed, and the control of the pressure was by means of the tunnel inlet valve. Theoretical and experimental work indicate the apparent Mach Number as used is fictitious because of static pressure variation in the test section and the influence of large molecular mean free path. The experimental data are presented in this form for convenience. Additional work is in progress to determine the magnitude of the corrections that should be applied.

A typical impact pressure distribution along the vertical axis (between diverging walls) is shown in Fig. 6. The characteristic thick boundary layers and lack of slip at the walls are noticeable. All plotted data are uncorrected, and the apparent shift in values at the centerline axis is due to experimental runs in each half of the nozzle being made on different days with slightly different adjustments of the tunnel. Fig. 7 shows similar data for the horizontal axis at a series of static pressures. These data indicate the possibility of slip at the parallel walls of the nozzle. For small openings of the inlet valve, the pressure is low and the Mach Number is correspondingly low, and the distribution is characteristic of what might be expected for laminar flow at subsonic speeds. As the inlet valve opening is increased, the pressure rises, the Mach Number increases, and a uniform velocity section appears at the center of the nozzle, becoming about 25 per cent of the cross section at an indicated static pressure of 200 microns. The presence of a thick boundary layer and large viscous effects is demonstrated.

The major problem in designing a supersonic wind tunnel for low-pressure studies is to determine the type of nozzle that will give optimum velocity distribution. Shortening the nozzle length in the flow direction in an attempt to reduce boundary-layer build-up is one obvious approach that is now being examined both experimentally and theoretically. The boundary-layer thicknesses indicated (Figs. 6 and 7) may be due partially to separation effects. Before constructing the nozzle with the abrupt converging section shown in Fig. 4, unpublished tests were run with various geometries. Oil was used at velocities to give the Reynolds Number range encountered in the wind tunnel, and velocity distributions were obtained at each nozzle throat. These tests with oil showed that the abrupt approach section used in the wind tunnel supersonic nozzle gave a uniform velocity distribution at the throat with minimum boundary-layer thickness. Additional evidence of satisfactory operation was available from performance of similar sharp entrance nozzles used in the Kochel wind tunnel. It is possible that shocks occurring in the supersonic portion of the nozzle would cause thickening of the boundary layer observed near the nozzle exit.

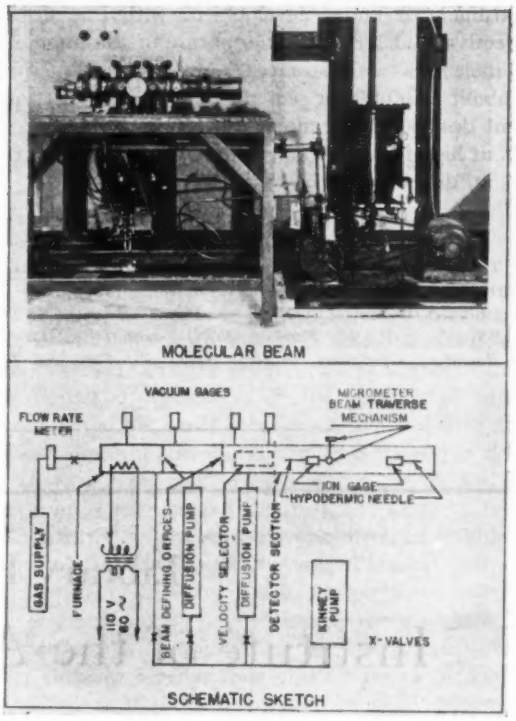

FIG. 8. Molecular beam (schematic sketch combined with photograph).

MOLECULAR BEAM

Molecular beam equipment (Fig. 8) is being tested at Berkeley. The source of high-speed molecules is a small furnace with an opening in one end through which molecules can escape into an evacuated chamber. This "beam" of molecules is collimated with slits to give a cone of molecules traveling with a range of speeds. A velocity selector can be used to pass only molecules having speeds within a predetermined range. The

instrument is under development with the ultimate objective of determining the nature of the interaction of molecules with surfaces. Molecular (N_2) speeds of about 1,600 ft. per sec. are used currently in equipment designed for a maximum of about 3,500 ft. per sec. at high furnace temperatures. The beam is about $^3/_{16}$ in. diameter at the "model."

References

[1] Tsien, H. S., *Superaerodynamics, Mechanics of Rarefied Gases*, Journal of the Aeronautical Sciences, Vol. 13, No. 12, pp. 643–664, December, 1946.

[2] Schamberg, R., *The Fundamental Differential Equations and the Boundary Conditions for High Speed Slip-Flow and Their Application to Several Specific Problems*, p. 7; Thesis, California Institute of Technology, May, 1947.

[3] "Life" Magazine, Vol. 20, No. 21, pp. 31–35, May 27, 1946.

[4] Strong, John, *Procedures in Experimental Physics*, 1st Ed., pp. 43–151; Prentice-Hall Inc., New York, 1946.

[5] Schaaf, S. A., and Cyr, R. R., *Time Constants for Vacuum Gage Systems*, Report HE-150-42, University of California, March, 1948.

[6] Evans, R. A., *Flow Visualization at Low Pressures*, Report HE-150-25, University of California, September, 1948.

[7] Folsom, R. G., and Kane, E. D., *Steam Jet Drive for Small Low Pressure Wind Tunnels*, Report HE-150-9, University of California, June, 1947.

[8] Tsien, H. S., *Wind-Tunnel Testing Problems in Superaerodynamics*, Journal of the Aeronautical Sciences, Vol. 15, No. 10, pp. 573–580, October, 1948.

Library Facilities of the
Institute of the Aeronautical Sciences

To serve Institute members and others in the aeronautical industry, the Institute of the Aeronautical Sciences offers the facilities of:

The W. A. M. Burden Library
2 East 64th Street
New York 21, N.Y.

The facilities of this library are available for reference study at the Institute.

The Paul Kollsman Lending Library
2 East 64th Street
New York 21, N.Y.

This library loans books without charge to members and others in the United States over eighteen years of age. Full information will be sent on request.

The Pacific Aeronautical Library
6715 Hollywood Boulevard
Los Angeles 28, Calif.

This is a service and reference library for West Coast members and organizations. Full information as to its facilities will be sent on request.

Airfoils in Slightly Supersonic Flow*

HSUE-SHEN TSIEN† AND JUDSON R. BARON‡
Massachusetts Institute of Technology

SUMMARY

An investigation is made to determine the performance of simple thin airfoils in the slightly supersonic flow region with the aid of the nonlinear transonic theory first developed by von Kármán.[1] Expressions for the pressure coefficient across an oblique shock and a Prandtl-Meyer expansion are developed in terms of a transonic similarity parameter. Aerodynamic coefficients are calculated in similarity form for the flat plate and asymmetric wedge airfoils, and curves are plotted. Sample curves for a flat plate and a specific asymmetric wedge are plotted on the usual coordinate grid of C_l, C_d, and $C_{m_{c/4}}$ versus angle of attack and C_l versus Mach Number to illustrate the apparent features of nonlinear flow.

INTRODUCTION

RECENTLY, THEODORE VON KÁRMÁN[1] has derived a set of similarity rules for flows around slender bodies in a stream having close to sonic velocity. He called this set of rules the transonic similarity rules. Essentially, the results are as follows: If δ is the thickness ratio of the body, α the angle of attack of the airfoil, C_l, C_d, C_m the sectional lift, drag, and moment coefficients, respectively, then

$$C_l(\alpha/\delta) = (\delta^{5/3}/\Gamma^{1/3})L(K) \tag{1}$$

$$C_d(\alpha/\delta) = (\delta^{5/3}/\Gamma^{1/3})D(K) \tag{2}$$

and

$$C_m(\alpha/\delta) = (\delta^{5/3}/\Gamma^{1/3})M(K) \tag{3}$$

In these equations, K is the similarity parameter defined as

$$K = (1/2)[(M^{0\,2} - 1)/(\Gamma\delta)^{2/3}] \tag{4}$$

where M^0 is the free stream Mach Number and Γ is a parameter of the property of the fluid—i.e.,

$$\Gamma = (\gamma + 1)/2 \tag{5}$$

where γ is the ratio of the specific heats of the gas. Furthermore, if ξ is a nondimensional parameter, such as percentage of chord, designating a surface point on the airfoil, then the pressure coefficient, C_p, at that point is given by

$$C_p = \frac{p - p^0}{(1/2)\rho^0 U^2} = \frac{\delta^{2/3}}{\Gamma^{1/3}}\,p(K;\ \xi) \tag{6}$$

The appropriate differential equation for such transonic flows is, however, nonlinear and, in general, difficult to solve. For the special case of slightly supersonic flow, the problem is, on the other hand, much simpler, since the exact solutions associated with this problem, the oblique shock and Prandtl-Meyer flow, are known. The task is then simply to reduce the exact solutions to forms that are appropriate to transonic conditions involving the parameter K. This is indeed already indicated by von Kármán[1] himself. The purpose of this paper is to complete the calculations of von Kármán, to render them more systematic, and then, finally, to apply these results to calculate the rather peculiar aerodynamic characteristics of simple thin airfoils in slightly supersonic flow with shocks attached to the leading edge.

OBLIQUE SHOCK

Let β be the shock angle—i.e., the angle between the free stream and the shock front—and let θ be the angle through which the flow is deflected. The basic oblique shock relations[2] are then

$$\frac{p}{p^0} = \frac{2\gamma}{\gamma + 1}\,M^{0\,2}\sin^2\beta - \frac{\gamma - 1}{\gamma + 1} \tag{7}$$

and

$$\frac{\tan(\beta - \theta)}{\tan\beta} = \frac{\gamma - 1}{\gamma + 1} + \frac{2}{\gamma + 1}\,\frac{1}{M^{0\,2}\sin^2\beta} \tag{8}$$

On the other hand, the pressure coefficient C_p for a point on the surface is given by

$$C_p = (2/\gamma M^{0\,2})[(p/p^0) - 1] \tag{9}$$

In the three equations, Eqs. (7), (8), and (9), the two quantities β and (p/p^0) can be eliminated. The resultant relation is

$$\tan\theta\left(1 - \frac{C_p}{2}\right)\left(\frac{\Gamma C_p}{2} + \frac{1}{M^{0\,2}}\right)^{1/3} = \frac{C_p}{2}\left[1 - \left(\frac{\Gamma C_p}{2} + \frac{1}{M^{0\,2}}\right)\right]^{1/3} \tag{10}$$

Eq. (10) is the exact oblique shock relation. For the transonic conditions, θ is small and is equivalent to δ in von Kármán's formulas. Thus

$$K = (1/2)[(M^{0\,2} - 1)/(\Gamma\theta)^{2/3}] \tag{11}$$

Received September 18, 1948.

* This paper is based on a thesis by J. R. Baron, under the direction of the senior author, submitted to the Graduate School in partial fulfillment of the requirements for the degree of Master of Science in Aeronautical Engineering at Massachusetts Institute of Technology.

† Professor of Aerodynamics.

‡ Research Aerodynamicist, Supersonic Laboratory.

From this equation the free stream Mach Number, M^0, can be expressed in terms of K and θ. In fact,

$$1/M^{0\,2} = 1 - 2K(\Gamma\theta)^{2/3} + \ldots \tag{12}$$

The appropriate form for the pressure coefficient is

$$C_p = (\theta^{2/3}/\Gamma^{1/3})p^{(1)}(K) \tag{13}$$

where $p^{(1)}$ is the pressure function associated with the flow after the oblique shock. Then Eqs. (12) and (13) can be substituted into the general relation, Eq. (10), and, by taking only the lowest order of terms, an expression for $p^{(1)}$ is obtained:

$$1 = (p^{(1)2}/4)[2K - (p^{(1)}/2)] \tag{14}$$

Eq. (14) is a cubic equation for $p^{(1)}$. To solve this equation, it is convenient to put

$$f = 2/p^{(1)} \tag{15}$$

Then Eq. (14) is converted into the normal form of cubic equations,

$$f^3 - 2Kf + 1 = 0 \tag{16}$$

According to standard solutions,[3] the character of the roots of this cubic equation is dependent upon whether

$$(1/4) - (8/27)K^3$$

is greater than, equal to, or smaller than zero. In the first case, there will be one real root and two complex conjugate roots. The complex roots have, of course, no physical significance and need not be considered further. However, the single root is negative, as can be seen from Eq. (16) by making K extremely small. Negative f means negative $p^{(1)}$. But physically the flow is compressed by the shock, and thus $p^{(1)}$ must be positive. Therefore, no useful solution exists for

$$(1/4) - [(8/27)K^3] > 0$$

When K is equal to the critical value K^* such that

TABLE 1

Pressure Function for Weak Oblique Shock, $p_1^{(1)}$, Strong Oblique Shock, $p_2^{(1)}$, Prandtl-Meyer Expansion, $p^{(2)}$, and the Ratio of $(M^2 - 1)/(M^{0\,2} - 1)$ for Various Values of K. [Eqs. (19), (20), (29), and (36)]

K	$p_1^{(1)}$	$p_2^{(1)}$	$\left(\frac{M^2-1}{M^{0\,2}-1}\right)_1^{(1)}$	$p^{(2)}$	$\left(\frac{M^2-1}{M^{0\,2}-1}\right)^{(2)}$
0.00	....	....	....	2.0801	∞
0.20	....	....	....	1.7956	5.4891
0.40	....	....	....	1.5989	2.9987
0.60	....	....	....	1.4503	2.2086
0.80	....	....	....	1.3333	1.8333
0.945	2.5028	2.5358	....	1.2629	1.6682
0.975	2.1199	3.0252	....	1.2495	1.6408
1.00	1.9993	3.2780	0.0000	1.2387	1.6193
1.25	1.5149	4.6243	0.3941	1.1430	1.4572
1.50	1.3051	5.7574	0.5650	1.0651	1.3550
1.75	1.1714	6.8199	0.6653	1.0006	1.2859
2.00	1.0773	7.8295	0.7307	0.9461	1.2365
2.50	0.9393	9.9069	0.8122	0.8586	1.1717
3.00	0.8487	11.9204	0.8586	0.7909	1.1318
4.00	0.7235	15.9490	0.9096	0.6923	1.0865
5.00	0.6428	19.6155	0.9357	0.6228	1.0623
6.00	0.5844	23.8720	0.9513	0.5705	1.0475
8.00	0.5038	32.3625	0.9685	0.4962	1.0310
10.00	0.4496	40.3388	0.9775	0.4448	1.0222
13.00	0.3936	53.0786	0.9849	0.3905	1.0150
20.00	0.3168	78.4920	0.9921	0.3156	1.0079
30.00	0.2584	127.7466	0.9957	0.2574	1.0043
50.00	0.2001	199.0446	0.9980	0.2000	1.0020
80.00	0.1581	472.1435	0.9990	0.1584	1.0010
100.00	0.1414	∞	0.9993	0.1420	1.0007
∞	0.0000	∞	1.0000	0.0000	1.0000

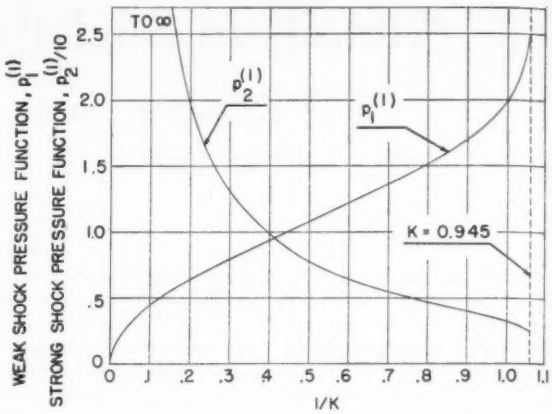

FIG. 1. Variation of compression shock pressure function with K. [Eqs. (19) and (20).]

$$(1/4) - [(8/27)(K^*)^3] = 0$$

or

$$K^* = (3/2)(1/4^{1/3}) = 0.945 \tag{17}$$

there are two distinct roots: $f = 1/2^{1/3}$ and $f = -2^{1/3}$. The second root is again without physical significance. Corresponding to the first root, the critical value $p^{(1)}$ is

$$p^{(1)}(K^*) = 2^{2/3} = 2.502 \tag{18}$$

K^* is actually then the lowest value for K, or the largest value for θ at a given M^0, for which the result has physical significance. This value of K must then correspond to the maximum flow deflection or critical condition for attachment at the leading edge. This checks with the calculation of von Kármán.[1]

For larger values of K, the physically meaningful values[3] of $p^{(1)}$ are

$$p_1^{(1)} = 1/\left[\sqrt{\frac{2}{3}}K\cos\left(\frac{\pi-\varphi}{3}\right)\right] \tag{19}$$

and

$$p_2^{(2)} = 1/\left[\sqrt{\frac{2}{3}}K\cos\left(\frac{\pi+\varphi}{3}\right)\right] \tag{20}$$

where φ is given by

$$\cos\varphi = (1/4)\sqrt{(27/2)(1/K^3)} \tag{21}$$

Since $K > K^*$, φ is greater than zero but smaller than $(\pi/2)$. Under these conditions, $p_2^{(1)} > p_1^{(1)}$. $p_1^{(1)}$ then corresponds to the weak shock case, and $p_2^{(1)}$ corresponds to the strong shock case. Following the general practice, $p_1^{(1)}$ will be used for attached leading-edge shocks.

The numerical values of $p_1^{(1)}$ and $p_2^{(1)}$ are tabulated in Table 1, and the data are plotted in Fig. 1. $p_1^{(1)}$ can be expressed as an inverse power series of K. Calculation shows that

$$p_1^{(1)} = \frac{1}{K^{1/2}}\left[1.41422 + \frac{0.25000}{K^{3/2}} + \frac{0.11048}{K^3} + \frac{0.06250}{K^{5/2}} + \frac{0.03987}{K^6} + \frac{0.02734}{K^{15/2}} + \frac{0.01966}{K^9} + \frac{0.01463}{K^{21/2}} + \frac{0.01119}{K^{12}} + \frac{0.00873}{K^{27/2}} + \cdots\right] \quad (22)$$

The first two terms of Eq. (22) agree with von Kármán's calculation. He did not consider the additional terms.

Let p^* denote the critical pressure corresponding to local sonic velocity. Then for isentropic flow,

$$\frac{p^*}{p^0} = \left[\frac{\frac{\gamma+1}{2} + \frac{\gamma-1}{2}(M^{0\,2} - 1)}{(\gamma+1)/2}\right]^{\gamma/\gamma-1}$$

The corresponding pressure coefficient, C_p^*, is then, according to Eq. (9),

$$C_p^* = \frac{2}{\gamma M^{0\,2}}\left\{\left[1 + \frac{\gamma-1}{\gamma+1}(M^{0\,2} - 1)\right]^{\gamma/\gamma-1} - 1\right\}$$

When $M^0 \approx 1$ for transonic flows, the above equation simplifies to

$$C_p^* = (M^{0\,2} - 1)/\Gamma \quad (23)$$

The flow after the strong shock is always subsonic. Sonic velocity after shock can only be associated with the weak shock. But it is known that the entropy change of a weak shock is negligible, and therefore Eq. (23) can be used for the weak shock case.

In general, as shown by Eq. (13),

$$C_p = [(M^{0\,2} - 1)/2\Gamma](p_1^{(1)}/K) \quad (24)$$

By comparing Eqs. (23) and (24), the critical value of $(p_1^{(1)})^*$ corresponding to local sonic velocity after the shock is

$$p_1^{(1)*}/K_s = 2 \quad (25)$$

where K_s is the value of K corresponding to $(p_1^{(1)})^*$. By dividing Eq. (14) by K^3,

$$\frac{1}{K^3} = \frac{1}{4}\left(\frac{p_1^{(1)}}{K}\right)^2\left[2 - \frac{1}{2}\left(\frac{p_1^{(1)}}{K}\right)\right] \quad (26)$$

and then substituting Eq. (25) into Eq. (26), the equation for K_s for sonic velocity after a shock is obtained:

$$K_s = 1 \quad (27)$$

Thus, for supersonic velocity after the leading edge shock, $K > 1$.

For airfoil calculations, one will also need the ratio $(M^2 - 1)/(M^{0\,2} - 1)$, where M is the Mach Number after the shock. This can easily be determined by noting that in general for isentropic flow

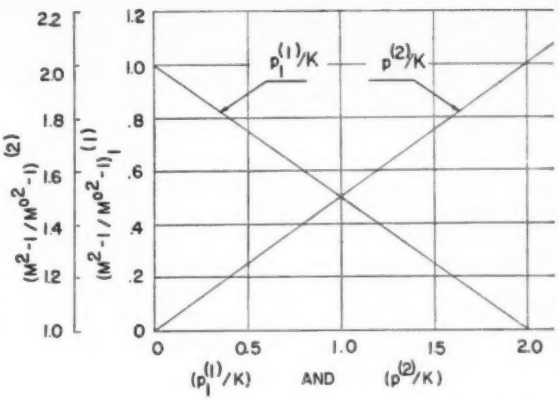

FIG. 2. Variation of $(M^2 - 1)/(M^{0\,2} - 1)$ with (p/K). [Eq. (29).]

$$\frac{p}{p^0} = \left\{\frac{1 + [(\gamma-1)/(\gamma+1)](M^{0\,2} - 1)}{1 + [(\gamma-1)/(\gamma+1)](M^2 - 1)}\right\}^{\gamma/\gamma-1}$$

where both $(M^2 - 1)$ and $(M^{0\,2} - 1)$ are small under transonic conditions. Then Eq. (9) gives

$$C_p = [(M^{0\,2} - 1)/\Gamma]\{1 - [(M^2 - 1)/(M^{0\,2} - 1)]\} \quad (28)$$

By combining Eqs. (24) and (28), the required ratio is given as

$$(M^2 - 1)/(M^{0\,2} - 1) = 1 - (1/2)(p/K) \quad (29)$$

This formula is, of course, generally true. If the value p is taken from Eq. (19), then the ratio will be that for the weak oblique shock. The numerical values are tabulated in Table 1, and the data are plotted in Fig. 2.

PRANDTL-MEYER EXPANSION

If q is the velocity and θ is the angle of turn during expansion, the Prandtl-Meyer expansion is determined by the relation[4]

$$dq = q\,d\theta/\sqrt{M^2 - 1}$$

However, in general,

$$dp = -\rho q\,dq$$

Thus, by eliminating dq from these two equations,

$$dp = -\rho q^2\,d\theta/\sqrt{M^2 - 1}$$

or

$$d\left(\frac{p}{p^0}\right) = -\left(\frac{\rho^0}{p^0}\right)\frac{(\rho/\rho^0)q^2\,d\theta}{\sqrt{M^2 - 1}} \quad (30)$$

Now since the expansion is adiabatic,

$$a^2 + \frac{\gamma-1}{2}q^2 = a^{0\,2} + \frac{\gamma-1}{2}U^2$$

Thus by using the isentropic relations, q^2 can be calcu-

lated from the above equation as

$$q^2 = \frac{2}{\gamma - 1} a^{0\,2}\left[1 + \frac{\gamma - 1}{2} M^{0\,2} - \left(\frac{p}{p^0}\right)^{\gamma-1/\gamma}\right]$$

Furthermore

$$M^2 - 1 = \left(\frac{2}{\gamma - 1} + M^{0\,2}\right)\left(\frac{p^0}{p}\right)^{\gamma-1/\gamma} - \frac{\gamma + 1}{\gamma - 1}$$

These relations, together with Eq. (9), then convert Eq. (30) into

$$\frac{dC_p}{d\theta} = -\frac{2}{M^{0\,2}} \frac{\left(1 + \frac{\gamma M^{0\,2}}{2} C_p\right)^{1/\gamma}\left[\frac{2}{\gamma - 1} + M^{0\,2} - \frac{2}{\gamma - 1}\left(1 + \frac{\gamma M^{0\,2}}{2} C_p\right)^{\gamma-1/\gamma}\right]}{\left[\left(\frac{2}{\gamma - 1} + M^{0\,2}\right)\left(1 + \frac{\gamma M^{0\,2}}{2} C_p\right)^{-(\gamma-1)/\gamma} - \frac{\gamma + 1}{\gamma - 1}\right]^{1/2}} \tag{31}$$

This is the exact equation. It can be simplified by noting that for transonic conditions C_p is small and M^0 is close to 1. Then, expanding the terms on the right-hand side of Eq. (31) into a power series of C_p, one finds that the significant terms are

$$\frac{dC_p}{d\theta} = -2/(M^{0\,2} - 1)^{1/2}\left(1 - \frac{\Gamma}{M^{0\,2} - 1} C_p\right)^{1/2} \tag{32}$$

Now, similar to Eq. (24), one can write

$$C_p = \frac{\theta^{2/3}}{\Gamma^{1/3}} p^{(2)}(K) = \frac{M^{0\,2} - 1}{2\Gamma}\left(\frac{p^{(2)}}{K}\right) \tag{33}$$

where $p^{(2)}$ is the pressure function associated with the Prandtl-Meyer expansion. Eq. (32) then becomes

$$\frac{1}{3} K^{-2/3} \frac{d}{dK}\left(\frac{p^{(2)}}{K}\right) = \frac{1}{\sqrt{2 - (p^{(2)}/K)}} \tag{34}$$

This can easily be integrated. The result is

$$[2 - (p^{(2)}/K)]^{3/2} = (3/K^{2/3}) + C \tag{35}$$

where C is the integration constant. To determine the constant, note that, when $\theta = 0$, no change is made in the free stream and $C_p = 0$. Then, when $K \to \infty$, $p^{(2)}/K \to 0$. Hence, the constant in Eq. (35) is equal to $(2)^{3/2}$. Then Eq. (35) can be solved for $p^{(2)}$, and the result is

$$p^{(2)} = \{2K - [(2K)^{2/3} + 3]^{3/2}\} \tag{36}$$

Therefore, when $M^\circ = 1$, and thus $K = 0$, the pressure coefficient is proportional to $\theta^{2/3}$, or

$$C_p = -[(3\theta)^{2/3}/\Gamma^{1/3}] \qquad (M^0 = 1) \tag{37}$$

This is in agreement with von Kármán's calculation.[1] For other values of K, the pressure function, $p^{(2)}$, and the ratio $(M^2 - 1)/(M^{0\,2} - 1)$ are tabulated in Table 1 and plotted in Figs. 2 and 3.

Flat Plate Airfoil

The aerodynamic coefficients of an airfoil can be obtained by integrating the pressure coefficients over the surface of the airfoil. If the local surface inclination to the free stream is θ, the sectional coefficients are

$$\left.\begin{aligned} C_l &= (1/c)\int_c (C_{p_{\text{lower}}} - C_{p_{\text{upper}}})dx \\ C_d &= (1/c)\int_c (C_{p_{\text{lower}}} - C_{p_{\text{upper}}})(\sin\theta)dx \\ -C_{m_{c/4}} &= (1/c)\int_c (C_{p_{\text{lower}}} - C_{p_{\text{upper}}})[\text{C. P.} - (c/4)]dx \end{aligned}\right\} \tag{38}$$

where c is the airfoil chord and C. P. is the center of pressure.

Consider now a flat plate inclined at an angle, α, to the flow such that an oblique shock and a Prandtl-Meyer expansion take place at the leading edge of the lower and upper surfaces, respectively. By integrating Eqs. (38), noting that sin α may be approximated by α, and utilizing Eqs. (13) and (33), one has

$$\left.\begin{aligned} C_l &= (\alpha^{2/3}/\Gamma^{1/3})L(K) \\ C_d &= (\alpha^{5/3}/\Gamma^{1/3})L(K) \\ -C_{m_{c/4}} &= (1/4)C_l \end{aligned}\right\} \tag{39}$$

where $L(K) = [p_1^{(1)} - p^{(2)}]$ and $K = (M^{0\,2} - 1)/2(\alpha\Gamma)^{2/3}$.

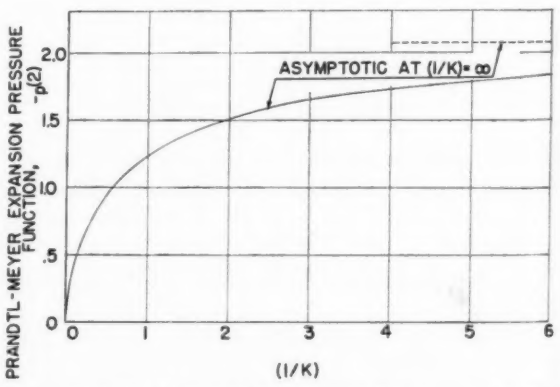

FIG. 3. Variation of Prandtl-Meyer expansion pressure function with K. [Eq. (36).]

Rearranging Eqs. (39), the aerodynamic coefficients may be plotted in a simple manner involving only the lift function $L(K)$. Thus,

$$L(K) = \frac{\Gamma^{1/3}}{\alpha^{2/3}} C_l = \frac{\Gamma^{1/3}}{\alpha^{2/3}} C_d = -4 \frac{\Gamma^{1/3}}{\alpha^{2/3}} C_{m_{c/4}} \quad (40)$$

This has been carried out in Fig. 4. Curves of C_l versus M^0 and C_l versus α have been calculated from these data and are presented in Figs. 5 and 6. Drag and moment coefficient curves can be seen to be similar to the lift coefficient curve with only a change in the scale of the ordinate. Data obtained by the use of Ackeret's linearized theory have been included with the curves for comparison. Two features are immediately apparent from the figures: First, the lift versus angle of attack curve is not a straight line as predicted by the linear theory but has a definite upward curvature; secondly, the predicted lift is at all times greater than Ackeret's prediction, and this difference increases with increasing angle of attack.

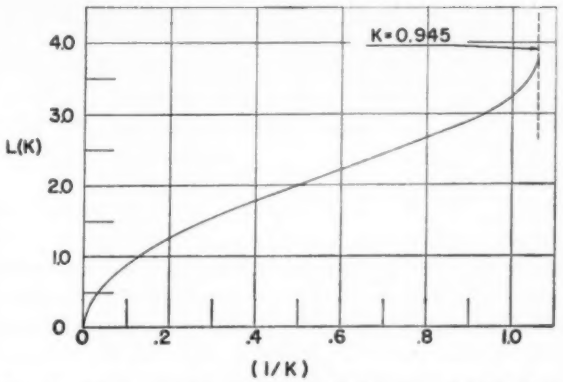

FIG. 4. Lift, drag, and moment similarity curve for flat plate airfoil [Eqs. (40).]

ASYMMETRIC WEDGE AIRFOIL

As an example of finite thickness airfoils, consider now the asymmetric wedge depicted in Fig. 7. Denoting the vertex angle at the leading edge by θ, Table 2 lists the C_p and K for each region of the airfoil. It should be noted that the C_p for region (2) given in Table 2 is relative to region (1). Account may be taken of this by noting that

$$(C_p)_{2_{\text{relative to free stream}}} = \frac{p_2 - p^0}{q} = \frac{p_2 - p_1}{q} + \frac{p_1 - p^0}{q}$$

$$= (C_p)_{2_{\text{relative to region (1)}}} + (C_p)_1 \quad (41)$$

to the order of magnitude of these calculations.

Since all angles are small, the coefficients may be written in integrated form as

$$\left.\begin{aligned} C_l &= (C_p)_3 - (1/2)(C_p)_1 - (1/2)(C_p)_2 \\ C_d &= \alpha(C_p)_3 + (1/2)(\theta - \alpha)(C_p)_1 - \\ &\quad (1/2)(\theta + \alpha)(C_p)_2 \\ -C_{m_{c/4}} &= (1/4)[(C_p)_3 - (C_p)_2] \end{aligned}\right\} \quad (42)$$

In order to transform Eqs. (42) into a form similar to Eq. (40) for the flat plate, two parameters, K_w and m are now defined such that

$$K_w = (1/2)[(M^{0\,2} - 1)/(\theta\Gamma)^{2/3}] \quad (43)$$

and

$$m = (\alpha/\theta) \quad (44)$$

The expressions for K and C_p in terms of these parameters are tabulated in Table 3. Taking into account Eq. (41), Eqs. (42) can now be written

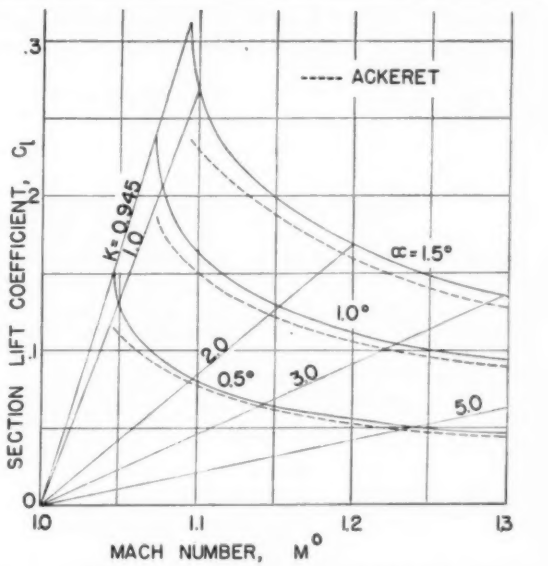

FIG. 5. Variation of section lift coefficient with Mach Number for the flat plate airfoil.

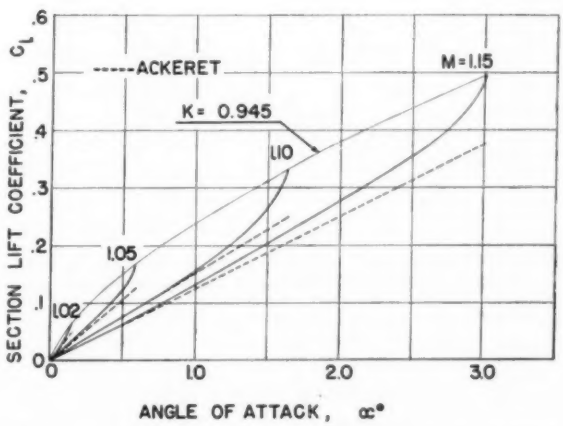

FIG. 6. Variation of section lift coefficient with angle of attack for the flat plate airfoil.

$$\left.\begin{aligned} C_l(\Gamma^{1/3}/\theta^{2/3}) &= m^{2/3}p_1^{(1)}(K_3) - (1-m)^{2/3}p_1^{(1)}(K_1) - (2)^{-1/3}p^{(2)}(K_2) \\ &= L(K, m) \\ C_d(\Gamma^{1/3}/\theta^{2/3}) &= m^{5/3}p_1^{(1)}(K_3) + (1-m)^{5/3}p_1^{(1)}(K_1) - (2)^{-1/3}(1+m)p^{(2)}(K_2) \\ &= D(K, m) \\ -C_{m_{c/4}}(\Gamma^{1/3}/\theta^{2/3}) &= (1/4)[m^{2/3}p_1^{(1)}(K_3) - (2)^{2/3}p^{(2)}(K_2)] \\ &= M(K, m) \end{aligned}\right\} \quad (45)$$

where the right-hand sides of Eqs. (45) are functions only of K_w and m. These are the similarity relations for the asymmetric wedge airfoil. Calculations have been carried out and plotted in Figs. 8a, 8b, and 8c, for a range of values of $0 \leq m \leq 1$ and $0.632 \leq K_w \leq 1.90$. The chosen upper value of K_w was approximated by using a free stream with M^0 equal to 1.30 as a maximum and a wedge with $\theta = 3°$ as a minimum. The chosen lower value of K_w was determined by allowing a small range of values for m in which the present theory is applicable. The theoretical value of $K_w \to \infty$—i.e., either a flat plate or a wedge in a stream of infinite M^0—is seen to lie along the horizontal axis. Note, in Figs. 8a, 8b, and 8c, the limiting line for an attached shock ($K_3 = 0.945$) at the leading edge when approximately $0.55 \leq m \leq 1.0$, and note also the limiting line for sonic flow ($K_1 = 1.0$) in region (1) of the airfoil when approximately $0 \leq m \leq 0.55$. The latter is a necessary condition for applying the Prandtl-Meyer flow in region (2).

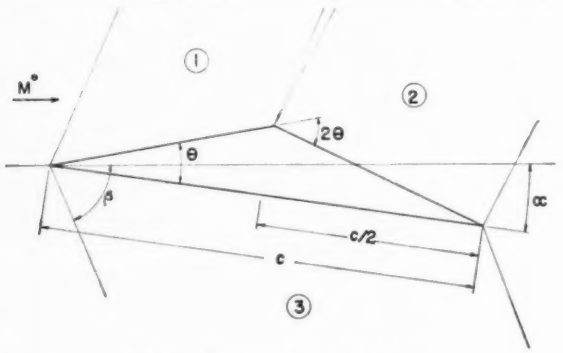

FIG. 7. Asymmetric wedge airfoil.

TABLE 2
Pressure Coefficient and K for Regions of Asymmetric Wedge Airfoil

Region i	C_p	K_1
1	$\frac{(\theta-\alpha)^{2/3}}{\Gamma^{1/3}}\,p_1^{(1)}$	$\left(\frac{1}{2}\right)\frac{M_0^2-1}{[(\theta-\alpha)\Gamma]^{2/3}}$
2	$\frac{(2\theta)^{2/3}}{\Gamma^{1/3}}\,p^{(2)}$	$\left(\frac{1}{2}\right)\frac{M^{0\,2}-1}{(2\theta\Gamma)^{2/3}}$
3	$\frac{\alpha^{2/3}}{\Gamma^{1/3}}\,p_1^{(1)}$	$\left(\frac{1}{2}\right)\frac{M^{0\,2}-1}{(\alpha\Gamma)^{2/3}}$

TABLE 3
Pressure Coefficient and K for Regions of Asymmetric Wedge Airfoil in Terms of the Similarity Parameters K_w and m

Region i	C_p/R	K_1
1	$(1-m)^{2/3}$	$K_w/(1-m)^{2/3}$
2	$(2)^{2/3}$	$\frac{K_w}{(2)^{2/3}}\left[\frac{M_1^2-1}{M^{0\,2}-1}\right]$
3	$(m)^{2/3}$	$K_w/m^{2/3}$

$R = (\theta^{2/3}/\Gamma^{1/3})p(K_1)$.

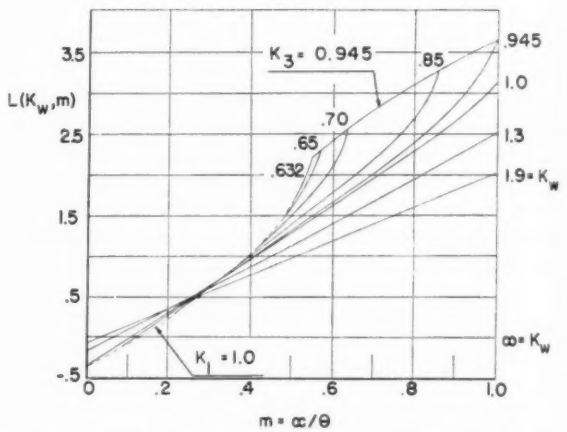

FIG. 8a. Lift similarity curves for asymmetric wedge airfoil. [Eq. (45).]

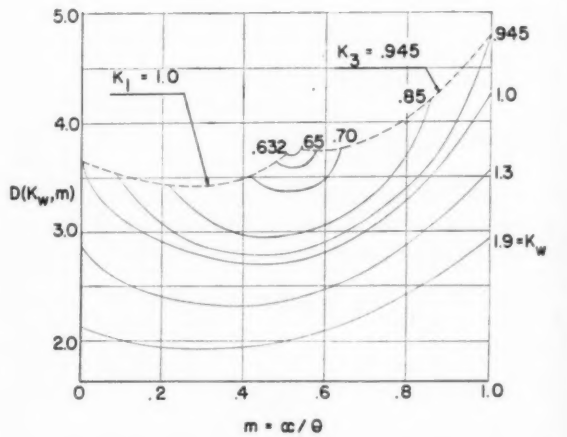

FIG. 8b. Drag similarity curves for asymmetric wedge airfoil. [Eq. (45).]

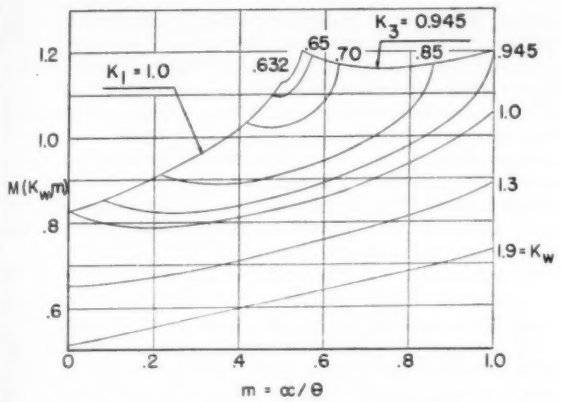

FIG. 8c. Moment similarity curves for asymmetric wedge airfoil. [Eq. (45).]

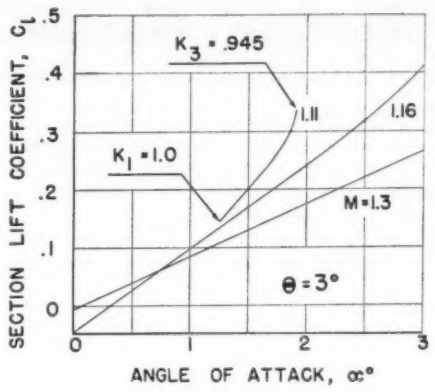

FIG. 10. Variation of section lift coefficient with angle of attack for the asymmetric wedge airfoil. (θ = 3°.)

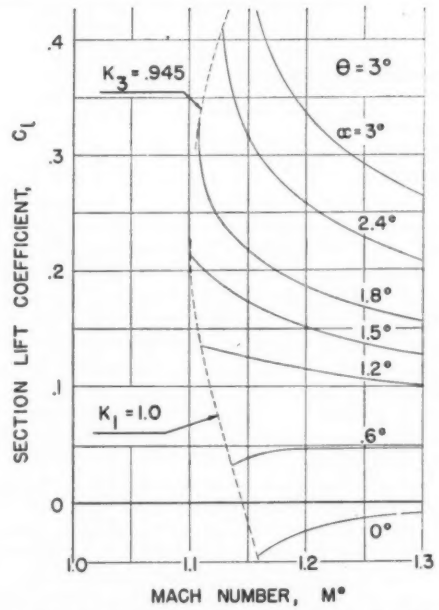

FIG. 9. Variation of section lift coefficient with Mach Number for the asymmetric wedge airfoil. (θ = 3°.)

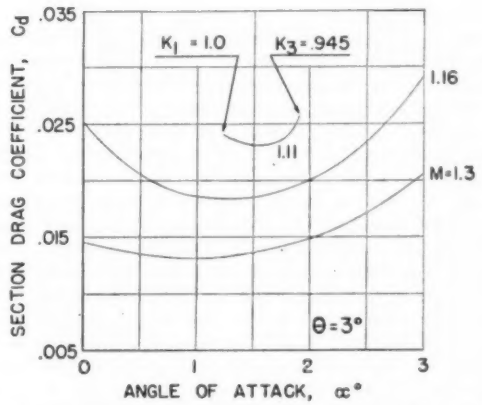

FIG. 11. Variation of section drag coefficient with angle of attack for the asymmetric wedge airfoil. (θ = 3°.)

As is to be expected, for the asymmetric wedge, zero lift occurs at a small angle of attack. It should be noticed that, as K_w increases (Fig. 8a), the lift versus angle of attack curves become linear. This can be explained by considering the two variables that determine K_w: M^0 and θ. If θ is considered constant, then K_w increases as M^0 increases, and thus, for Mach Numbers much greater than 1.0, the lift curve is linear, as is well known. Considering, on the other hand, M^0 constant, then K_w increases as the wedge becomes thinner, and the ratio m represents a smaller variation of angle of attack. In the limit, when $K_w \to \infty$, the representation is that of a flat plate at zero angle of attack for all values of m.

(*Continued on page 64*)

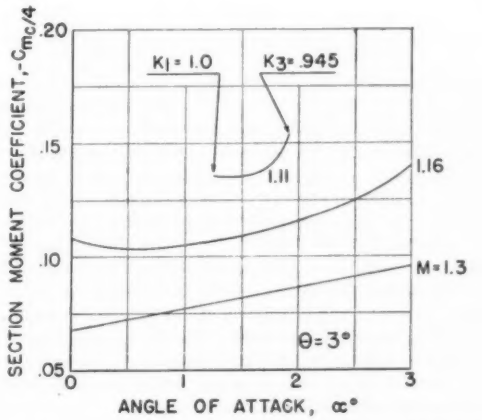

FIG. 12. Variation of section moment coefficient (about quarter-chord) with angle of attack for the asymmetric wedge airfoil. (θ = 3°.)

Readers' Forum

BRIEF REPORTS of important findings in aeronautical sciences and discussions of papers published in the JOURNAL *will be presented in this special department. Publication will be completed 6 to 8 weeks after receipt of the material. No proof will be sent to the authors. The Editorial Committee does not hold itself responsible for the opinions expressed by the correspondents. Contributions should not exceed 800 words in length.*

Determination of Stability Derivatives from Flight Data

Harry Greenberg
Ames Aeronautical Laboratory, N.A.C.A., Moffett Field, Calif.
October 13, 1948

IN AN INFORMATIVE ARTICLE in the JOURNAL OF THE AERONAUTICAL SCIENCES (September, 1947) entitled "Progress in Dynamic Stability and Control Research," by W. F. Milliken, Jr., of Cornell Aeronautical Laboratory, it was shown how certain dynamic stability parameters of an airplane can be determined from oscillation tests made in flight. These consist of combinations of the fundamental stability derivatives such as M_α, M_q, $M_{\dot\alpha}$, etc. In the above-mentioned paper, Milliken and his coworkers were able to determine the lift curve slope from the flight data but were unable to break down the stability parameters b and k into their component parts, the stability derivatives. The purpose of this letter is to show that there is a fundamental reason why it is impossible in some cases to determine the moment derivatives solely from flight data, no matter how accurately or carefully the tests are made. It is possible in these cases to determine only certain linear combinations of the derivatives; these are sufficient to determine the dynamic characteristics of the airplane.

Consider first the case of longitudinal motion with forward speed assumed constant, an assumption that is legitimate at the start of a maneuver or for high-frequency oscillation tests. This is the case analyzed in some detail in the paper referred to above. In this case the equations of motion are:

$$\alpha L_\alpha = mV(q - \dot\alpha) \tag{1}$$

$$\alpha M_\alpha + \dot\alpha M_{\dot\alpha} + qM_q + \delta M_\delta = I_y\dot q \tag{2}$$

By making simultaneous measurements of α and q (or of n and q, where n is the normal acceleration), it is certainly possible to determine L_α/mV from Eq. (1). It might be thought that, by taking a sufficient number of measurements of α and q, the values of M_α/I_y, $M_{\dot\alpha}/I_y$, M_q/I_y, and M_δ/I_y could be determined from Eq. (2) by solving four simultaneous equations for the four unknowns. But these equations will not be linearly independent, since a linear relation exists between the coefficients of these simultaneous equations. This linear relation is contained in Eq. (1), which states that the quantities α, q, and $\dot\alpha$ are linearly dependent. Hence, only M_δ/I_y can be determined from Eq. (2). As for the other three unknowns (M_α/I_y, $M_{\dot\alpha}/I_y$, and M_q/I_y), only two linearly independent combinations of them can be determined. The parameters b and k mentioned in Milliken's report are two such combinations.

If the equations are generalized to include the derivatives L_δ and L_q, it is still possible to determine the lift derivatives, but again it is not possible to determine the moment derivatives solely from flight measurements involving two degrees of freedom for the same reason given above.

If the flight measurements are made in such a way as to allow the forward speed to vary (low-frequency oscillation tests or long duration maneuvers) and include at least two c.g. positions, then it is possible to determine the neutral point of the airplane. If the derivative M_u is zero, then it is possible to determine M_α and all other moment derivatives. But if the derivative M_u exists, it is again impossible to determine M_α and M_u individually but only a linear combination of them. This can be shown in the same manner as above for two degrees of freedom.

In the case of lateral stability, the situation with regard to the determination of the derivatives from flight measurements is more favorable. This is because of the assumed absence of a yawing moment derivative with respect to rate of change of sideslip, analogous to the pitching moment derivative with respect to rate of change of angle of attack. Hence, each equation is solvable for its derivatives by the method of simultaneous equations, since these equations are linearly independent.

On Sweat-Cooling

E. A. Richardson
Bethlehem Steel Company, Bethlehem, Pa.
July 31, 1948

I HAVE GIVEN some study to Preprint No. 137, entitled "Experimental Study of Cooling by Injection of a Fluid Through a Porous Material," by Pol Duwez and H. L. Wheeler, Jr., presented at the Third National Flight Propulsion Meeting, March 19, 1948 (published in the JOURNAL OF THE AERONAUTICAL SCIENCES, Vol. 15, No. 9, p. 509, September, 1948). This letter will cover not only this paper, but also certain references as "Stability of the Laminar Boundary Layer with Injection of a Cool Gas at the Wall," by Lester Lees, Aeronautical Engineering Laboratory, Princeton University, May 20, 1948, and a recent paper by S. W. Yuan, of the Polytechnic Institute of Brooklyn, on the temperature field in the boundary layer. In none of the last three papers did the authors appreciate that heat flow in a fluid moving with a velocity component parallel to, and opposite to, the direction of the flow of such heat is vastly different from that in a stationary fluid. In my opinion all such papers are quite unrepresentative of the matter in question, however well conceived otherwise. Reference should be made to the paper "Mathematical Attacks on Forced Convection Problems," by T. B. Drew, Transactions of the American Institute of Chemical Engineers, Vol. xxvi, 1931, in which the differential equations for constant mass velocity of flow are given and the case of the constant and uniform line source of heat normal to the flow direction is derived. A little further study through the derivation of a uniform and constant plane source of heat normal to the direction of constant mass velocity fluid flow would show that the steady-state temperature distribution upstream from such a plane source is a long function falling off with extreme rapidity. This tends to be true when $(c_{p\rho}vx/2k)$ for the fluid is of the order of, or greater than, about 2, where $c_{p\rho}$ is the specific heat per cubic foot at constant pressure, v is the fluid velocity in feet per hour, x is the distance from the plane heat source in feet, and k is the conductivity in B per square foot per hour per 1°F. per foot. Hence, with small flow velocities, virtually no heat can travel as far as (or the order of) 0.001 ft. upstream. Hence, at attainable flow velocities, only radiant heat can pass through a relatively thin fluid layer. It should be obvious that a thicker layer, or a faster velocity, when the boundary layer varies in velocity normal to the source, will yield the same sort of result.

Table 3 of Duwez and Wheeler seems incorrect in the quoted velocity of fluid flow V of the hot gases. I plotted the heat flow q in B per sq.in. per sec. versus V in ft. per sec. and secured substantially straight lines for any assigned pair of values of hot gas temperature T_L and surface of porous body temperature T_1. For Tables 2, 4, and 5 these straight lines fairly consistently passed through the origin, but for Table 3 the common point approximated $q = 0$ at $V = -200$ ft. per sec. I then plotted the fluid exit velocity v to the gas stream velocity V and again obtained substantially straight lines. As before, Tables 2, 4, and 5 gave lines through the origin, while Table 3 gave lines through a point at $v = 0$, $V = -200$ ft. per sec. This matter should be cleared up.

Limiting myself to Tables 2, 4, and 5, I proceeded to derive coefficients C' in the formulas $Q = C'V$, plotting them versus $(T_L - T_1)$, which last is the difference between the average temperature T_L of the turbulent hot gas core and that, T_1, of the hot surface of the porous wall. Three such plots resulted, one for each table. It did not appear that they could be reduced to one plot through use of Reynolds Number R_θ. In each case, the plot was effectively a straight line through the origin up to a characteristic value marking the beginning of a curve convex upwards which tended to exhibit a maximum. Lack of range in the data resulted in but one curve extending far enough to show a maximum followed by a rapid falling away therefrom, this curve being for $T_L = 1{,}900°$F., which showed a maximum at approximately $(T_L - T_1) = 1{,}400°$F.

In similar fashion, I then plotted coefficients C'' in formulas of the type $v = C''V$ against $(T_L - T_1)$ for each value of T_L. The resulting plots in each case comprised two intersecting straight-line sects. The point of intersection of these sects corresponds approximately to the point of departure of C' from the straight line in the preceeding set of plots.

It will be seen, I think, that any attempt to study the ratio of $(T - T_1)/(T_1 - T_0)$ (where T is the hot gas temperature and T_0 that of the entering fluid) against Q/W, the ratio of permeating fluid flow per square inch per second to that of the hot gases, as in Fig. 10 where a narrow and straight band of points passing through the origin is found from 0 to 0.014, can be misleading. Similarly, the plotting, following Rannie, of $(T - T_1)/(T - T_0)$ which should yield curves asymptotic to 1.0, as Q/W increases, is misleading, since even the plot of experimental points in Fig. 11 show a definite trend to a straight line (or lines) above $Q/W = 0.011$, which would reach 1.0 by, or before, $Q/W = 0.030$. This is extremely important if true. The plotting of $(T - T_1)/(T_1 - T_0)$ versus v/U, as in Fig. 12, is not so misleading, since the departures from the mean (or extrapolated) curve are noteworthy above $v/U = 0.0047$. It is of interest that similar points tend to lie on straight lines above this point. (U differs from V in that the former is the flow average velocity for the stream while the latter is the maximum velocity measured at the core center.) This curve may well be extremely misleading, however, since the form of plotting used by the present writer indicates the easy attainment of much higher ratios of $(T - T_1)/(T_1 - T_0)$ with moderate increases of v/U and would look like the stress curve in column buckling. (See Timoshenko, *Theory of Elastic Stability*, 1st Ed., p. 39, Fig. 18; McGraw Hill Book Company, Inc., New York, 1936).

With reference to Table 1, in which nitrogen and hydrogen cooling are compared, the ratio of the flow of the two fluids for equivalent results is that demanded by the theory of heat diffusion in that the fluid exit velocity ratio must be that of $\sqrt{k_2 c_1/k_1 c_2}$ where k is the conductivity, c is the heat capacity of the fluid, and subscript 2 might refer to hydrogen and 1 to nitrogen. As c_1 is substantially equal to c_2, for these fluids, the ratio is that of the conductivities. The calculated ratio is closely the measured ratio. My original calculation was too low because of the use of old data; more modern data give a better check.

My own experience in the art of cooling high-temperature furnaces indicates that it is not necessary to use a separate fluid for a coolant. The desired wall protection may be secured by passing the whole air mass for combustion through the furnace walls, if desired, since it must be obvious, from the same art, that vortex-type combustion furnaces with the highest rates of heat generation may be used because this same boundary layer keeps the burning gases from licking the wall.

Although heat flow by radiation from the gases was small in the experimental apparatus (of the order of $0.001B$ per sq.in. per sec.), the same will not necessarily be true in a larger apparatus, particularly when combustion is occurring therein.

Induction Effects in Aeroelasticity

John W. Miles
Department of Engineering, University of California at Los Angeles
September 7, 1948

HILDEBRAND AND REISSNER have investigated the effects of induction on the torsional divergence speed of an unswept wing and concluded that strip theory, using the two-dimensional lift curve slope, led to errors of from 15–40 per cent.[1] The writer recently had occasion to investigate this problem for Northrop Aircraft, Inc.,[2] and found that the error introduced by strip theory for elliptic or tapered wings of continuous stiffness distribution is made small simply by introducing the mean lift curve slope for the rigid wing (i.e., corrected for induction effects) rather than the two-dimensional slope.

Analysis of the integrodifferential equation governing the torsional deformation of the aerodynamically loaded wing leads to the introduction of the modulus $\tilde{\omega}$ as the ratio of the indicated air speed to the divergence speed (i.e., $\tilde{\omega} = 1$ at divergence), and it is found that

$$\tilde{\omega}^2 = (qb^2/4)\left[\int_0^1 e(s)c^2(s)\theta(s)c_l^{\theta}(s)ds\right] \times \left\{\int_0^1 GJ(s)\left[\frac{\partial\theta(s)}{\partial s}\right]^2 ds\right\} \quad (1)$$

where q is the dynamic pressure, b is the span, e is the fraction of the chord of the elastic axis aft of the line of aerodynamic centers (eccentricity), c is the chord, θ is the elastic twist, c_l^{θ} is the lift coefficient distribution due to θ, GJ is the torsional stiffness distribution, and s is a dimensionless coordinate running from 0 at the root to 1 at the tip. Moreover, the equation is self-adjoint, $\tilde{\omega}$ being the eigenvalue, and it therefore follows (the Rayleigh principle) that $\tilde{\omega}$ is an absolute minimum with respect to first order variations of $\theta(s)$ about the true solution to the integrodifferential equation.

Using the Prandtl lifting line theory to determine c_l^{θ} from θ, using variational (or Rayleigh) theory to solve Eq. (1), and assuming that $GJ(s)$ was proportional to the fourth power of the chord, the writer found[2] that $\tilde{\omega}$ was given by

$$\tilde{\omega} = (3/8)\left[(dc_L/d\alpha)eS^3q/GJ(0)\right]^{1/2} \quad (2)$$

with a maximum error of 3 per cent for taper ratios between 1.6:1 and α. $(dc_L/d\alpha)$ is the lift curve slope for the rigid wing, and e is assumed constant. For asymmetrical loading $(dc_L/d\alpha)$ should be evaluated for half the true aspect ratio. Thus, it is well to introduce $\tilde{\omega}_s$ and $\tilde{\omega}_a$ for symmetrical and asymmetrical loading.

[1] Hildebrand, F. B., and Reissner, Eric, *The Influence of the Aerodynami Span Effect on the Torsional Divergence Velocity and on the Shape of the Corresponding Deflection Mode*, N.A.C.A. T.N. No. 926, 1944.

[2] Miles, John W., *Aeroelastic Properties of Unswept Wings, Lifting Line Theory*, Northrop Report A-101, 1947.

The modulus $\tilde{\omega}$ is the dominant parameter in all aeroelastic calculations not involving control surface loading. Thus, it is found[2] that the lift coefficient (given root angle of attack) and damping in roll coefficients for a wing of two to one taper and aspect ratio 6 (and, within a few per cent, for all unswept wings) are given by

$$(c_L/c_L^0) = 1 + 0.87[\tilde{\omega}_s^2/(1 - \tilde{\omega}_s^2)] \quad (3)$$

$$(c_{l_p}/c_{l_p}^0) = 1 + 0.98[\tilde{\omega}_a^2/(1 - \tilde{\omega}_a^2)] \quad (4)$$

where the superscript 0 denotes the value of the coefficient for the rigid wing.

In the case of control surface loading the reversal speed is more significant than the divergence speed, and it is therefore expedient to introduce the parameter $\tilde{\omega}_R$ as the ratio of the indicated air speed to the reversal speed ($\tilde{\omega}_R = 1$ at reversal). In this case it is found that the results are relatively insensitive to induction effects if the *two-dimensional lift curve slope* is used. The ratio $(\tilde{\omega}_R/\tilde{\omega})$, as given by Eqs. (1) or (2) [with $(dc_L/d\alpha)$ evaluated as the two dimensional lift curve slope], is plotted against the parameter, Γ_δ in the accompanying Fig. 1 for a 30 per cent span aileron on a two to one tapered wing of aspect ratio 6, where

$$\Gamma_\delta = 1 + (c_{m_\delta}/ec_{l_\delta}) \quad (5)$$

c_{m_δ} and c_{l_δ} being the section characteristics of the control surface.

These results are not too sensitive to variations of parameters other than Γ_δ. Using N.A.C.A. test data,[3] Γ_δ is plotted versus the control surface chord ratio for various products of the two dimensional lift curve slope (m) and the eccentricity (e) in Fig. 2.

If $\tilde{\omega}_R$ is evaluated according to the last paragraph, it is found that

$$(p/p^0) = 1 - \tilde{\omega}_R^2 \quad (6)$$

to within a few per cent for all practical configurations. This parabolic fall-off of rolling effectiveness with indicated air speed seems to be a rather well-known empirical conclusion.

More detailed results, including the calculation of dynamic stability derivatives, are given in reference 2. It should be specifically remarked that the results are not applicable to swept wings, where bending will generally be more important than torsion.

[3] Ames, M. B., and Sears, R. I., *Determination of Control Surface Characteristics from N.A.C.A. Plain Flap and Tab Data*, N.A.C.A. T. R. No. 721, 1941.

Airfoils in Slightly Supersonic Flow

(*Continued from page 61*)

To illustrate the nature of the coefficients in the usual form, calculations have been carried out for the case of $\theta = 3°$ and are plotted in Figs. 9 through 12.

Fig. 9 shows that, at small angles of attack giving positive lift, the lift coefficient actually increases with increase in Mach Number. This is a behavior not predicted by Ackeret's linear theory, which requires a decrease in lift coefficient with Mach Number according to the factor $1/(M^{02} - 1)^{1/2}$.

REFERENCES

[1] von Kármán, Th., *The Similarity Law of Transonic Flow*, Journal of Math. and Physics, Vol. 26, No. 3, pp. 182–190, October, 1947.

[2] Liepmann, H. W., and Puckett, A. E., *Introduction to Aerodynamics of a Compressible Fluid*, pp. 51–58; John Wiley & Sons, New York, 1947.

[3] Burington, R. S., *Handbook of Mathematical Tables and Formulas*, 2nd Ed., pp. 7–9; Handbook Publishers, Sandusky Ohio, 1947.

[4] Ibid., reference 2, p. 212.